PROGRESS TOWARDS REALIZING ATOM-LIGHT INTERFACE WITH BLUE-DETUNED TWEEZERS ARRAY

by

NG BOON LONG

(B.Sc.(Hons), National University of Singapore)

A THESIS SUBMITTED FOR THE DEGREE OF

DOCTOR OF PHILOSOPHY

in

CENTRE FOR QUANTUM TECHNOLOGIES

NATIONAL UNIVERSITY OF SINGAPORE

2023

Supervisor:
Professor Christian Kurtsiefer

Examiners:
Assistant Professor Yvonne Y. GAO, National University of Singapore
President's Assistant Professor LOH Huanqian, National University of Singapore

Declaration

I hereby declare that this thesis is my original work and it has been written by me in its entirety. I have duly acknowledged all the sources of information which have been used in the thesis.

This thesis has also not been submitted for any degree in any university previously.

Ng Boon Long

01 August 2023

Acknowledgments

Back in 2016, I had a conversation with a professor in a coffee shop that lead me to this research path. At the end of the conversation, he casually asked which field of physics I am more interested in and I naively answered "Quantum.". He then told me that I should try to approach Prof Christian for some research opportunity, and I did. I still remember the day when he showed me the lab and told me that we will figure something out for the project that I will be working on. From that time onward, Christian remains as my supervisor until now, throughout my last two years of undergrad study and my whole PhD life. I would like to express my deepest gratitude and appreciation for Christian's mentorship along my journey in this research group.

Next, I would like to extend my gratitude to my lab partner, Chang Hoong for his guidance and support throughout the entire course of my PhD. This project would not have been possible without his constructive input and continuous flow of ideas. The wide range of knowledge and skill set that he had made me feel safe to explore something completely new for me because I know he will be there to back me up. Most importantly, countless night of coffee, discussion, and encouragement from him is what prevents this adventure from stopping halfway.

Thanks to my mentor, Mathias Seidler for equipping me with various kinds of skills that last for my entire research journey including programming, electronics, atomic physics, and the most crucial one being how to couple a laser into an optical fiber. Without these solid foundations, I can imagine that my growth as a researcher will be much slower.

Special thanks to Wilson and Matthias Steiner, the predecessor of this experiment for setting up the main part of the single atom setup. I can tell the effort in constructing the setup as it has been trapping single atoms for almost eight years and it is still working fine.

The friendly environment and accompanies that I get are what support me through the ups and downs in the past 7 years. I am thankful for the presence of these people - Adrian, Janet, Chi Huan, Lijiong, Florentin, and Wen Xin. I will always remember all the food and beer that we had together.

I would like to extend my gratitude to all the other members of the Quantum

Optics group, including Hou Shun, Peng Kian, Yicheng, Jianwei, Xi Jie, Justin, Alessandro, Brenda, Jaesuk, and Darren. Some of the undergraduate students that I would like to mention are Neville, Ting You, Mervin, Kelly, Wai Marn, Ilija, Philip, Eva, and Zifang. Thank you for the short but wonderful memory together in the office and in the lab.

Lastly, I want to thank my family and friends for their unwavering support and encouragement throughout this journey.

Contents

Abstract

Progress Towards Realizing Atom-Light Interface with Blue-Detuned Tweezers Array

by

Ng Boon Long

Doctor of Philosophy in Centre For Quantum Technologies

National University of Singapore

In this work, we focus on exploring the potential of realizing a light-atom quantum interface using a closed optical transition that involves a magnetic-sensitive ground state. Through coherent state manipulation within the ground state manifold, we have the capability to couple our qubits selectively to the specific optical channels. This has opened up the possibility to implement some protocols in an optically-trapped ^{87}Rb atom that are initially developed for solid-state qubits such as schemes for the generation of time-bin atom-photon entanglement [1] and the sequential generation of an entangled photonic string [2, 3].

First, we experimentally study the performance of dynamical decoupling on preserving the coherence of the ground state qubit. We use the two magnetic-sensitive $5^2S_{1/2}$ Zeeman levels as qubit states, motivated by the possibility to couple one of the states to the $5^2P_{3/2}$ excited state via a closed optical transition. We manage to extend the coherence time to close to 2 ms with periodic dynamical decoupling sequence, and further improvement is limited by pulse imperfection. We apply the Carr-Purcell-Meiboom-Gill sequence to our qubit system, which has been demonstrated to be able to mitigate pulse imperfections. With up to $N = 50$ π-pulses, we manage to achieve a coherence time of 6.8 ms as compared to T_2^* of 38(3) μs obtained from Ramsey experiment.

Next, we report on the observation and analysis of the resonance fluorescence emitted from the closed optical transition mentioned above. For driving strength above the saturation regime, we observe a triplet structure in the emission spectrum which is the well-known Mollow triplet. Under off-resonant excitation, the temporal cross-correlation between photons originating from different sidebands indicates that

there is a preferred time-ordering of the emitted photons. The cascaded generation of time-correlated fluorescence photons with a tunable frequency difference will be useful for quantum optics experiments and quantum communication protocols.

In the last part, we explore the possibility of implementing a reconfigurable blue-detuned optical dipole trap using a spatial light modulator. We manage to characterize the intensity profile of the bottle beam trap in a test setup. By manipulating spatial phase profile of the trap laser, we demonstrate the scaling up to multiple dipole traps in such a configuration. We have successfully incorporated this bottle beam trap into our current setup to confine a single atom. To characterize the performance of this trap, several measurements have been done including the lifetime and coherence of the single atom in the blue-detuned trap. This work is still in progress and more effort is needed to improve the reliability of the trap.

List of Figures

Chapter 1

Introduction

Over the past 30 years, the rapid development in quantum information science has been driven by many discoveries and a deeper understanding of the underlying principle. A fascinating application of quantum information science is quantum computation, where it harnesses the principles of quantum mechanics and leverages the counterintuitive properties of quantum systems to solve complex computational problems that are intractable for classical computers [4].

Quantum bits, or qubits, are the fundamental unit of information in quantum computing. Unlike classical bits, which can only exist in logical states of 0 or 1, qubits can be in coherent superpositions of both states. Entanglement is another unique feature of a quantum system where a quantum correlation with no classical analogue exists between several entangled qubits. The state of these entangled qubits can only be described as an inseparable whole. Utilizing these properties, people manage to realize schemes and algorithms that could speed up the computational process for some very complex problems. For example, Shor's algorithm [5] is proposed to lower the computational complexity of factorization of large numbers, which could result in vulnerability in the widely-used RSA encryption scheme. The real-life applications of quantum computation are not that far-fetched nowadays as several proof-of-principle experiments have been demonstrated [6–10].

Researchers are actively exploring viable candidates for quantum computing, such as neutral atoms [11, 12], cavity QED [13, 14], superconducting circuits [15, 16], trapped ions [17–19], semiconductor quantum dots [20–22], etc. Each platform presents unique advantages and challenges, but none has emerged as the definitive solution. There are two important considerations in realizing a practical quantum

computer: local computational power and connectivity between different quantum systems. To achieve efficient quantum information processing locally, the quantum system must allow qubit state preparation, manipulation, and readout with high fidelity. While the long coherence time of the qubit relative to the gate operation time is necessary to avoid information loss along the computation process, the scalability of the quantum system is also of paramount importance since the number of functional qubits is essential for quantum computers to outperform their classical counterparts [23].

When a quantum system fulfills the above criteria, one needs to start thinking about its connectivity with other quantum systems in order to transmit quantum information over long distances. Optical photons are an excellent choice for this purpose as the quantum information encoded in the photonic states can be preserved for a long time due to the low interaction probability with the environment [24]. As such, the quantum system in consideration needs to have some sort of capability to convert its own information into photons and vice versa. This implies that efficient coherent interaction between the system and the photon is essential. These two considerations lead to the idea of a quantum network where the atom-like systems act as the stationary node of the network for information processing and storage while the photons as the flying qubit in charge of information transfer [25, 26].

With all these considerations, we focus on exploring the feasibility of an optically confined single neutral ^{87}Rb atom to be the building block of such a quantum computer. A single two-level neutral atom is a relatively simple system to study and can be manipulated individually with high precision. With various trapping and cooling techniques, the atoms can be isolated almost entirely from the environment, which results in a long coherence time of the qubit [27]. Instead of placing the atom in a high finesse cavity to achieve strong atom-light coupling [28, 29], our approach involves a tightly focused light field onto the optically confined atom through a pair of aspheric lenses. The reason for such a choice is due to the simplicity of a lens system in terms of setting up. Besides, in the case of a quantum network formed by atom-cavity systems, it is a resource demanding task to make sure each of the nodes in the network is operating at the same resonant frequency.

In combination with various beam splitting controls and techniques, the optical dipole trap can be easily scaled up to realize an optical tweezer array that can hold a

large number of single neutral atoms in arbitrary 2D and 3D geometry [30–32]. The knowledge and experience in controlling single atoms to perform single qubit gate operation can be applied to the case of a tweezer array as high fidelity individual site addressing with negligible crosstalk between neighboring qubits can be realized with the same beam splitting controls and techniques. Combined with the strong long-range interactions provided by Rydberg states [33, 34], two- and three-qubit entangling gates have been successfully demonstrated [35–37], paving the way to a practical quantum computer. Recently, neutral-atom arrays that contain two different species of neutral atoms [38] and two different isotopes of Rubidium [39] have been demonstrated. This shows the robustness of the optical tweezer approach.

Early works in our group focus on how the temporal profile of the photons affects the interaction probability with an atom [40]. Subsequent efforts successfully demonstrated a 36.6(3)% extinction of a weak coherent field by a single atom trapped in free space [41]. In this thesis, we divert away from the path of investigating the atom-light interaction strength and start to look into some aspects of our qubit system that might matter in the implementation of a practical quantum interface.

Motivated by the choice of a closed optical transition in the previous experiments to achieve high interaction strength, we are curious about the coherence performance of the magnetically sensitive ground state qubit that is coupled to the closed optical transition. Through the application of a dynamical decoupling sequence to the qubit, we manage to preserve the coherence for a long enough time relative to the gate operation time.

While we have a good understanding of the atom-light interaction, the characteristic of the emission from the system remains unexplored. The frequency spectrum of the atomic fluorescence exhibits a triplet structure when the system is saturated by the incoming excitation. With off-resonant excitation, the preferred time-ordering of the photons emitted from different sidebands could be used as a heralded narrowband single photon source that might find applications in quantum information processing.

In the end, we start to consider the scaling up of our current system to increase the number of usable qubits. Inspired by the possibility of incorporating Rydberg excitation into our future experiment, we develop a dipole trap system based on a blue-detuned laser. With a bottle beam trap configuration, we can construct a trap

that will retain its trapping power for the atom in its ground state and Rydberg state simultaneously. This can avoid the situation where the red-detuned dipole trap needs to be turned off during the experiment time window when a Rydberg excitation occurs.

Thesis outline

This thesis is organized as follows:

- Chapter 2 describes the experiment setup and some key techniques for trapping the single ^{87}Rb atoms. We also include some characterization measurements such as atom lifetime and trap frequency measurement.
- Chapter 3 presents the theoretical description and experimental effort on the dynamical decoupling sequence. We explore different types of sequences and characterize their effectiveness in preserving coherence. An improvement over two orders of magnitude in the coherence time is observed by applying the optimal pulse sequence.
- Chapter 4 reports our observation of the Mollow triplet in the fluorescence spectrum from an optically confined single atom. The single photon nature of the fluorescence is illustrated in the second-order correlation measurement of the atomic emission. We show the preferred time-ordering of the photons originating from opposite sidebands under off-resonant excitation.
- Chapter 5 covers the working principle and characterization of blue-detuned bottle beam trap.
- Chapter 6 concludes our findings and discusses the future outlook of the experiment.

Chapter 2

Experimental setup and control of single atom

This chapter introduces the experimental setup and some key techniques for trapping single ^{87}Rb atoms. We briefly describe each key component: the aspheric lens pair, the laser system, and the far-off-resonant optical dipole trap (FORT). Next, we show the manipulation of the optically confined single atoms, which involves state detection and optical pumping to targeted states.

2.1 Overview

The schematic of our experimental setup is shown in Fig. 2.1. We trapped a single ^{87}Rb atom with FORT operating at a wavelength of 851 nm by strongly focusing the laser using an aspheric lens. In order to load atoms into the FORT, we first need to cool the atoms to a temperature below the trap depth of FORT, which is around $k_B \times 3$ mK in our setup. We first use a magneto-optical-trap (MOT) to form a cloud of atoms that is sufficiently cold and dense to be captured by the dipole trap. The atomic fluorescence scattered by the single atom is collected with the same pair of aspheric lenses, which then will be coupled into a single-mode fiber and subsequently detected with an avalanche photodetector.

2.2 Aspheric lens pair

A pair of high numerical aperture (NA) aspheric lenses in confocal configuration lies at the heart of our optical setup. Besides using these lenses to form the FORT,

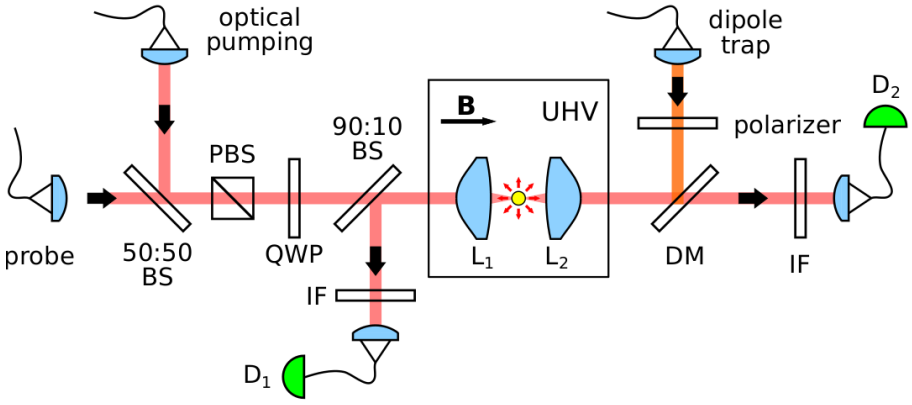

Figure 2.1: Setup for probing light-atom interaction in free space. A single ^{87}Rb atom is cooled and trapped at the focus of the far-off-resonance dipole trap (FORT) between two high NA lenses (L_1, L_2) within an ultra-high vacuum (UHV) chamber. Through the same lenses, we can strongly focus the probe beam onto the atom and collect the fluorescence emitted by the atom. The collected atomic fluorescence is coupled into a single-mode fiber and subsequently detected by avalanche photodetectors (APDs). IF: interference filter centered at 780 nm, QWP: quarter-wave plate, BS: beam splitter, PBS: polarizing beam splitter, $D_{1/2}$: avalanche photodetectors (APDs), B: magnetic field.

laser light can be tightly focused onto the single atom to realize strong atom-light coupling. The reason for us to choose aspheric lenses is their compactness and cheaper pricing compared to multi-element microscope objectives. We use aspheric lenses custom-made by Asphericon with a NA of 0.75 and an effective focal length of 5.95 mm. The lenses are coated with an anti-reflection coating with less than 0.5% reflection at 700-1400nm. For other technical details such as the mechanical mount and characterization of the lenses, one can refer to Wilson's PhD thesis [42].

2.3 Laser system

Lasers are utilized throughout the experiment for many different purposes such as trapping, cooling, and exciting the atom. Several lasers are used in the setup including (1) a 780 nm laser for cooling and probing, (2) a 795 nm laser for repumping, (3) another 780 nm laser for clock state optical pumping, and (4) an 851 nm laser for atom trapping. For the first two lasers, all the technical details such as the laser configuration and spectroscopy for frequency locking have been covered in a previous thesis [42] and no change has been made to them. While the other two

lasers are the new addition to the setup, we will briefly describe their purpose and configuration in the following section.

Clock state optical pumping laser

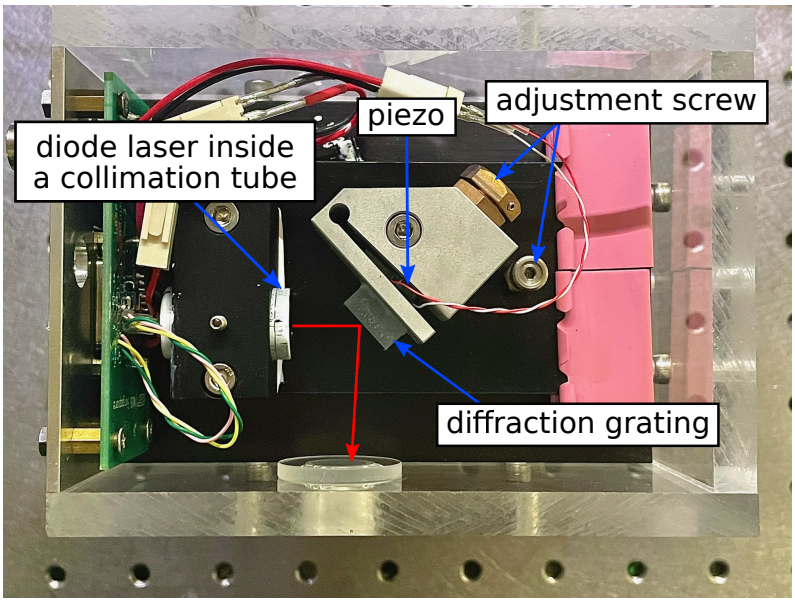

Figure 2.2: A photo of the home-built external cavity diode laser setup inside an acrylic box. The red colour line is drawn as a visual aid to indicate the beam path from the diode laser reflected by the diffraction grating. The two adjustment screws help to adjust the alignment of the grating in both vertical and horizontal directions in order to form a cavity. The piezo that is attached to the grating mount provides a change in the cavity length which turns into a change in laser output frequency.

This laser is a home-built external cavity diode laser (ECDL) in a Littrow configuration [43, 44] with a laser diode from Thorlabs (L785P090). As shown in Fig. 2.2, the ECDL is enclosed in a box with a temperature control system. Together with the diode laser, the reflective diffraction grating forms an external cavity that narrows down the laser linewidth by yielding feedback to the laser diode and amplifying a single frequency mode. The coarse wavelength tuning (>100 GHz) is achieved by tuning the temperature through a Peltier element and adjusting the diffraction angle of the grating via an adjustment screw. For fine-tuning(<1 GHz), the external cavity length can be changed by the piezo that is attached to the grating mount which results in a change of the cavity resonance. With this configuration, the ECDL can achieve a laser linewidth of less than 1 MHz. With an operating

current of 60 mA, the output optical power of this ECDL is 30 mW which is more than enough for our daily operation.

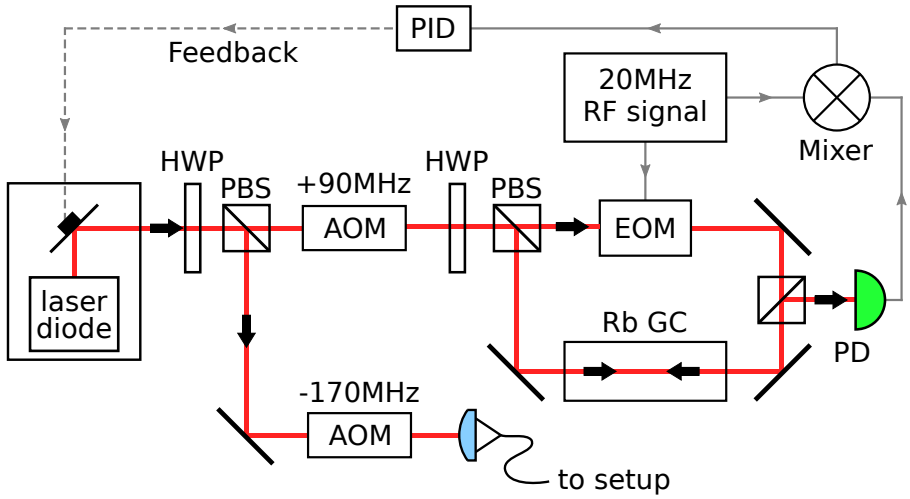

Figure 2.3: Setup of the clock state optical pumping laser. The combination of a half-wave plate (HWP) and a polarizing beam-splitter (PBS) distributes the laser output into two paths. In the first path, an acousto-optic modulator (AOM) increases the laser frequency by 90 MHz before going into the modulation transfer spectroscopy (MTS) port. In MTS, the phase of the pump beam (top path) is modulated by an electro-optic modulator (EOM); the modulation is transferred to the probe (bottom path), and subsequently detected by the photodetector (PD). This signal is mixed with the RF signal to generate error signals. A proportional–integral–derivative (PID) controller turns this signal into a feedback to the ECDL piezo to lock the laser to a target frequency. By locking it to the $5^2S_{1/2}, F = 2 \rightarrow 5^2P_{3/2}, F' = 3$ transition, the output frequency of the laser is now 90 MHz below this transition. It is further decreased by 170 MHz using another AOM such that the light is now resonant with $F = 2 \rightarrow F' = 2$ transition.

We need this separate laser because the main 780 nm laser in the system does not have excess laser power to spare for clock state optical pumping purposes. As shown in Fig. 2.3, the laser frequency is first increased by 90 MHz via an acousto-optic modulator (AOM) from Gooch & Housego (3080-122). Using a modulation transfer spectroscopy (MTS), the laser is frequency-locked to the ^{87}Rb D_2 line, specifically the $5^2S_{1/2}, F = 2 \rightarrow 5^2P_{3/2}, F' = 3$ transition. The laser frequency is now 90 MHz below the $F = 2 \rightarrow F' = 3$ transition. It is further decreased by 170 MHz by another AOM in a double pass configuration such that the light resonates with the $F = 2 \rightarrow F' = 2$ transition for optical pumping purposes. The exact frequency is

fine-tuned depending on the experimental setting such as trap depth and magnetic field that caused frequency shifts.

Dipole trap laser

For our red-detuned far-off-resonant optical dipole trap (FORT), we are using a continuous-wave (CW) Ti:Sapphire laser (SolsTiS) from M Squared where we set the lasing wavelength at 851 nm. This Ti:Sapphire laser is pumped by a 532 nm laser (Verdi V-10). With pump power of 10 W, the laser has an average output power of 1.5 W depending on the emission wavelength. The advantages of using this laser is the stability in terms of power and the single-mode operation. To further stabilize and adjust the trapping potential, we lock the power of this laser with a PID control loop. By doing so, not only that we can maintain a consistent trap potential over a long period of time, but the trap depth can also be tuned reliably according to the experimental sequences.

For the experiment that is described in Chapter 5, the blue-detuned dipole trap is generated using the same Ti:Sapphire laser with the emission wavelength tuned to 740 nm. So we use a distributed feedback laser (Eagleyard EYP-0852-00150) to form the red-detuned FORT to replace the original trap. This new FORT has the same power stabilization setup as the previous one.

2.4 Far-off-resonant optical dipole trap

A far-off-resonant optical dipole trap (FORT) is formed by strongly focusing down a far-detuned laser beam in order to create a large enough intensity gradient around the focus. The interaction between the light field and the atomic dipole moment leads to the presence of AC Stark shifts in the atomic energy levels. This interaction is attractive if the light field is red-detuned with respect to the atomic transition and vice versa. As such, a tightly focused red-detuned laser creates a potential well that pulls the atom towards the region of maximal intensity at the focal spot.

The dipole potential has a depth that is approximately proportional to I/Δ whereas the scattering rate of the trap light by the atom scales with I/Δ^2. Here, I is the intensity of the trap light, and Δ is the detuning from the atomic transition.

In order to reduce the influence of the dipole trap on the atomic states and atom temperature, a large detuning is preferred to lower the scattering rate of the trap light by the atom. On the other hand, higher optical power is needed to obtain a certain trap depth with larger detuning due to the I/Δ scaling. In our experiment, the aspheric lenses are designed to perform at the diffraction limit for light with a wavelength of 780 nm. We choose to use 851 nm as the dipole trap wavelength such that the trap beam can still be focused down near to diffraction limit and have a low scattering rate due to the large detuning (60 nm).

2.4.1 Experimental Implementation

The output of the Ti:Sapphire laser is sent into an AOM and subsequently coupled into a polarization-maintaining single-mode fiber for a clean spatial and polarization mode. At the other end of the fiber, we use a triplet fiber collimator from Thorlabs to obtain a collimated beam with a beam waist of 2.7 mm. Since the laser power is directly related to the trap potential experienced by the atom, it is crucial for the laser power to stay constant over time. Part of the laser is sent onto a photodiode for power stabilization purposes, where a control loop is controlling the radio frequency (RF) power supplied to the AOM based on the photodiode readout. After that, the beam is focused down through the same aspheric lens pairs for strong atom-light coupling to a waist of approximately 1.1 μm.

The typical operating power of the dipole laser is around 12 mW, which corresponds to a trap depth of $U_0 \simeq k_B \times 2.8\,\mathrm{mK}$. We use a FORT that is linearly polarized, where the vector light shift vanishes and the qubit coherence can be preserved for a longer time [27]. It is also essential for efficient polarization gradient cooling [45]. However, the presence of tensor light shift in linearly polarized FORT greatly affects the atom-light coupling [46]. In daily operation, we have to lower the trap depth to around $k_B \times 1.2\,\mathrm{mK}$ and apply a strong bias magnetic field along the quantization axis to retain a strong and clean atom-light coupling.

Thanks to the collisional blockade mechanism [47], a dipole trap that is strongly focused can only hold a single atom at one time. When two atoms are loaded into the trap, both of them will be rejected out of the trap due to light-assisted collisions, which result in zero atom within the dipole trap. By spatially overlapping the MOT

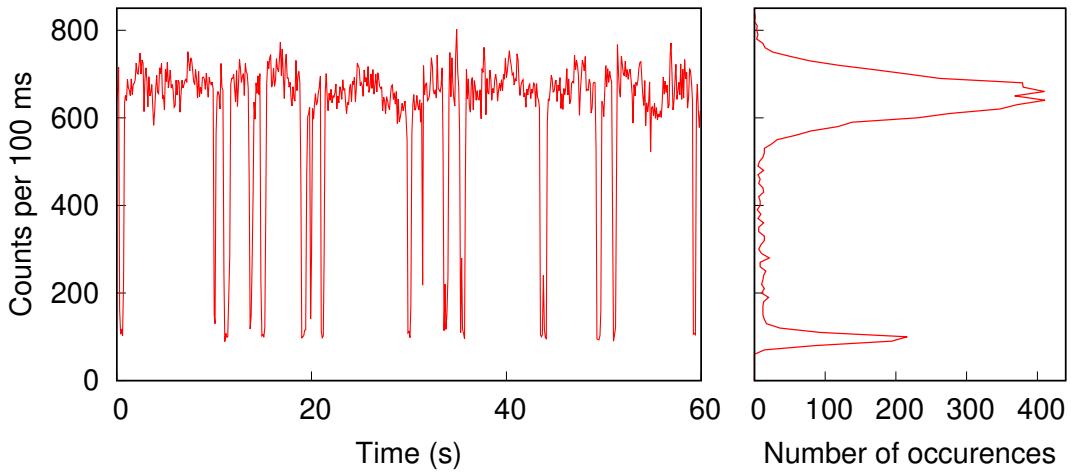

Figure 2.4: Fluorescence signal of single atoms in an optical dipole trap with the MOT always turned on. (Left) Typical telegraph signals of single atom fluorescence with a lower background level and a higher level indicate the presence of one atom in the trap. (Right) Histogram of the fluorescence by collecting data over 10 minutes.

and the FORT, a single ^{87}Rb atom can be loaded into the FORT from the atomic cloud. The fluorescence scattering by the atom is collected by the aspheric lens pair and subsequently coupled into single-mode fibers. We detect the collected fluorescence using single photon detectors (Perkin Elmer SPCM-AQR-15). Figure 2.4 shows the typical telegraph signal that indicates the sub-Poissonian loading of single atoms with either zero or one atom inside the trap.

This fluorescence signal that has two discrete levels to indicate the presence of an atom in the trap. We can use a threshold count rate that acts as a trigger to begin the experimental sequence. In our setup, we use a pattern generator device with a counter to check the fluorescence count rate and implement the experimental sequence condition on the count rate. It takes around 30 ms of fluorescence collection to have sufficient information to distinguish if there is an atom in the trap reliably.

2.4.2 Trap Characterizations

Using a focused Gaussian laser beam, the spatial distribution of the FORT potential with trap depth U_0 can be described in cylindrical coordinates as

$$U(\rho, z) = -U_0 \frac{1}{1 + (z/z_R)^2} \exp\left[-\frac{2\rho^2}{w_D^2(1 + (z/z_R)^2)}\right], \tag{2.1}$$

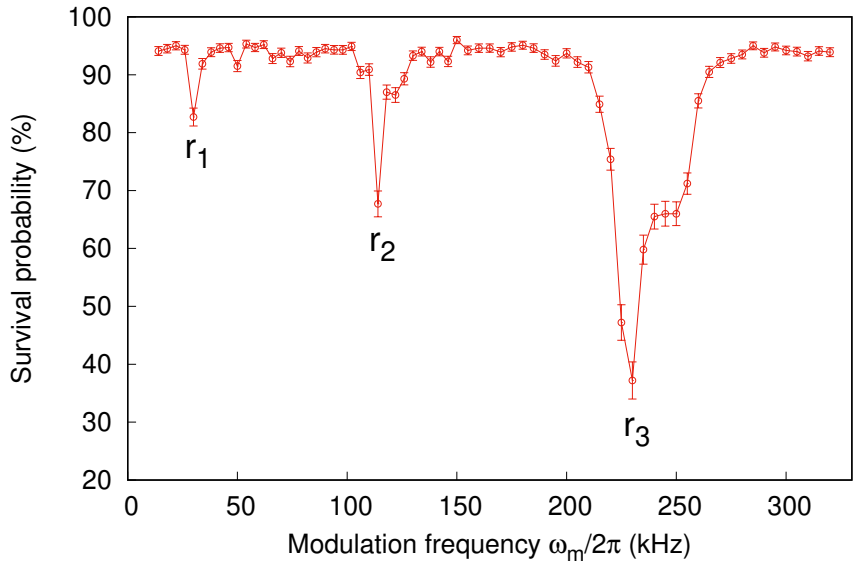

Figure 2.5: Survival probability of the atom in the FORT when the trap is modulated at different frequencies. Parametric resonances lead to the dips in the survival probability. The parametric resonances are $r_1 = 2\omega_z/2\pi$, $r_2 = 2\omega_r/4\pi$ and $r_3 = 2\omega_r/2\pi$, which give us $\omega_z/2\pi$=15(1) kHz and $\omega_\rho/2\pi$=115(2) kHz.

where w_D is the beam waist and $z_R = \pi w_D^2/\lambda$ denotes the Rayleigh range of the laser beam. For a cold atom with a thermal energy $k_B T$ much lower than the trap depth U_0, it will mostly reside near the bottom of the potential. In this case, the trap potential can be approximated as a harmonic potential:

$$U(\rho, z) \approx -U_0[1 - 2(\frac{\rho}{w_D})^2 - (\frac{z}{z_R})^2]. \tag{2.2}$$

and the trap frequencies are given by $\omega_r = (4U_0/mw_D^2)^{1/2}$ and $\omega_z = (2U_0/mz_R^2)^{1/2}$ in the radial and axial direction, respectively.

In order to measure the trap frequencies, we heat up the atom parametrically by modulating the dipole trap power. This is done via modulation of the RF input power to the trap laser AOM. By varying the modulation frequency ω_m, we observe a degradation of the atom survival probability in the trap when the modulation frequency hits one of the parametric resonances,

$$\omega_n = \frac{2\omega_{\rho/z}}{n}, n = 1, 2, 3, \ldots \tag{2.3}$$

From the trap frequency measurement shown in Fig. 2.5, we observe three parametric resonances. We infer an axial trap frequency of $\omega_z/2\pi$=15(1) kHz from resonance r_1. For radial direction, r_2 and r_3 are the resonances when n equal to 1 and 2, respectively. From this, we infer a radial trap frequency of $\omega_\rho/2\pi$=115(2) kHz.

2.4.3 Atom lifetime in the trap

The lifetime of the trapped single atom is an important measure of the optical dipole trap performance. A longer lifetime allows us to execute more experimental cycles on the atom without the need to constantly wait for an atom to load into the trap.

We can infer the lifetime of the single atoms in the trap from the survival rate of the atom after a certain period. When the collected fluorescence exceeds the threshold, a single atom is loaded into the trap and we will switch off the MOT by turning off the quadrupole field. This will help to prevent atom loss due to collision with other atoms. After waiting for a certain duration, we will check if the atom is still present in the trap by checking the integrated fluorescence counts for 30 ms. This measurement is repeated for different duration to get the survival rate of the atom.

We perform the experiment under two different conditions: with and without the presence of cooling light during the waiting period. In the case where the cooling light is absent, the lifetime is mainly limited by collisions of the trapped atom with the background gas. While for the case where the trapped atom is under continuous illumination of the cooling light, the spontaneous scattering of the cooling light will heat up the atom and contribute to a shorter lifetime in the trap. The result of the single atom lifetime under two different conditions is shown in Fig. 2.6. We fit the experimental data to an exponential decay and obtain the $1/e$ lifetime of 2.77(4) s for the single atom in the FORT without the presence of cooling light. In the case of continuous illumination by the cooling light, the lifetime is reduced to 1.61(4) s due to heating effect from the photon scattering. In any case, these lifetimes are sufficient for our purposes as they are a few orders of magnitudes higher than the timescale needed for most of the experimental sequences.

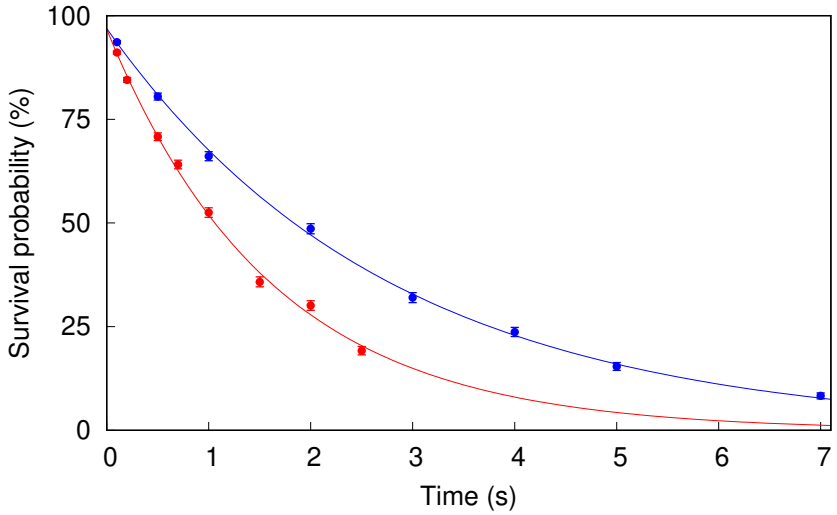

Figure 2.6: Trapping lifetime of single atoms in an optical dipole trap with (red) and without (blue) the continuous illumination of the cooling light. The solid lines are exponential fits that result in $1/e$ lifetime of 1.61(4) s (red) and 2.77(4) s (blue) when cooling light is turned on and off, respectively. The error bars reflect the standard error of binomial statistics.

2.5 Manipulation of single atoms

In this section, we will describe the experimental sequences that we implement routinely in our setup. First, we will explain the procedures to prepare the trapped atom in the desired state and how we measure it.

2.5.1 Experimental sequences

We use a field-programmable gate array (FPGA) based pattern generator to aid us in realizing the sequences in all the experiments throughout this thesis. This pattern generator has multiple outputs that send out electrical logic signals according to the sequences that we programmed. These signals are used to turn on and off devices in the setup such as AOMs and coils that generate quadrupole and bias magnetic fields.

Fig. 2.7 outlines the logic flow of the experimental sequence we carry out routinely. At the initial stage, we turn on the MOT (quadrupole field, cooling, and repump laser) and the dipole laser to wait for a single atom to load into the trap. Due to the sub-Poissonian loading as shown in Fig. 2.4, the sudden increase in photon scattered

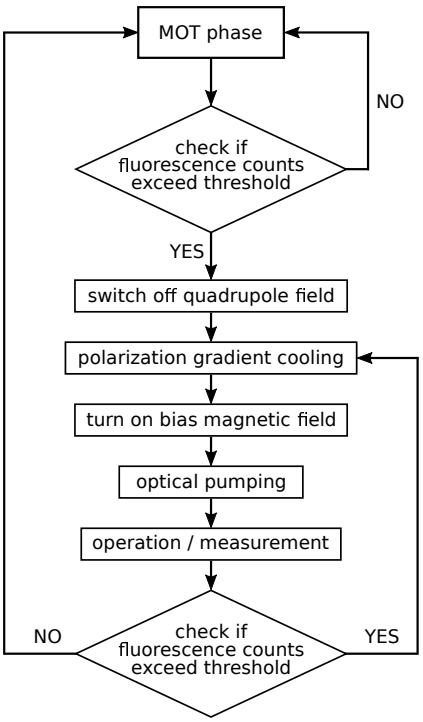

Figure 2.7: Flow chart of the experimental sequence.

from the cooling light indicates the presence of a single atom in the dipole trap. We can set a threshold in the sequence to decide if it will continue with the MOT phase or jump to the main experimental sequence. The pattern generator has a built-in counter that will integrate the photodetection events for a certain duration, and check if the counts exceed the threshold value. The typical duration that we use in the experiments is around 20 ms to 40 ms so that we have enough fidelity to distinguish the presence of an atom within the trap. If the counts do not exceed the threshold, this checking procedure will be repeated until the threshold is reached.

When the fluorescence counter exceeds the threshold, we will switch off the quadrupole field to prevent further loading of atoms into the trap. Next, we perform polarization gradient cooling (PGC) by lowering the power in the MOT beams for 10 ms. This helps to cool the atom down to a temperature of 14.7(2) μK. A bias magnetic field of 1.44 mT is applied along the FORT laser propagation direction to lift the degeneracy of the Zeeman states. According to the requirements of different experiments, the atom is optically pumped into the target state by an optical pumping beam.

Now, we can start applying different steps and operations to the atom. Depending on the goal of the experiment, we can program the sequence to fulfill our needs such as transmission measurement or coherence measurement. The details of the sequence will be described in the corresponding section in the later part of this thesis. At the end of the sequences, we will turn on the cooling laser to check if the atom is still in the trap by comparing the fluorescence counts with the set threshold. The sequence will return to the atom preparation stage (PGC stage) if the atom survives, otherwise it will return to the MOT phase.

This deterministic way of atom loading and performing the experimental sequence is more efficient in terms of data collection compared to the method that repeats the measurement sequence and post-process to isolate the data that are collected when the atom is present. We run a small test to quantify the efficiency of this method. To simulate the situation where the experimental sequence does not condition on the presence of the atom in the trap, we turn on the MOT and dipole laser for 500 ms, then we switch off the MOT for 50 ms to represent the time window where the state preparation and measurement are happening. After that, we turn on the MOT beam for 30 ms to check if there is atom within the trap by looking at the fluorescence from the atom. Then, the sequence will return back to MOT phase for 500 ms. If the atom is present, we consider that as one useful atombin. For a collection time of 10 minutes, the experimental sequence that condition on the presence of the atom results in 11 times more atombins compared to the sequence that does not.

2.5.2 Atomic state detection

The ^{87}Rb $5^2S_{1/2}$ ground state consists of two hyperfine states with total angular momentum $F = 1$ and $F = 2$, respectively. The method to distinguish these two hyperfine states reliably is crucial in identifying the atomic superposition state involved in the coherence measurement presented in the next chapter. Here, we follow the nondestructive state detection scheme illustrated in [48, 49] to verify the hyperfine state of the atom. This scheme requires shining light onto the atom to excite the transition from $5^2S_{1/2}, F = 2$ to $5^2P_{3/2}, F' = 3$ and subsequently detect the atomic fluorescence. Atoms that are initially in the $F = 2$ (bright) state will continuously scatter light, whereas for atoms in the $F = 1$ (dark) state, there is no

coupling to the light field and no light is being scattered. As such, the presence or absence of fluorescence above a given threshold reveals the hyperfine state that the atom is in.

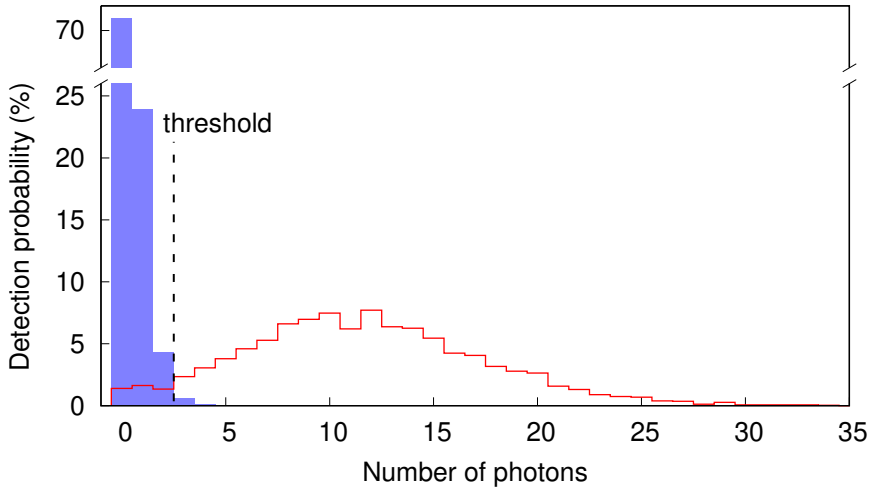

Figure 2.8: Histogram for photon detection probability for atoms prepared in a bright state (red) and a dark state (blue), respectively. The state readout fidelity is 97.4(2) % for a set threshold of 3 detected photons.

The detection performance is characterized by first preparing the atom in either the bright or dark state, and then turn on the state detection light for 600 μs. This pulse duration is chosen such that the atom heating is minimal while the state detection fidelity is high to accurately identify the hyperfine state. We repeat this procedure and analyze the photon distribution of the collected fluorescence for cases where the atom is either initialized in the bright or dark state. Fig. 2.8 shows the distribution of the detected photon number for 2800 experimental cycles with two distinguishable peaks. When the atom is prepared in the bright state, the detectors record a mean photon number $n_b = 11.7(1)$ in the 600 μs collection window. For an atom in the dark state, we expect the atom to scatter almost no photons due to the hyperfine splitting of 6.8 GHz. However, we find that in the experiment, the detectors occasionally register one or two events during the detection window (mean photon number $n_d = 0.36(1)$) due to the APD dark counts. From the histogram, we can choose a threshold photon number n_{th} that maximizes the discrimination between the two hyperfine states.

In order to characterize the state detection performance, we define the state readout fidelity as

$$F = 1 - \frac{\xi_b + \xi_d}{2}, \tag{2.4}$$

where $\xi_{b(d)}$ is the probabilities of a state assignment error for atoms prepared in the bright (dark) state given a certain n_{th}. For the data shown in Fig. 2.8, the ξ_b and ξ_d is 4.4(4)% and 0.8(2) % respectively, using $n_{th} = 3$. With this, we achieve a detection fidelity of $F = 97.4(2)\,\%$. The high-fidelity single-shot readout potentially enables quantum state manipulation without further averaging.

2.5.3 Optical pumping

After the initial trapping and PGC stage, the atomic state is spread across all the Zeeman sublevels in both the hyperfine states of $5^2S_{1/2}$ ground state. We therefore perform optical pumping to ensure that the atom is initialized in the desired state. Throughout this thesis, we mainly work with the closed transition $5^2S_{1/2}, F = 2, m_F = -2 \rightarrow 5^2P_{3/2}, F' = 3, m_F = -3$. As such, we want to prepare the atom in the $F = 2, m_F = -2$ state most of the time. With the exception in Section 3.2.3 where we measure the coherence of the clock state transition, the atom needs to be prepared in the magnetically insensitive Zeeman state, $5^2S_{1/2}, F = 2, m_F = 0$. In both cases, we apply dark-state optical pumping to minimize the photon scattering such that excessive heating of the atom is avoided.

To initialize the atom in the $F = 2, m_F = -2$ state, we send in two σ^- polarized light beams along the optical axis. These two beams are on resonance with the $5^2S_{1/2}, F = 2 \rightarrow 5^2P_{3/2}, F' = 2$ and the $5^2S_{1/2}, F = 1 \rightarrow 5^2P_{1/2}, F' = 2$ transitions, respectively. The first beam (pump) drives the atom towards the target state, while the second beam (repump) brings the atom back to the $F = 2$ state when the atom decays to the $F = 1$ state and decouples from the pump beam. After multiple excitations, the atom is now in the desired $F = 2, m_F = -2$ state which is decoupled from the pumping light. As such, the atom will not scatter photons anymore once it falls into this "dark state". In our experiment, the atom takes around 1 to 2 ms to reach the "dark state" through this optical pumping process.

For the preparation of the atom in the $F = 2, m_F = 0$ state, we change the configuration of the pump by sending in the beam perpendicularly to the optical

axis. This light is linearly polarized parallel to the optical axis in order to drive the π-transition from $5^2S_{1/2}, F = 2$ to $5^2P_{3/2}, F' = 2$. When the atom decays to the $m_F = 0$ state, it will be decoupled from the pump light because the transition $5^2S_{1/2}, F = 2, m_F = 0 \rightarrow 5^2P_{3/2}, F' = 2, m_{F'} = 0$ is forbidden due to the selection rules for atomic dipole transitions. Together with the same repump light, we can prepare the atom in the desired clock state without excessive photon scattering.

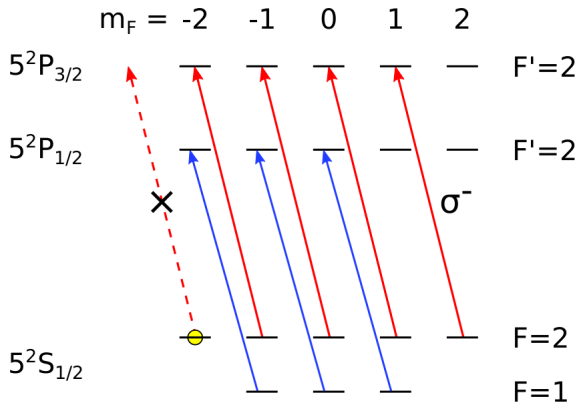

Figure 2.9: Optical pumping scheme to initialize the atom into the $5^2S_{1/2}, F = 2, m_F = -2$ state. When the atom reaches the target state, it is decoupled from the pumping field as no allowed σ^- transition exists. The circularly σ^- polarized 780 nm (795 nm) pumping (repumping) field is indicated by the red (blue) arrows.

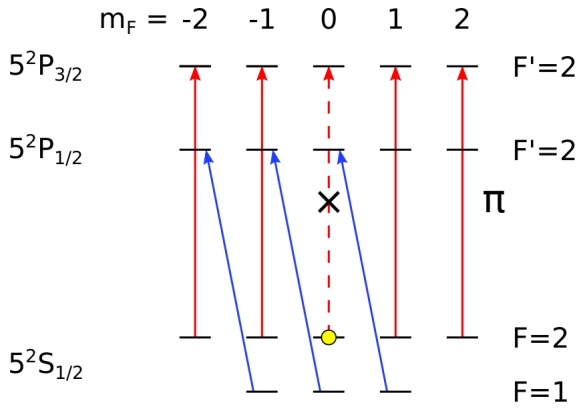

Figure 2.10: Optical pumping scheme to initialize the atom in the magnetically insensitive $5^2S_{1/2}, F = 2, m_F = 0$ state. Due to the selection rule for dipole transition, the atom in the target state will be decoupled from the pumping field. The linearly π polarized 780 nm pumping field is indicated by the red arrows while the blue arrows show the same repumping field as in Fig. 2.9.

Chapter 3

Dynamically decoupled single neutral atom

This chapter describes the experimental implementation of dynamical decoupling schemes on a single ^{87}Rb atom in a tightly focused far off-resonant optical dipole trap (FORT). First, we give a brief overview of dynamical decoupling as a tool to maintain the coherence of a quantum system for a longer period of time. Next, we characterize the atomic coherence by driving Rabi oscillations and perform Ramsey and spin-echo measurements. This result also serves as a reference to show the effectiveness of different dynamical decoupling sequences in mitigating decoherence. The subsequent section will focus on applying a few dynamical decoupling sequences onto the atom and determining the coherence time. We also observe a strong correlation between the motional states of the atom and the qubit coherence after the sequences are applied, which can be used as a measurement basis to resolve trapping parameters such as trap frequency. Finally, we also present a measurement to determine the optimal pulse sequence for our system by mapping out the coherence with 5 π-pulses at the different durations between pulses. A majority of the content in this chapter has been published in [50].

3.1 Introduction

Quantum computation which utilizes quantum bits to process and store information holds the potential to tackle some of the most complex computational problems more effectively than classical computers [51, 52]. However, one restriction that hinders the realization of this potential is the undesired coupling between the quantum

system and the external environment which causes the loss of information [53]. This degradation of the quantum state is called decoherence, and it limits the number of gate operations that can be applied to the qubit, as well as the duration the quantum information can be preserved [54, 55]. In order to suppress the decoherence process, one of the most effective approaches is dynamical decoupling (DD). This method is accomplished by applying a series of π pulses to the system, which overcomes the decoherence by inverting the interaction between the system and the environment [56, 57]. The DD scheme was first established in the nuclear magnetic resonance (NMR) community. One of the more well-known implementations is the Hahn echo sequence proposed by Erwin Hahn [58]. He showed that flipping a qubit with a π pulse is equivalent to a change of sign of the system-environment interaction Hamiltonian. This in turn corresponds to a time reversal of the perturbation, effectively decoupling the system from the noise-inducing environment. Since then, many DD schemes with different pulse sequences such as Carr-Purcell (CP) and Carr-Purcell-Meiboom-Gill (CPMG) have been introduced to address various sources of errors.

3.1.1 Dynamical decoupling

Consider a system that consists of a qubit that is coupled to an external environment which imparts a random phase onto the qubit. The qubit can be described as a superposition state

$$|\Psi(t)\rangle = c_{\downarrow}(t)\,|\downarrow\rangle + c_{\uparrow}(t)\,|\uparrow\rangle\,, \tag{3.1}$$

where $|\downarrow\rangle$ and $|\uparrow\rangle$ are the basis states of the qubit. The complex probability amplitudes $c_{\downarrow}$ and $c_{\uparrow}$ are normalized such that $|c_{\downarrow}|^2 + |c_{\uparrow}|^2 = 1$. Undesirable coupling to the environment will result in the loss of state information that is encoded in $c_{\downarrow}$ and $c_{\uparrow}$. In general, one may classify decoherence processes into two classes: longitudinal energy relaxation and transverse dephasing. The first process affects the probability amplitudes of $|\Psi\rangle$ and causes the qubit state to evolve along the meridians of the Bloch sphere. This results in a flip of the qubit state ("bit-flip error"). The longitudinal relaxation process can be characterized by an energy relaxation time, T_1 with reference to NMR literature [59].

As compared to energy relaxation, transverse dephasing randomizes the relative phase between the basis states. This causes the qubit state to move along the

latitude lines of the Bloch sphere. When we average the data collected from multiple experimental runs, the phase randomization results in decoherence with a characteristic time T_ψ. Taking these two decoherence processes into account, the coherence time of the qubit system can be shown to be $(T_2^*)^{-1} = (2T_1)^{-1} + T_\psi^{-1}$. In reality, T_2^* of the qubit can be measured through the Ramsey decay. We can reverse the transverse dephasing with some coherence preserving protocols and achieve a longer coherence time T_2 of the qubit.

However, the longitudinal relaxation process is generally much slower than the transverse dephasing in our system. Therefore, we can write down a Hamiltonian that models decoherence in our system as follow:

$$H = \frac{\hbar}{2}[\omega_0 + \xi(t)]\hat{\sigma}_Z, \tag{3.2}$$

where ω_0 is the unperturbed energy splitting of the qubit, and ξ is a classical random variable describing the variation of the qubit energy splitting due to the environment.

Given the relatively longer energy relaxation time T_1, we are interested in the decoherence process of a qubit that is in the coherent superposition of its ground and excited state. Consider a state at time $t = 0$, $|\Psi_0\rangle$ that is initially oriented along the y-axis of the Bloch sphere, where $|\Psi_0\rangle = \frac{1}{\sqrt{2}}(|\uparrow\rangle + i\,|\downarrow\rangle)$. $|\Psi_0\rangle$ can be prepared by initializing the qubit in $|\uparrow\rangle$ state and apply a $\pi/2$-pulse around the x-axis to rotate the state to y-axis. After that, we let the qubit evolve freely for a time t. The resulting state under the effect of Eqn. 3.2 is given by

$$|\Psi(t)\rangle = \frac{1}{\sqrt{2}}\left(e^{-i\omega_0 t/2}e^{-\frac{i}{2}\int_0^t \xi(t')dt'}\,|\downarrow\rangle + ie^{i\omega_0 t/2}e^{\frac{i}{2}\int_0^t \xi(t')dt'}\,|\uparrow\rangle\right). \tag{3.3}$$

From Eqn. 3.3, we can see that accumulation of random phase between $|\uparrow\rangle$ and $|\downarrow\rangle$ happens due to the contribution of the $\xi(t)$ term. This decoherence process of the qubit can be visualized in the Bloch sphere picture as shown in Fig. 3.1. Ideally, when ξ is zero, the initial state that lies on the y-axis will evolve to $|\downarrow\rangle$ if we apply another $\pi/2$-pulse around the x-axis. However, the state now starts to rotate about the z-axis with a rotation speed that depends on $\xi(t)$. The additional phase makes the state fail to reach $|\downarrow\rangle$ completely even though another $\pi/2$-pulse is applied.

Instead of applying $\pi/2$-pulse, we let the state freely evolve and apply a π pulse around the x-axis (denoted as π_x) at $t = \tau/2$ which corresponds to a rotation of 180° with respect to the x-axis. This will result in a time reversal of the phase

accumulation and "refocus" the qubit back to its desired state at $t = \tau$. This is the basic idea of the Hahn spin echo, a pioneering strategy for tackling decoherence in the NMR community.

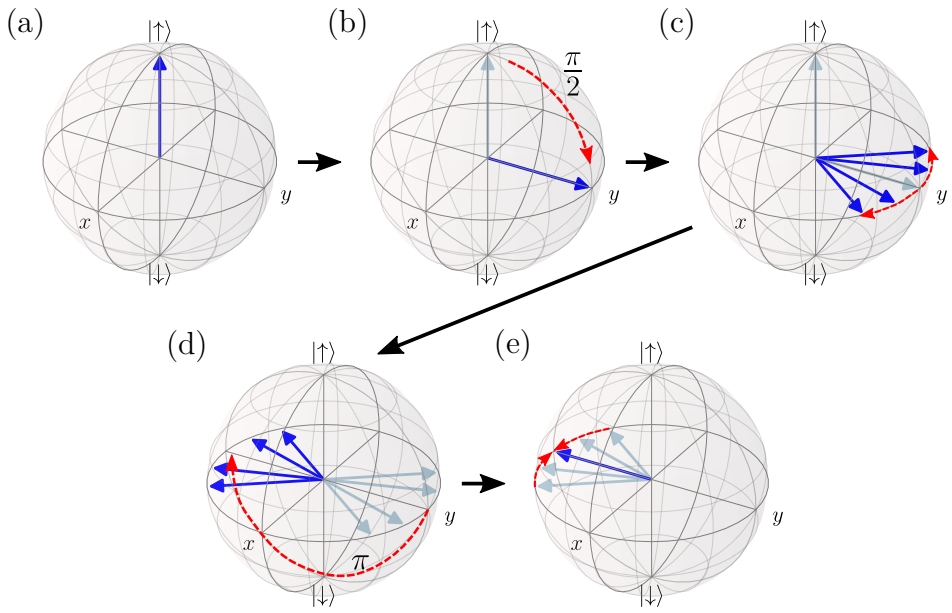

Figure 3.1: Visualization of Hahn spin echo in Bloch sphere. (a) Initialize the qubit in $|\uparrow\rangle$ state. (b) A $\pi/2$-pulse around the x-axis is applied to bring the state to the y-axis. (c) Let the qubit evolves freely for time t. The state starts to spread across the $x - y$ plane with a speed that depends on $\xi(t)$. (d) A π pulse around the x-axis is applied to flip the state to the opposite side of the Bloch sphere. (e) After another time t, the state is refocused back onto the y-axis.

However, this idea will only work under the assumption that the changes in ξ are slow compared to the free-precession time of the state. As such, this refocusing effect will also decay as a function of the free-precession time, where the decoherence effect cannot be reversed due to fluctuation of ξ. To bypass this limitation, Carr and Purcell proposed an extension of the Hahn spin echo sequence which is known as the Carr-Purcell (CP) sequence [56]. In this sequence, the single π pulse is being replaced by a series of equidistant π pulses, which effectively partition the changes in ξ into multiple time windows and reverse their effect accordingly with each π pulse.

Theoretically, one can add more π pulses in order to make sure the pulse intervals are below the correlation time of the fluctuations. In reality, the number of pulses

is limited by the accumulation of pulse errors which will eventually destroy the coherence of the system instead of preserving it. Meiboom and Gill [57] introduce Carr–Purcell–Meiboom–Gill (CPMG) sequence which is a variation of the CP sequence where the π pulses are applied around the y-axis (denoted as π_y) is introduced to mitigate the pulse errors.

Later on, Uhrig proposed the Uhrig dynamical decoupling (UDD) sequence which has non-equidistant pulse spacings, where its j-th π pulse located at $\delta_j\tau$ with $\delta_j = \sin^2[\pi j/(2N+2)]$ [60]. Here, τ is the total free evolution time and N is the total number of π pulses. We will examine the efficiency of various DD strategies in the subsequent sections.

3.1.2 Filter theory

The effect of various decoupling pulse sequences on the decoherence rate of the target system can be understood analytically using filter theory [60–62]. As shown in the previous section, the DD sequence modulates the phase accumulation of the qubit temporally by partitioning the free evolution time into smaller time bins. While the slow fluctuation of $\xi(t)$ can be corrected by the applied π-pulses, the fluctuation that occurs at a higher frequency will cause the qubit to dephase irreversibly. As such, it is helpful to view this problem in the frequency domain where the DD sequence can be treated as a spectral filter to separate the system from the environmental noise, depending on the various frequency components of $\xi(t)$. Here we use a formulation to describe the decoherence of a qubit system as presented in [60, 63, 64].

Due to transverse dephasing, the qubit state accumulates random phases over time due to its coupling with the external environment. This is the dominant factor that decreases the state coherence $W(\tau)$ after a duration τ. For a state $|\Psi_0\rangle$ initialized along the y-axis of the Bloch sphere, the state coherence $W(\tau)$ is given by

$$W(\tau) = |\overline{\langle\sigma_y(\tau)\rangle}| = e^{-\chi(\tau)}, \tag{3.4}$$

where the angled brackets represent a quantum-mechanical expectation value and the overline represents a statistical average.

To qualitatively understand the efficiency of multipulse sequences on dephasing suppression, we focus on the change in the state coherence integral $\chi(\tau)$. For a state

initialized in the equatorial plane of the Bloch sphere, we can write

$$\chi(\tau) = \frac{2}{\pi}\tau^2 \int_0^\infty S(\omega) g_N(\omega, \tau) d\omega, \tag{3.5}$$

where $g_N(\omega, \tau)$ can be viewed as a frequency-domain filter function of the random phases for a refocusing sequence consisting of N π-pulses, and $S(\omega)$ is the power spectral density of environmental noise in the semiclassical picture. This quantity describes the overlap between the filter function of the decoupling sequence and the power spectral density of environmental noise.

In order to obtain the power spectral density of environmental noise, we apply a Fourier transform to the time-dependent noise term $\xi(t)$:

$$S(\omega) = \int_{-\infty}^{\infty} e^{-i\omega t'} \langle \xi(t + t')\xi(t') \rangle \, dt'. \tag{3.6}$$

This power spectral density represents the ensemble-averaged phase accumulated between the basis states.

The decoupling sequence that contains a series of π-pulses modulates the phase accumulation of the qubit in the time domain. By applying Fourier transform to the temporal modulation, we can treat the DD sequence as a frequency-domain filter function, $g_N(\omega, \tau)$ that can decouple the system from the environmental noise depending on the shape of the filter. Depending on the distribution of N π-pulses within the free-induction time τ, $g_N(\omega, \tau)$ can be written as

$$g_N(\omega, \tau) = \frac{1}{(\omega\tau)^2} \Big| 1 + (-1)^{1+N} e^{i\omega\tau} + 2 \sum_{j=1}^{N} (-1)^j e^{i\omega\delta_j\tau} \cos(\omega\tau_\pi/2) \Big|^2, \tag{3.7}$$

where $\delta_j \in [0, 1]$ is the normalized position of the centre of the jth π-pulse in the free-induction time window and τ_π is the length of the π-pulses.

Figure 3.2 illustrates the filter properties of function $g_N(\omega, \tau)$ for two common DD sequences that will be implemented in the system. For a fixed free evolution time τ, the filter function's peak frequency shifts higher as N increases, leading to a reduction of integrated low-frequency noise. The filter function gets narrower and is centered closer to $\omega = N\pi/\tau$ as N increases.

With the knowledge of the spectral density of noise coming from the environment, one can utilize the filter treatment to calculate or construct DD sequences that are optimized to preserve the coherence of the system.

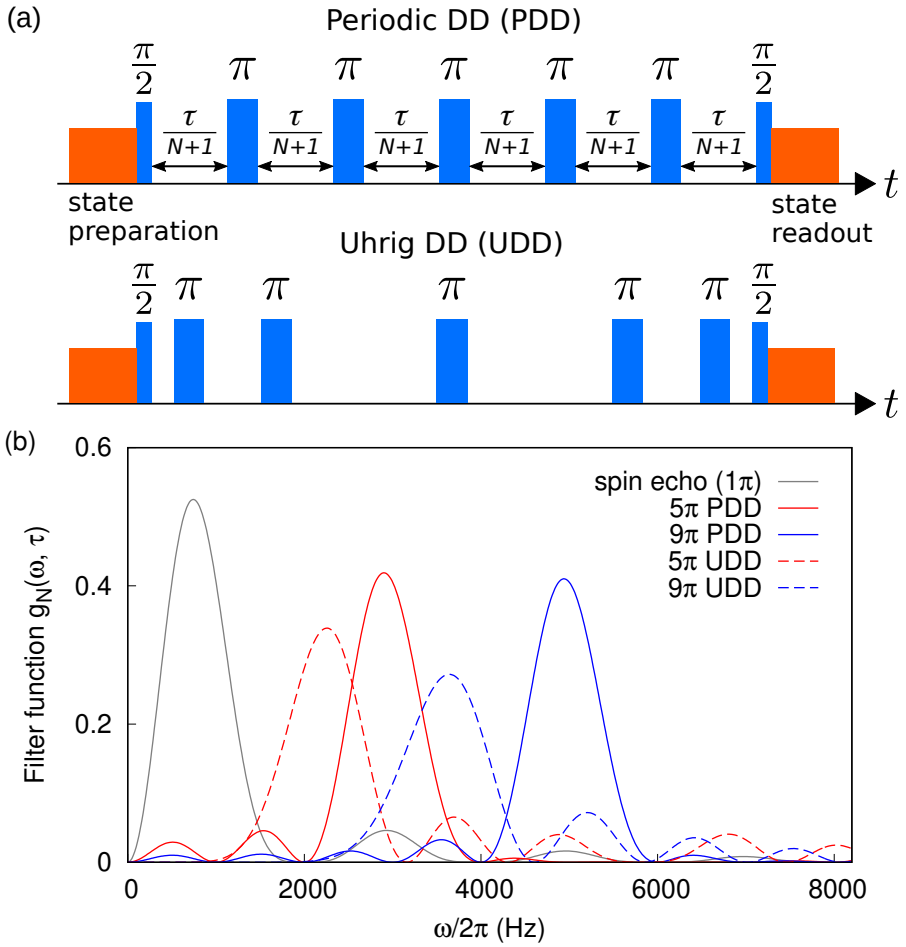

Figure 3.2: (a): Schematic representation of Periodic and Uhrig DD sequences. The qubit state is initialized in the $|\uparrow\rangle$ state. We then bring the qubit state to the superposition state $(|\uparrow\rangle + i\,|\downarrow\rangle)/\sqrt{2}$ with a $\pi/2$-pulse and let it evolve freely for a period τ, with τ being partitioned into small windows using π-pulses. PDD partitions τ into uniform periods. While UDD has its j-th π-pulse locating at $\delta_j\tau$ with $\delta_j = \sin^2[\pi j/(2N+2)]$. (b): Filter function $g_N(\omega, \tau)$ for different pulse sequences with $\tau = 1\,\text{ms}$. Increasing the number N of π-pulses shifts the peak to higher frequencies.

3.2 Experimental realization

In this section, we will describe the experimental setup and sequences that are important in investigating the effect of the DD sequence on preserving the coherence of our system. The complete experimental setup and the relevant atomic transitions are shown in Fig. 3.3.

The atom preparation is similar to the sequence described in Section 2.5.1 where a

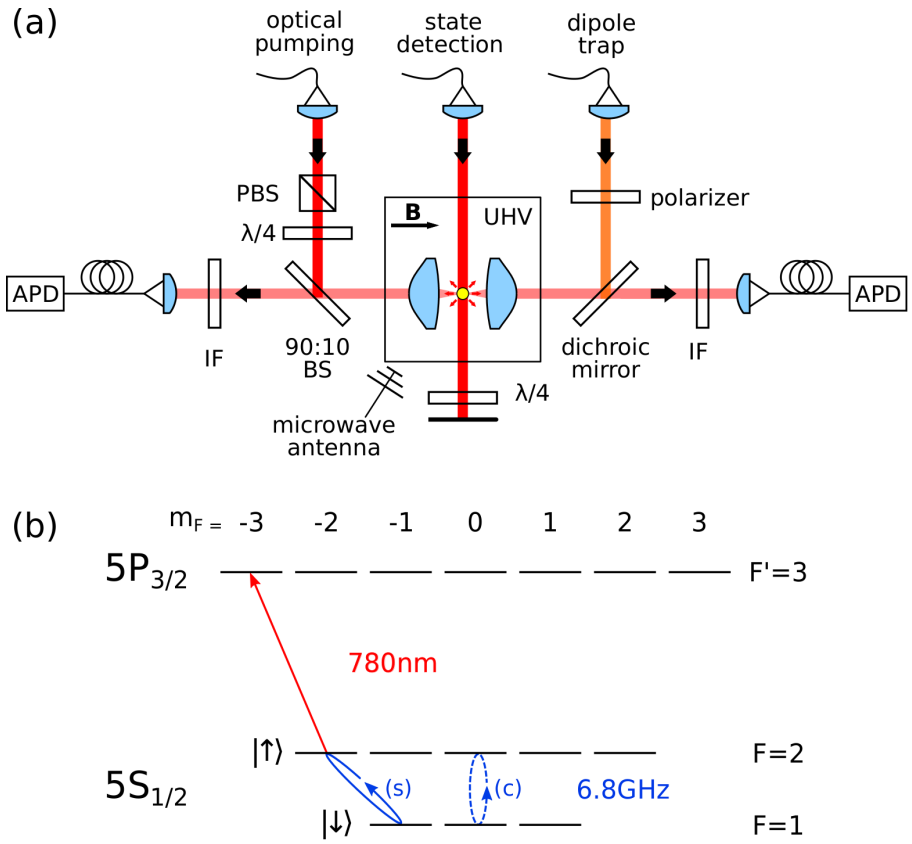

Figure 3.3: (a): Setup for implementing dynamical decoupling sequence on a single atom qubit. APD: avalanche photodetectors, UHV: ultra-high vacuum chamber, IF: interference filter centered at 780 nm, $\lambda/2$: half-wave plate, $\lambda/4$: quarter-wave plate, PBS: polarizing beam splitter, BS: beam splitter, B: magnetic field. (b): Energy level scheme. Stretched state (s) $|F = 2,\ m_F = -2\rangle \equiv |\uparrow\rangle$, $|F = 1,\ m_F = -1\rangle \equiv |\downarrow\rangle$ and clock state (c) $|F = 2,\ m_F = 0\rangle$, $|F = 1,\ m_F = 0\rangle$ are used as the qubit states. The $|\uparrow\rangle$ state can be coupled to $5P^2_{3/2}\,|F = 3,\ m_F = -3\rangle$ via a closed optical transition.

single ^{87}Rb atom is trapped in the FORT and we apply 10 ms of polarization gradient cooling to cool the atom down to a temperature of 14.7(2) μK. Then, a bias magnetic field is applied to lift the degeneracy in the Zeeman states, such that the atom can be optically pumped into the target state. In this chapter, we use the two magnetic-sensitive $5^2S_{1/2}$ Zeeman levels, $|F = 2,\ m_F = -2\rangle \equiv |\uparrow\rangle$ and $|F = 1,\ m_F = -1\rangle \equiv |\downarrow\rangle$ as qubit states, motivated by the possibility to couple $|F = 2,\ m_F = -2\rangle$ to $5^2P_{3/2}$ the excited state $|F' = 3,\ m'_F = -3\rangle$ via a closed optical transition, opening a possible path to protocols originally developed for solid-state quantum systems to be implemented in an atomic system. This includes schemes for the generation of

time-bin atom-photon entanglement [1] and the sequential generation of an entangled photonic string [2, 3], which are crucial resources for quantum computations.

Atoms in the $|\uparrow\rangle$ state are coupled to $|\downarrow\rangle$ by applying a microwave field resonant to this transition using a pair of log-periodic antennae. We then use this field to drive Rabi oscillations and perform various dynamical decoupling sequences to characterize the atomic coherence [27, 65–68]. After that, we need to check in which state the atom is in by utilizing a lossless state-selective detection method described in Section 2.5.2.

After performing the state detection, we will check if the atom is still present in the trap to decide if we will continue the experiment sequence from the cooling stage, or if we need to load a new atom into the trap. For each data point, we repeat this sequence over many experimental cycles until we gather sufficient data to infer the atomic state.

3.2.1 Microwave Generation and Characterization

To drive the magnetic dipole transition between the two hyperfine ground states, $5^2S_{1/2}, F = 2$ and $5^2S_{1/2}, F = 1$, we need to generate a microwave field with a frequency equal to the hyperfine splitting, which in our case is around 6.8 GHz for ^{87}Rb atom. We send the RF signal into a pair of log-periodic antennae (Kent Electronics WA5VJB PCB Log-Periodic 2-11 GHz) that are pointing towards the trapped single atom.

For an atom that is initially in the $|\uparrow\rangle$ state, the probability of it being in the $|\downarrow\rangle$ state after a microwave pulse of duration t is given by

$$P_{\downarrow} = \frac{\Omega^2}{\Omega^2 + \Delta^2} \sin^2\left(\frac{\sqrt{\Omega^2 + \Delta^2}\, t}{2}\right), \tag{3.8}$$

where Ω is the Rabi frequency and $\Delta = \omega - \omega_0$ is the detuning of the microwave field from the resonant frequency. With appropriate choice of Ω and t, the highest chance of the atom being in the $|\downarrow\rangle$ state is located at the frequency where $\Delta = 0$ according to Eqn. 3.8.

As such, to locate the resonant frequency ω_0 of the transition experimentally, we prepare the atom into the $|\uparrow\rangle$ state and turn on the microwave field for 5 μs. After that, we turn on the state detection light and the atomic state can be inferred

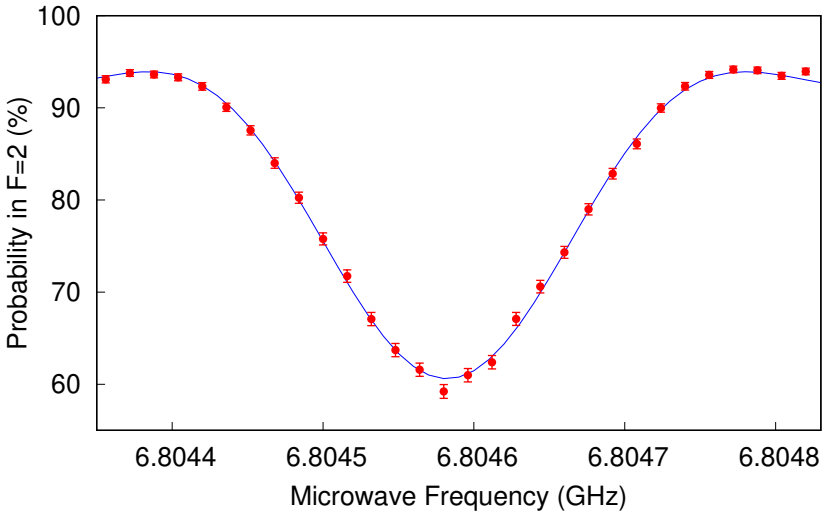

Figure 3.4: Spectroscopy measurement to locate the resonance of $|\uparrow\rangle \leftrightarrow |\downarrow\rangle$ transition. We send a microwave pulse of 5 μs to excite the atom and measure the state of the atom. The blue solid line is a fit to 1-$P_{\downarrow}$ while also taking into account the imperfection in preparing the qubit in $|\uparrow\rangle$ state. A resonant frequency of 6.804582 GHz can be extracted from the fit.

from the amount of photons scattered by the atom. We repeat the measurement at different microwave frequencies, but keep the RF power and pulse duration constant. The result is shown in Fig. 3.4. We can extract the resonant frequency from the fit to 1-$P_{\downarrow}$. With this, we can tune the frequency of the microwave field to match the resonant frequency of the targeted transition.

3.2.2 Rabi Oscillation

Now with the resonant frequency known, there is yet another key ingredient to implement various dynamical decoupling sequences: the pulse area. For example, the π-pulse mentioned in the previous section is an excitation pulse with a pulse area of π. The pulse area can be obtained from the product of Rabi frequency, Ω, and the pulse duration. To understand the influence of pulse area, we can look at Eqn. 3.8 in the case of zero detuning. For a π-pulse ($\Omega t_{\pi} = \pi$), the atom that is initially in the $|\uparrow\rangle$ state will end up in the $|\downarrow\rangle$ state. While for a $\pi/2$-pulse ($\Omega t_{\pi/2} = \pi/2$), the atom will be in a superposition of the $|\uparrow\rangle$ and $|\downarrow\rangle$ states. In the Bloch sphere picture, the application of a π-pulse or a $\pi/2$-pulse corresponds to a rotation of π or $\pi/2$ along any axis on the equatorial plane that is defined by the pulse itself.

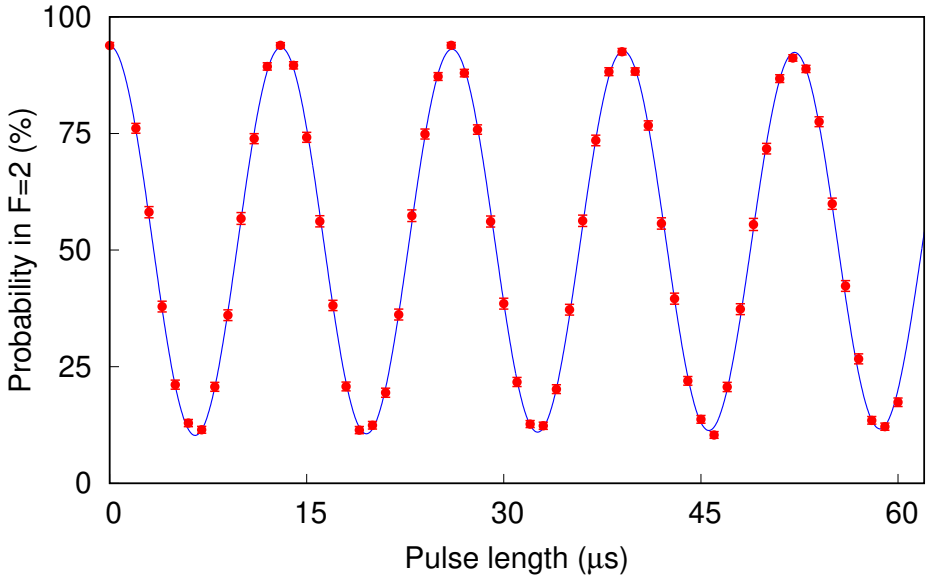

Figure 3.5: Rabi oscillation between $|\uparrow\rangle$ and $|\downarrow\rangle$ states. The state detection measurement determines if the atom is in which hyperfine level of the $5^2S_{1/2}$ manifold. The solid line is a fit to an exponentially decaying cosine function to extract the Rabi frequency, $\Omega_{mw} = 2\pi \times 76.78(3)\,\mathrm{kHz}$.

Since the pulse area is given by Ωt, we need to measure the Rabi frequency of our microwave driving field to infer the pulse duration needed for a π pulse. In order to do that, we use the microwave field to drive Rabi oscillations between the $|\uparrow\rangle$ and $|\downarrow\rangle$ states. We measure the atomic state after turning on the microwave field for a different durations. The result is shown in Fig. 3.5.

The Rabi oscillation in Fig. 3.5 exhibits a Rabi frequency of $\Omega_{mw} = 2\pi \times 76.78(3)\,\mathrm{kHz}$ with a visibility of 0.837(7). By assuming perfect state preparation and no other source of error, a maximum visibility V_{max} of 0.948(4) can be achieved as the maximum visibility is related to state detection fidelity through $V_{max} = 1 - 2(1 - F)$. The Rabi oscillation shows little decay within the first $60\,\mu$s, implying that the reduced visibility is most likely due to imperfections in the state preparation process rather than the driving process. As shown in Fig. 3.5, the probability of the atom in $5^2S_{1/2}, F = 2$ level does not go near to zero, implying that there is a non-zero probability that the atom is in other Zeeman states that do not couple to the microwave field. The reduced visibility of the Rabi oscillation could be explained by the occupation of other states due to imperfect state preparation. From the

detection fidelity, the population of the atom prepared in $|\uparrow\rangle$ state is inferred to be 88.9(9) %.

With the measured Rabi frequency, we can infer the pulse duration required for a π-pulse is 6.51 μs. Since the precision of the pulse is bounded by the smallest step size of the pattern generator which is 10 ns, it affects the pulse area of the π-pulse by less than 0.15 % and is negligible for most situations. We also calibrate the Rabi frequency regularly to eliminate the drift due to RF power drift and the mechanical movement of the antennae.

3.2.3 Coherence Characterization

To determine the dephasing time of our qubit system, we first carry out a Ramsey experiment where we apply two $\pi/2$-pulses with a free evolution time τ in between the two pulses to the atoms in the $|\uparrow\rangle$ state. We repeat the experiment for different τ and fit an exponential decay to the Ramsey contrast, which results in dephasing time $T_2^* = 38(3)\,\mu$s (Fig. 3.6, red). This dephasing time serves as a baseline for us to quantify the effect of various DD sequences in terms of protecting the coherence of the system.

Next, we apply standard spin echo sequence [58, 59], which add an extra π-pulse in the middle of the free evolution window τ as compared to the Ramsey experiment. As mentioned in the previous section, this sequence helps to refocus the atomic state and reverse the inhomogeneous dephasing during the free evolution time, resulting in a much slower decay of the Ramsey contrast. With this sequence, we obtain a coherence time $T_2 = 480(21)\,\mu$s for the stretched state of our qubit by fitting the data to a decaying Gaussian (Fig. 3.6, blue). Here, the coherence time is defined as the $1/e$ decay time of the spin-echo visibility.

Instead of characterizing the coherence of the magnetically sensitive Zeeman states, researchers usually focus on the magnetically insensitive Zeeman states because these states are immune to noise from fluctuating magnetic fields. In order to compare the coherence in this qubit with other systems [66, 69, 70], we perform a spin echo on the transition between magnetically insensitive Zeeman states, $5S_{1/2}$, $|F = 1,\ m_F = 0\rangle \leftrightarrow |F = 2,\ m_F = 0\rangle$ of our qubits as most of the other experiments were also probing the clock state coherence. Using the same procedure, we find

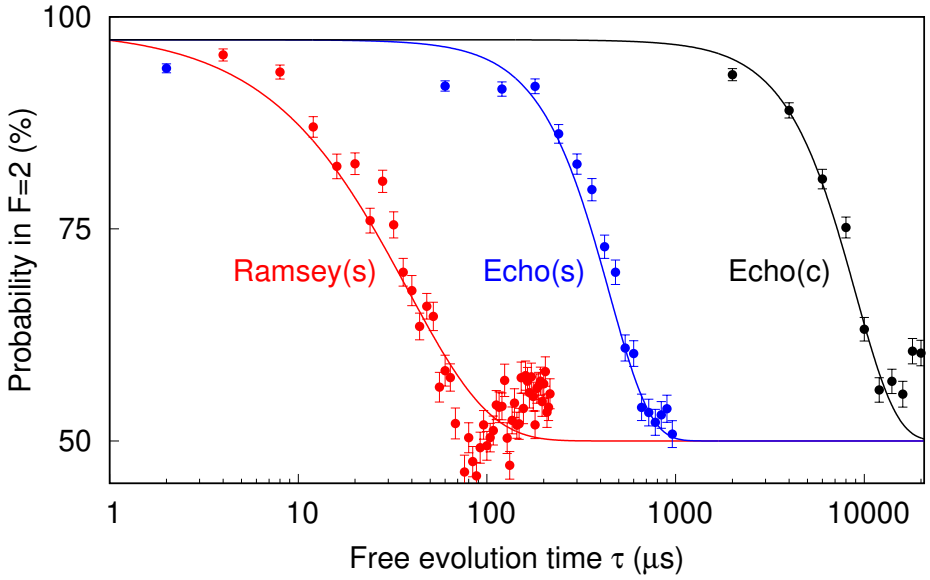

Figure 3.6: Ramsey and spin-echo when the atom is initially prepared in $|\uparrow\rangle$ (s) or $|F = 2,\ m_F = 0\rangle$ (c). We fit a decaying exponential to the Ramsey signal and a decaying Gaussian to the spin-echo signal to extract their respective $1/e$ time constants; $T^*_{2,s} = 38(3)\,\mu$s, $T_{2,s} = 480(21)\,\mu$s, and $T_{2,c} = 9.5(6)$ ms.

the coherence time of the magnetically insensitive qubit to be $T_{2,c} = 9.5(6)$ ms, which is 20 times longer compared to the stretched state coherence (Fig. 3.6, black). This observation is consistent with previous experiments with the superposition of magnetically insensitive Zeeman states in a red detuned dipole trap, which has a typical coherence time of 10 ms. It has been shown that the coherence time can be improved to tens of milliseconds by reducing the trap depth [66, 70]. The coherence time on the order of hundreds of milliseconds has also been demonstrated by reducing the differential light shift with a magic-intensity trapping technique [71].

We look into different aspects that could be the dominant factor that limits the coherence time of the magnetically sensitive states. Initially, we suspect that the fluctuations in dipole beam intensity give rise to the differential light shift that limits our coherence time in the magnetically sensitive states. To confirm our hypothesis, the coherence time for magnetically sensitive states is calculated analytically following [66]. For the inhomogeneous dephasing caused by an atom temperature-dependent differential light shift, we expect a dephasing time of around 1.4 ms from the relation $T_2^* = 0.97(2U_0)/(\delta k_B T_{atom})$ [66]. In our setup, the trap

depth is $U_0 = k_B \times 0.88\,\mathrm{mK}$ with a maximum differential light shift $\delta \simeq 2\pi \times 13\,\mathrm{kHz}$ for our 851-nm FORT. An irreversible dephasing dominated by intensity fluctuations of the dipole laser gives $T_2 = 1/(\delta\sigma_A) \simeq 20\,\mathrm{ms}$ with the measured Allan deviation $\sigma_A = 0.06\,\%$ of dipole power, following the definition in [66]. As such, we conclude that the coherence time for magnetically sensitive states is not limited by our dipole trap.

For ^{87}Rb, the stretched state ($5S_{1/2}$, $|F = 1,\ m_F = -1\rangle \leftrightarrow |F = 2,\ m_F = -2\rangle$) qubit's sensitivity to the external magnetic field is 21 GHz/T at low fields. Due to the high magnetic sensitivity of the qubit states, fluctuations in magnetic fields can be the dominant factor in the dephasing mechanism. Therefore, we can find ways to isolate the magnetic noise in order to achieve a longer coherence time for our qubit. Despite not using the clock states, we manage to achieve a high ratio of state manipulation speed and preserved coherence, $T_{2,s}/t_\pi \approx 74$ which is sufficient for most applications.

3.3 Periodic DD sequence

In the previous section, we showed that the spin-echo technique, as the simplest example of a DD sequence with one single π-pulse, can already improve the coherence time. To test the effect of DD sequences with more π-pulses, we first apply the periodic DD (PDD) sequence to our system. PDD sequence is the simplest pulsed DD scheme with all the π-pulses distributed evenly in the free evolution time window. Using the same experimental procedure, the coherence evolution of the qubit system under the PDD sequence is shown in Fig. 3.7.

Initially, we expect a monotonic decaying profile for the coherence evolution that is similar to the spin-echo sequence result shown in Fig. 3.6. However, we observe that the decaying envelopes contain collapses which always occur at the same partition period $\tau/(N+1)$ for various N from Fig. 3.7. The partition period here refers to the free evolution time window between each π-pulse. For the three sets of data, the first dip always occurs at around $\tau_{dip}/(N+1) = 40\,\mu\mathrm{s}$ while the second one appears at $\tau_{dip}/(N+1) = 130\,\mu\mathrm{s}$. This feature can be explained by the atomic motion in the dipole trap as the dips occur at frequencies that correspond to the trap frequency. A similar effect has also been observed in previous studies [72,

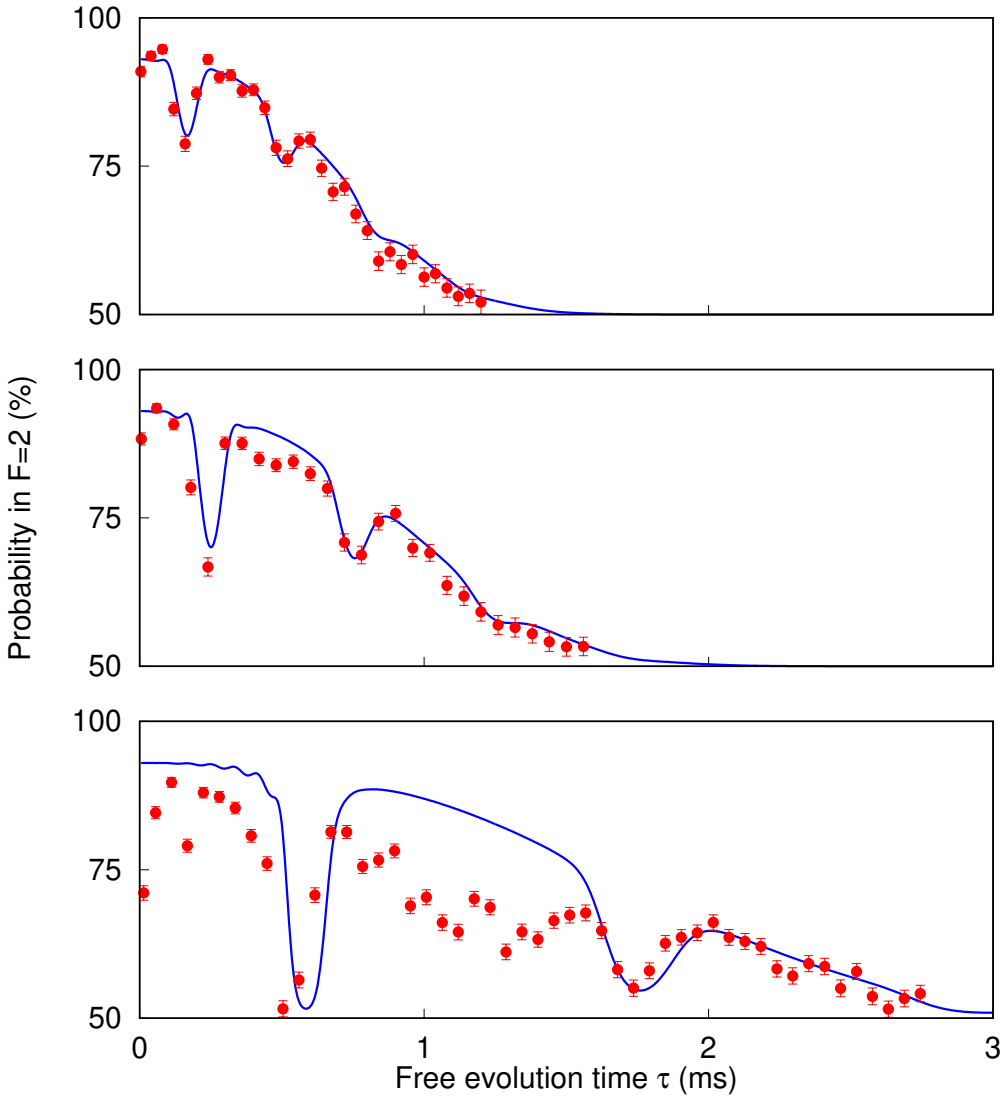

Figure 3.7: Coherence evolution of the stretched state qubit under Periodic DD (PDD) for a different number of π-pulses. N is chosen to be $N = 3$ (top), $N = 5$ (middle), and $N = 13$ (bottom) π-pulses. Solid lines are numerical simulations using our heuristic noise model. Error bars represent the standard error of binomial statistics accumulated from 300 repeated sequences.

73] and we will discuss this further in the next section.

Due to the recurring dips, the qubit coherence evolution under PDD does not fit well with a smooth decaying Gaussian. As such, the coherence time extracted from the fit is not very meaningful in this context. To compare various decaying envelopes, we define the coherence time T_2 as the time for the state coherence to decay by a factor of $1/e$. This is consistent with the usual definition in a bare two-level system.

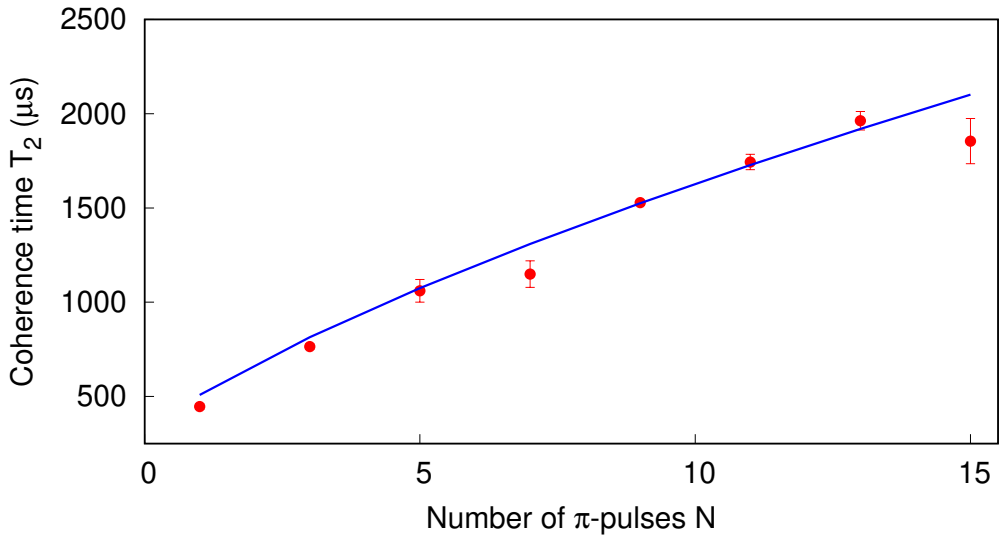

Figure 3.8: Coherence time T_2 as a function of the number N of π-pulses. The solid line shows the simulation result for a spectrum $S(\omega) \propto 1/\omega^{\alpha}$ with $\alpha = 1.73$.

Of course, we also take into account the fact that the qubit is not perfectly prepared in the desired initial state. Using this definition, Fig. 3.8 shows the coherence time as a function of the number of π-pulses.

As mentioned in Section 3.1.2, the DD sequence can be treated as a noise filter function where the function's peak frequency shifts higher as N increases for a fixed free evolution time τ. From the result in Fig. 3.8, the coherence time increases with the number N of π-pulses in a sequence. This suggests that the noise follows a $1/\omega^{\alpha}$ spectrum with $\alpha > 0$. Besides, the dependence of T_2 on N suggests that T_2 can potentially be further improved by using additional refocusing pulses. A similar trend has been observed in other qubit systems, including single silicon-vacancy centers [74], single nitrogen-vacancy centers [75], and single $^{43}Ca^{+}$ ion system [76].

In our system, we are currently limited to pulse sequences with $N \leq 20$ as the contrast of the coherence evolution drops as N increases. From Fig. 3.7, we can see that the probability of atom in F=2 state can reach 95% at very short τ for 3 π-pulses PDD (top). This probability drops to 90% when N increases to 13 (bottom). This limitation is mainly due to pulse imperfections including errors in the flip angles and finite pulse width introducing dephasing to the qubit, as discussed in [77]. We attribute the main source of pulse imperfections in our system to the inexact π-pulse

timing. By driving the qubit continuously with various numbers N of π-pulses, we estimate the uncertainty of the π-pulse timing to be 1 % from the Rabi contrast. This small deviation from the exact π rotation in the Bloch sphere gives a cumulative error in the multipulse DD sequences when the number of π-pulses becomes too large. Of course, more robust pulse sequences with pulse phases that are shifted appropriately can be applied to mitigate pulse errors. Nonetheless, this preliminary refocusing strategy here has offered us an insight into the dephasing mechanism of a magnetic-sensitive qubit state.

To further confirm that the occurrence of the dips is due to the atomic motion in the dipole trap, we simulate $\chi(\tau)$ under a simple noise model consisting of a $1/\omega^{\alpha}$ noise and a Gaussian centered at the axial trap frequency $\omega_0 = 2\pi \times 12.0\,\mathrm{kHz}$. The noise spectral density is given by

$$S(\omega) = S_0/\omega^{\alpha} + S_1 e^{-(\omega-\omega_0)^2/(2\sigma^2)}. \tag{3.9}$$

In this noise model, the $1/\omega^{\alpha}$ spectrum represents the noise floor produced by ambient magnetic field fluctuations and power fluctuations of the dipole light field, while the Gaussian spectrum represents the differential light shift experienced by the atom when it moves in an inhomogenous dipole light field.

Since we extract the coherence time in Fig. 3.8 by ignoring the recurring dips, it is an ideal set of data for us to estimate the value of S_0 and α. Using only the first term in Eqn. 3.9, the simulation manages to produce a solid line that matches well with the experimental data for a $1/\omega^{\alpha}$ noise with α=1.73. Next, we calculate the coherence evolution for different numbers N of π-pulses using the full model including the second term in Eqn. 3.9. As shown in Fig. 3.7, our heuristic noise model is able to predict the recurring features quite well.

3.3.1 Noise Spectroscopy

In the field of magnetometry, dynamical decoupling is also implemented in order to reconstruct the spectrum of the noises that are coupled to the system [78, 79]. We manipulate the band-pass filter properties of $g_N(\omega, \tau)$ function to characterize the noise spectrum [80, 81]. Knowing that the filter function behaves as periodic sinc-shaped peaks at frequency $\omega_l \simeq (2l+1)\omega$ with $\omega \simeq N\pi/\tau$, we probe the noise spectral density by varying N and τ.

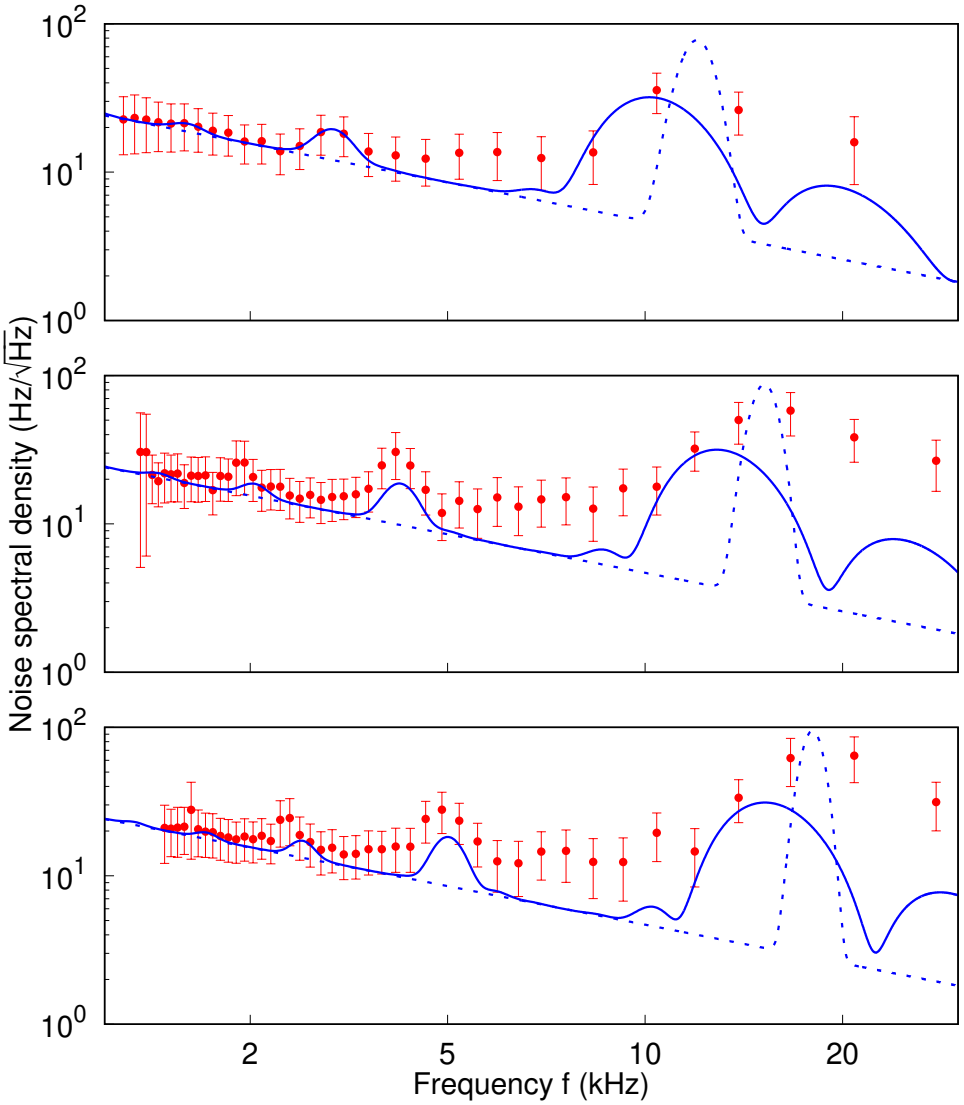

Figure 3.9: Noise spectroscopy with DD adapted from atomic magnetometry. Red circle: noise spectral density reconstructed with experimental data. The recurring peaks are the feature of the filter function $g_N(\omega)$. Blue dashed line: noise spectrum of our heuristic noise model. Blue solid line: reconstructed noise spectral density in simulation. This is obtained by modulating the exact noise spectrum (blue dashed line) with the filter function of the chosen DD sequence. Trap depth is set to be 0.88 mK (top), 1.04 mK (middle), and 1.41 mK (bottom), respectively. The trap frequencies used in the simulation are 12.0 kHz, 15.2 kHz, and 18.0 kHz, respectively.

Fig. 3.9 shows the noise spectra probed experimentally when the dipole beam power is being varied. This measurement will give us more information about the atomic motion in different trap depths as the trap depth is proportional to the dipole laser power. The reconstruction of noise spectral density $S(\omega)$ follows [80,

81]. The frequency range is determined by the choice of free evolution time τ. We observe the maximum noise density around 10.4 kHz, 16.7 kHz, and 20.8 kHz for dipole trap with trap depth of 0.88 mK, 1.04 mK, and 1.41 mK, respectively. As the dipole beam power increases, the maximum noise density shifts to higher frequencies as expected. The noise peaking at the axial trap frequency can be explained by the polarization gradients of a tightly focused FORT following [82]. Despite the fact that we use a linearly polarized FORT for which the vector shift vanishes, the tight focusing of FORT can still result in a spatially varying vector light shift for the qubit states around the focal plane. As the trap frequency along axial direction $\omega_z = \sqrt{2U_0/(mz_R^2)}$ increases along with the trap depth U_0, the light shift noise due to oscillatory atomic motion shifts to higher frequencies. This is also in line with the observation in Fig. 3.9.

Compared to our heuristic noise model, we observe some recurring peaks in the noise spectra at lower frequencies. After careful inspection, we figure out that these peaks are the feature of the filter function $g_N(\omega)$, determined by the DD sequence. We numerically construct the noise spectral density modulated by the filter function with our heuristic noise model and find that the simulation predicts the recurring features well. By utilizing the higher harmonics of the filter function, the trap frequency can be resolved with higher precision. We can use this as a basis for the precision measurement of trap parameters.

Another observation is that the width of the Gaussian noise in our model is much narrower than the noise spectral density modulated with a filter function. This is because of the fact that the bandwidth of the filter function is inversely proportional to N. In our experiment, the number of refocusing pulses N used is less than 20, resulting in a bandwidth that is comparable to the width of the Gaussian noise which we would like to resolve. Indeed, it is possible to improve the resolution of the noise spectral density by increasing the number of π-pulses N but there is a trade-off for increasing noise due to accumulated pulse errors.

Aside from the peak features, we notice that the background noise floor does not vary with dipole beam power. We measure the intensity fluctuation of the dipole beam and find that it only corresponds to noise spectral density of $0.5\,\mathrm{Hz}/\sqrt{\mathrm{Hz}}$. This suggests that the background could be mainly due to stray magnetic field fluctuation.

3.4 Uhrig DD sequence

To compare the effectiveness of different DD sequences on preserving the qubit coherence, we also apply UDD protocols [60] to suppress dephasing in our qubit system. It also has been shown analytically that the UDD sequence could provide strong suppression of phase accumulation when the noise environment contains a high-frequency component and a sharp high-frequency cutoff. The pulse sequence and the filter function $g_N(\omega, \tau)$ for UDD are shown in Fig. 3.2. A feature of UDD is the lack of higher harmonics but more sidelobes in its filter function. With the same number of π-pulses N, UDD produces a pass band with a larger width peaking at a lower frequency compared to the PDD sequence. This implies that the UDD sequence might perform worse under a broadband noise spectrum.

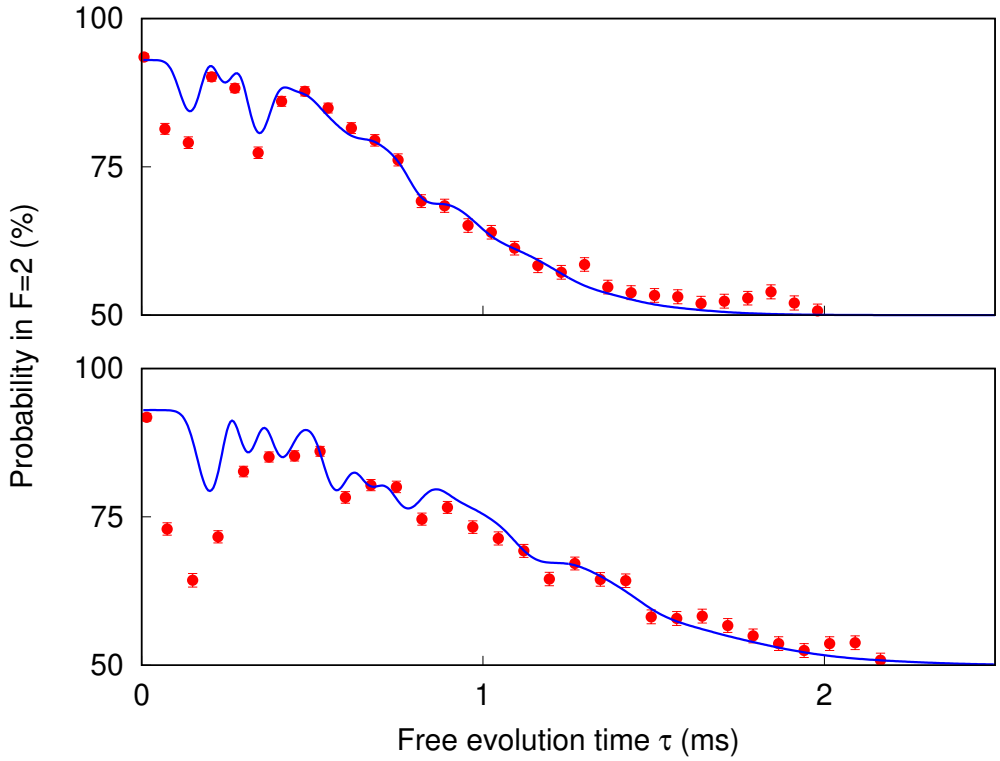

Figure 3.10: Implementing Uhrig dynamic decoupling (UDD). Top: UDD with 3 π-pulses, $T_2 = 926(16)\,\mu$s. Bottom: UDD with 5 π-pulses, $T_2 = 1285(25)\,\mu$s. Solid lines are numerical simulations using our heuristic noise model with the same parameters implemented in Section 3.3. Error bars represent standard error of binomial statistics accumulated from 300 repeated sequences

By applying the UDD sequence with the same procedure, the coherence evolution

of a single atom qubit is shown in Fig. 3.10. Again, the simulation with our heuristic noise model can reproduce the wiggles qualitatively in the $|\uparrow\rangle$ population as a function of the total free evolution time τ. However, the simulation falls short in predicting the magnitude of the wiggles. This mismatch between the simulation and the result might be due to the assumption of instantaneous π-pulse in calculating the filter function $g_N(\omega, \tau)$.

To avoid any complications caused by the wiggles, we opt for the same definition of the coherence time as in the previous section where the state coherence decays by a factor of $1/e$. We observe a coherence time of $926(16)\,\mu$s and $1285(25)\,\mu$s for $N = 3$ and $N = 5$ π-pulses, respectively. Compared with the coherence time obtained using PDD sequence with the same number of π-pulses ($764(14)\,\mu$s for $N = 3$ and $1060(60)\,\mu$s for N=5), we observe an improvement of 21.2 % on the coherence time, consistent for both $N = 3$ and $N = 5$. In our system, the performance of both PDD and UDD sequences are comparable to each other because in general, a DD sequence requires a rather distinctive noise spectrum to outperform its counterpart.

3.5 DD benchmarking

Theoretically speaking we can try to work out the sequence that fits our system the most given that we have information about the noise spectrum. For practical purposes, it might be easier to experimentally figure out the best sequence for a particular system with limited knowledge about the associated noise. For most applications in quantum information processing, we aim to preserve coherence maximally for a given duration. In the following section, we will demonstrate an optimization protocol to determine the sequence that works best for our qubit.

As shown in Fig. 3.11 (a), we are using a sequence with 5 π-pulses. We set a fixed free evolution time τ to mimic the situation where the coherence need to be maintained for a certain duration in between qubit operations. In this characterization, we choose a fixed free evolution time of $\tau = 900\,\mu$s and $\tau = 1500\,\mu$s. Now, the optimization is still too complicated to realize experimentally due to the 5 degrees of freedom arising from the π-pulse locations within the free evolution time window. So we impose a reflection symmetry to the pulse sequence such that it will symmetry with respect to the middle π-pulse. With these two constraints, we

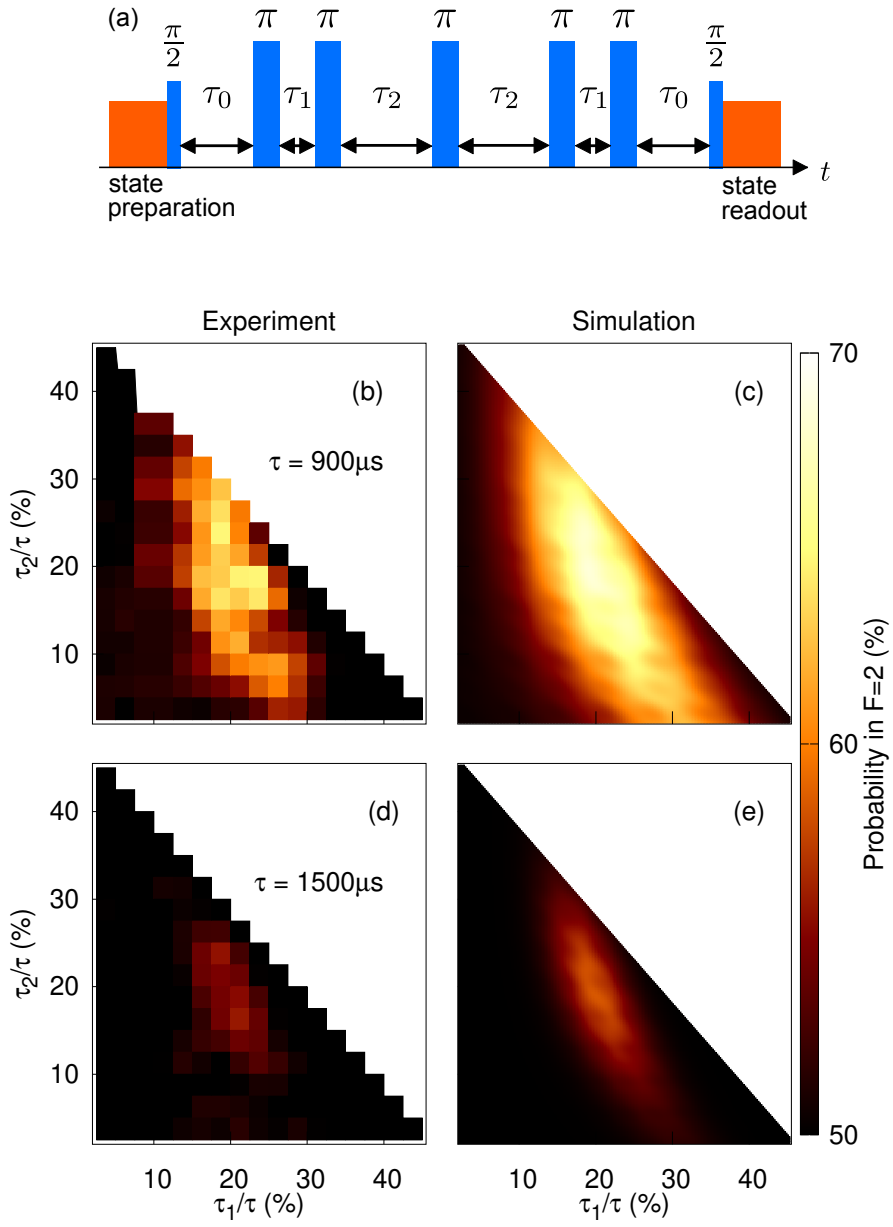

Figure 3.11: Optimization with five π-pulses for a fixed free evolution time $\tau = 900\,\mu$s and $\tau = 1500\,\mu$s. (a): Schematic representation of the DD sequence, satisfying $\tau_0 + \tau_1 + \tau_2 = 0.5\tau$. (b-d): Population of $F = 2$ state at the end of refocusing. For both $\tau = 900\,\mu$s and $\tau = 1500\,\mu$s, the maximum fidelity is not given by standard DD sequences such as UDD (τ_1/τ =18.3 %, τ_2/τ =25.0 %) or PDD (τ_1/τ =16.7 %, τ_2/τ =16.7 %), the maximal point locates at τ_1/τ =19.2 %, τ_2/τ =19.6 % in the simulation.

successfully reduce the number of free parameters from 6 to 2.

To better understand the effect of the noise on the qubit coherence, we numerically calculate the dynamics of the qubit state using our heuristic noise model introduced in previous sections, following Eqn. 3.5. From Fig. 3.11, we find a good agreement between the observed coherence and the model for the same parameters used in the previous section. The maximum coherence is obtained with the protocol that follows $(\frac{\tau_0}{\tau}, \frac{\tau_1}{\tau}, \frac{\tau_2}{\tau}) = (11.2\,\%, 19.2\,\%, 19.6\,\%)$. This optimal sequence matches well with the Carr-Purcell (CP) sequence, which is widely used in the field of NMR and is constructed with the first and last precession periods being half of the duration of the interpulse period, e.g. $(\frac{\tau_0}{\tau}, \frac{\tau_1}{\tau}, \frac{\tau_2}{\tau}) = (10\,\%, 20\,\%, 20\,\%)$ [83].

3.6 Carr-Purcell-Meiboom-Gill sequence

Inspired by the results obtained from the optimization in the previous section, we probe the coherence time T_2 of our system with the CP sequence. As shown in Fig. 3.12, we observe a coherence time of 1017(38) μs and 1274(42) μs for $N = 3$ and $N = 5$ π-pulses, respectively. In terms of coherence time, there is an improvement of 33.1 %, and 20.2 % for $N = 3$ and $N = 5$ π-pulses respectively compared to the case of using the PDD protocol. However, the improvement in coherence time halts at larger N. Especially, the coherence time decreases after $N \geq 15$, due to the drop in initial signal contrast caused by the accumulation of pulse imperfections.

To address this problem, we apply the Carr-Purcell-Meiboom-Gill (CPMG) sequence to our qubit system, which has been demonstrated to be able to mitigate pulse imperfections for the preservation of a quantum state [57]. In terms of pulse location, the CPMG scheme is the same as the CP scheme. The only difference is that the refocusing microwave pulse is 90° phase shifted from the $\pi/2$-pulse which prepares the superposition state. For example, we start with the $|\uparrow\rangle$ state in the Bloch sphere and then apply a $\pi/2$ rotation about the x-axis to it. Now, the state will lie along the y-axis. For the CP sequence, the subsequent π-pulses will rotate the state about the x-axis. In contrast, in the CPMG scheme, the 90° phase shift means that the subsequent π-pulses will rotate the state about the y-axis. In the ideal case where the state experiences no dephasing, it will stay on the y-axis, and the rotation about the y-axis will not change the state. At the end of this sequence,

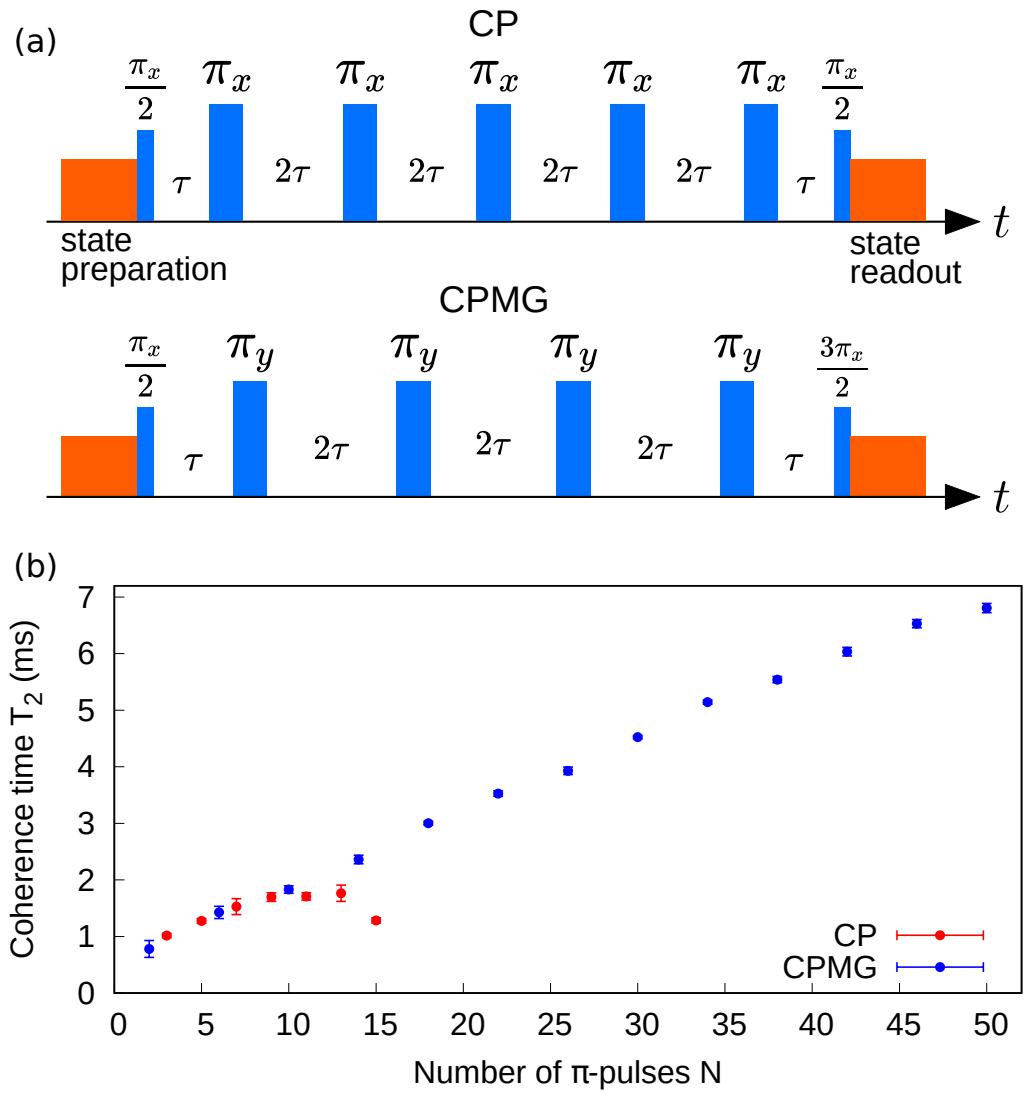

Figure 3.12: (a): Schematic representation of the CP and CPMG sequence. In both sequences, the qubit state is initialized in the $|\uparrow\rangle$ state and then is brought to the superposition state $(|\uparrow\rangle + i\,|\downarrow\rangle)/\sqrt{2}$ with a $\pi/2$-pulse. In CP, we apply an odd number of π-pulses that have the same phase as the $\pi/2$-pulse, denoted as π_x. While in CPMG, we apply an even number of π-pulses that have orthogonal phase as the $\pi/2$-pulse, denoted as π_y. Afterward, the atom is brought back to its initial state by $\pi/2$-pulse and $3\pi/2$-pulse in CP and CPMG sequences respectively. (b): Coherence time T_2 as a function of the number N of π-pulses for CP and CPMG sequence.

we would need a $3\pi/2$-pulses about the x-axis to bring the state back to the $|\uparrow\rangle$ state.

In Fig. 3.12(b), we compare the coherence time of our qubit under the CPMG protocol to the CP protocol. For a small number of π-pulses, the performance of

the CPMG protocol is identical to the performance of the CP protocol since the accumulation of pulse error is negligible at this stage. In contrast to the CP sequence, the CPMG sequence that contains up to $N = 50$ π-pulses can be applied to our qubit with reasonably high signal contrast in the coherence evolution. We achieve a coherence time of 6.81(8) ms, which is 3.7 times longer than the optimal coherence time obtained with the PDD protocol. We have also applied other variants of the CPMG protocol, such as the XY schemes [84], and we observe similar coherence performance.

Throughout this chapter, we are investigating the coherence of one single state possessing a particular phase. For an arbitrary state on the Bloch sphere, other robust sequences are more effective in protecting the qubit coherence such as KDD_x and KDD_{xy} [77, 85]. Concatenated DD sequences in which phases are changed recursively are some other alternatives for preserving arbitrary spin states [86, 87].

3.7 Conclusion

We have presented a detailed experimental study of the implementation of dynamical decoupling in a single neutral atom qubit system. Along the process of characterizing and comparing the performance of various standard DD protocols including periodic DD, Uhrig DD, CP DD, and CPMG DD, we observe an enhancement in the coherence time T_2 by two orders of magnitude from the Ramsey decay time T_2^*. The observed coherence time of 6.8 ms is sufficient to facilitate the high-fidelity transfer of quantum states between quantum repeater nodes separated by thousands of kilometers [88]. By treating the DD sequence as a noise filter, we characterized the noise spectrum of an optically trapped Rubidium atom. Through the optimization protocol in Section 3.5, we determined the best sequence in terms of coherence preserving for our qubit system. In the last part of this chapter, we demonstrated that the CPMG sequence performs the best in the longer timescale.

Future experiments will explore lowering the noise floor and motion-dependent dephasing. Improvements will extend the coherence times and hence open up new possibilities for the implementation of more robust free-space neutral atom quantum memories for future quantum repeater networks [89]. A better understanding of the qubit response to noise may also help to develop a broadband single-atom sensor

that would allow imaging magnetic fields with a spatial resolution at atomic length scales.

Chapter 4

Mollow triplet from a single atom

This chapter presents the investigation of the atomic fluorescence emitted by a single optically trapped atom. This includes a frequency spectrum measurement of the fluorescence and correlation between photons originating from different parts of the spectrum. We start with a brief theoretical description of the fluorescence emitted by a two-level system under different driving strengths. Next, we investigate the frequency spectrum of the resonance fluorescence using a Fabry-Perot cavity. By utilizing the closed transition of ^{87}Rb, we get to perform the experiment under conditions that are coming close to the ideal condition considered in the Mollow triplet theory. Second-order correlation measurements reveal the single photon nature of the fluorescence concurrently with Rabi oscillations of a strongly excited atom. The subsequent section will focus on the effect of off-resonant excitation on the arrival time of photons originating from different peaks of the triplet spectrum. The asymmetry in correlations between photons from two sidebands of the atomic spectrum under off-resonant excitation indicates that there is a preferred time-ordering of the emitted photons from different sidebands. A majority of the content in this chapter has been published in [90].

4.1 Introduction

The study and investigation of fluorescence emitted from resonantly excited atomic systems have played a major role in understanding the interaction between atoms and radiation [91]. In 1930, Weisskopf first established the theory of atomic resonance fluorescence in the limit of weak excitation [92]. In this limit, the fluorescence spectrum of a two-level atom shows a single scattering peak centered

at the excitation frequency that follows the linewidth of the excitation field. This single peak consists mostly of coherent scattering and had been measured in various systems [93–95], which is a promising way to generate highly coherent single photons with subnatural linewidth [96, 97].

Later this result was extended to include the effect of strong excitation radiation by Mollow in 1969 [98]. When the driving intensity increases above the saturation regime, the incoherent component in the fluorescence dominates, and the single peak spectrum evolves into a triplet structure. The photons emitted in this process continue to be of interest in quantum optics, as these photons exhibit different correlation signatures in particular conditions such as off-resonant excitation [99–105]. There has been renewed interest in the photon statistics of the coherent and incoherent components that coexist in the fluorescence [106–109]. With better filtering techniques that are available nowadays, the photon correlation from these two components can be measured independently.

The Mollow triplet was first observed experimentally in an atomic beam passing perpendicularly through an intense laser field [110–112] where the emitted fluorescence spectrum was analyzed using a Fabry-Perot cavity. This configuration minimized Doppler broadening due to atomic motion and the fluorescence could be approximated as the light emitted from individual non-interacting atoms. Since then, the Mollow triplet has been successfully observed in many different systems such as quantum dots [95, 103, 113–116], molecules [117], ions [118, 119], cold atomic cloud [120], and superconducting qubits [121–123].

While easier to implement experimentally, light interaction with an ensemble of atoms will mask certain features of the process such as photon anti-bunching. In contrast, a single optically trapped atom is an excellent candidate to investigate photon correlations between different frequency components of the Mollow triplet. An optically confined atom can be cooled to sub-Doppler temperature owing to polarization gradient cooling (PGC) [124, 125], and therefore suppresses the Doppler contribution to the spectrum. Using a magnetic field to lift the Zeeman degeneracy and an appropriate driving laser polarization, the closed transition of an ideal two-level system can be implemented, coming close to the ideal situation considered in the Mollow triplet theory.

4.2 Theoretical Background

In this section, we will give a brief overview of the two-level system interacting with a classical field [126]. The characteristic of the fluorescence emitted during this process such as the intensity correlation and the frequency spectrum will also be discussed in the following section.

4.2.1 Two-level system

Let's start with a two-level system that consists of a ground state and an excited state, labeled as $|g\rangle$ and $|e\rangle$. These are the eigenstates of the unperturbed Hamiltonian given by

$$H_0 = \hbar\omega_0(|e\rangle\langle e|), \tag{4.1}$$

where ω_0 is the resonant frequency of the unperturbed system. As such, the system at any time t can be described as a coherent superposition

$$|\psi(t)\rangle = c_g(t)\,|g\rangle + c_e(t)\,|e\rangle\,. \tag{4.2}$$

When we start to consider the two-level system interacting with a classical monochromatic field $\mathbf{E}(t)$ with frequency ω, the total Hamiltonian can be written as

$$H = H_0 + H_I. \tag{4.3}$$

The interaction Hamiltonian, H_I under the dipole approximation is given by

$$H_I = -\mathbf{d}\cdot\mathbf{E}, \tag{4.4}$$

where $\mathbf{d} = -e\mathbf{r}$ is the dipole operator.

Now, we rewrite the field into positive and negative frequency components $\mathbf{E}^{(+)}$ and $\mathbf{E}^{(-)}$:

$$\begin{aligned}\mathbf{E}(t) &= \hat{\epsilon}E_0\cos(\omega t)\\ &= \hat{\epsilon}\frac{E_0}{2}(e^{-i\omega t} + e^{i\omega t})\\ &= \mathbf{E}^{(+)} + \mathbf{E}^{(-)}.\end{aligned} \tag{4.5}$$

Here, E_0 is the field amplitude and $\hat{\epsilon}$ is the unit polarization vector of the field. Using the atomic lowering operator $\sigma = |g\rangle\langle e|$, the dipole operator becomes

$$\mathbf{d} = \langle g|\mathbf{d}|e\rangle\,(\sigma + \sigma^\dagger). \tag{4.6}$$

Using Eqn. 4.5 and Eqn. 4.6, we can now write the Hamiltonian into

$$H = \hbar\omega_0\sigma^\dagger\sigma + \frac{\hbar\Omega}{2}(\sigma e^{-i\omega t} + \sigma e^{i\omega t} + \sigma^\dagger e^{-i\omega t} + \sigma^\dagger e^{i\omega t}). \tag{4.7}$$

We have defined the Rabi frequency that characterizes the interaction strength as

$$\Omega = -\frac{\langle g|\hat{\epsilon}\cdot\mathbf{d}|e\rangle\, E_0}{\hbar}. \tag{4.8}$$

In general, we can choose the phase of the dipole matrix element such that the Rabi frequency is real and positive.

With the Hamiltonian in Eqn. 4.7, substitution of $|\psi\rangle$ into the Schrödinger equation $i\hbar\partial_t|\psi\rangle = H|\psi\rangle$ results in

$$\partial_t c_g|g\rangle + \partial_t c_e|e\rangle = -i\omega_0 c_e|e\rangle - i\frac{\Omega}{2}[(e^{-i\omega t} + e^{i\omega t})c_e|g\rangle + (e^{-i\omega t} + e^{i\omega t})c_g|e\rangle]. \tag{4.9}$$

By projecting onto $\langle g|$ and $\langle e|$, we can get a pair of coupled differential equations,

$$\begin{aligned}\partial_t c_g &= -i\frac{\Omega}{2}(e^{-i\omega t} + e^{i\omega t})c_e \\ \partial_t c_e &= -i\omega_0 c_e - i\frac{\Omega}{2}(e^{-i\omega t} + e^{i\omega t})c_g.\end{aligned} \tag{4.10}$$

In order to eliminate the oscillatory terms in the coupled equation, we make a transformation into the rotating frame of the field by defining $\tilde{c}_e = c_e e^{i\omega t}$. The coupled equation in the rotating frame is written as

$$\begin{aligned}\partial_t c_g &= -i\frac{\Omega}{2}(1 + e^{-i2\omega t})\tilde{c}_e \\ \partial_t \tilde{c}_e &= i\Delta\tilde{c}_e - i\frac{\Omega}{2}(1 + e^{i2\omega t})c_g,\end{aligned} \tag{4.11}$$

where $\Delta = \omega - \omega_0$ is the detuning of the field from the resonance of the two-level system. In the rotating wave approximation (RWA), we can ignore the $e^{-i2\omega t}$ and $e^{i2\omega t}$ term in Eqn. 4.11 because these dynamics are oscillating at twice the field frequency. We can then rewrite the coupled equation as

$$\begin{aligned}\partial_t c_g &= -i\frac{\Omega}{2}\tilde{c}_e \\ \partial_t \tilde{c}_e &= i\Delta\tilde{c}_e - i\frac{\Omega}{2}c_g.\end{aligned} \tag{4.12}$$

From Eqn. 4.12, we can infer the effective Hamiltonian in the rotating frame

$$\begin{aligned}\tilde{H} &= \tilde{H}_0 + \tilde{H}_I \\ &= -\hbar\Delta\sigma^\dagger\sigma + \frac{\hbar\Omega}{2}(\sigma + \sigma^\dagger).\end{aligned} \tag{4.13}$$

In this frame where the field is stationary, the energy of the excited state is shifted by $\hbar\omega$, and the energy difference between $|g\rangle$ and $|e\rangle$ become $\hbar\Delta$. This effectively transforms the problem into an interaction between two states with an energy difference of $\hbar\Delta$ and a dc electric field. Thanks to RWA, this problem will be easier to solve due to the elimination of the explicit time dependence in the Hamiltonian.

The uncoupled energy basis $|g\rangle$ and $|e\rangle$ are no longer the eigenstates of Eqn. 4.13. We can work out the new eigenenergies to be superpositions of the uncoupled energy basis

$$E_{\pm} = \frac{\hbar}{2}(-\Delta \pm \Omega'), \tag{4.14}$$

with the generalized Rabi frequency $\Omega' = \sqrt{\Omega^2 + \Delta^2}$. The corresponding eigenstates are given as

$$\begin{aligned} |+\rangle &= \sin\theta\,|g\rangle + \cos\theta\,|e\rangle \\ |-\rangle &= \cos\theta\,|g\rangle - \sin\theta\,|e\rangle\,, \end{aligned} \tag{4.15}$$

where the angle θ is defined as $\tan 2\theta = -\Omega/\Delta$. These are the dressed states of the atom as a result of interaction with the field. In the case of exact resonance ($\Delta = 0$), the two energy states would be degenerate when the coupling field does not exist. However, the two degenerate states start to split when we turn on the coupling field and the splitting is proportional to the coupling strength. This shift of the eigenenergies at the avoided crossing is also known as AC stark shift.

Next, we include the impact of spontaneous decay in our formulation. In the rotating frame, we solve the master equation for the density matrix $\tilde{\rho} = |\tilde{\psi}\rangle\langle\tilde{\psi}|$,

$$\partial_t\tilde{\rho} = -\frac{i}{\hbar}\left[\tilde{H}, \tilde{\rho}\right] + \mathcal{L}\left[\tilde{\rho}\right], \tag{4.16}$$

where $\mathcal{L}\left[\tilde{\rho}\right]$ is the Lindblad operator accounting for spontaneous decay. Considering the case for homogeneous broadening, we can obtain the optical Bloch equations

$$\begin{aligned} \partial_t\rho_{ee} &= i\frac{\Omega}{2}(\tilde{\rho}_{eg} - \tilde{\rho}_{ge}) - \Gamma\rho_{ee} \\ \partial_t\rho_{gg} &= -i\frac{\Omega}{2}(\tilde{\rho}_{eg} - \tilde{\rho}_{ge}) + \Gamma\rho_{ee} \\ \partial_t\tilde{\rho}_{ge} &= -i\frac{\Omega}{2}(\rho_{ee} - \rho_{gg}) - (\frac{\Gamma}{2} + i\Delta)\tilde{\rho}_{ge} \\ \partial_t\tilde{\rho}_{eg} &= i\frac{\Omega}{2}(\rho_{ee} - \rho_{gg}) - (\frac{\Gamma}{2} - i\Delta)\tilde{\rho}_{ge} \end{aligned} \tag{4.17}$$

with Γ as the excited state decay rate. The matrix element $\tilde{\rho}_{gg}$ and $\tilde{\rho}_{ee}$ that represent the populations remain the same in this frame while the coherences differ by a phase factor,

$$\begin{aligned}
\tilde{\rho}_{gg} &= c_g c_g^* = \rho_{gg} \\
\tilde{\rho}_{ee} &= \tilde{c}_e \tilde{c}_e^* = c_e c_e^* = \rho_{ee} \\
\tilde{\rho}_{ge} &= c_g \tilde{c}_e^* = c_g c_e^* e^{-i\omega t} = \rho_{ge} e^{-i\omega t} \\
\tilde{\rho}_{eg} &= \rho_{eg} e^{i\omega t}.
\end{aligned} \tag{4.18}$$

In many applications, it is sufficient to know the steady state of the system, i.e. the solutions of the Eqn. 4.17 under the condition of $\partial_t \rho = 0$. After a little algebra, we find the steady-state population and coherence to be

$$\begin{aligned}
\rho_{ee}(t \to \infty) &= \frac{\Omega^2/\Gamma^2}{1 + (2\Delta/\Gamma)^2 + (2\Omega^2/\Gamma^2)} = \frac{1}{2}\frac{s}{1+s} \\
|\tilde{\rho}_{eg}(t \to \infty)|^2 &= |\frac{\Omega(2\Delta - i\Gamma)}{\Gamma^2 + (2\Delta)^2 + 2\Omega^2}|^2 = \frac{1}{2}\frac{s}{(1+s)^2}.
\end{aligned} \tag{4.19}$$

Here we introduce the saturation parameter, s as

$$s = \frac{2\Omega^2}{\Gamma^2 + 4\Delta^2}. \tag{4.20}$$

For the case of on resonance excitation ($\Delta = 0$), we can define the saturation intensity, I_s as

$$\frac{I}{I_s} = \frac{2\Omega^2}{\Gamma^2} = s_{(\Delta=0)}, \tag{4.21}$$

where $I = (\epsilon_0 c/2)E_0^2$ is the excitation field intensity. The saturation intensity is a quantity that sets a scale over what we mean by large or small intensities. When the excitation intensity is small relative to the saturation intensity, the steady-state excited state population increases linearly with the intensity. As the intensity increases above I_s, the excited state population begins to saturate towards one half, given that $\Delta = 0$. The saturation behavior here illustrates the nonlinear response of the two-level system interacting with the field, which is not predicted classically.

4.2.2 Correlation functions

Correlation functions of the light emitted by the two-level atom can give us some insights into the characteristics of the fluorescence itself. The normalized first

and second-order correlation function of the field emitted by the atom are formally defined as

$$\begin{aligned} g^{(1)}(\tau) &= \frac{\langle E^{(-)}(t)E^{(+)}(t+\tau)\rangle}{\langle E^{(-)}(t)E^{(+)}(t)\rangle} \\ g^{(2)}(\tau) &= \frac{\langle E^{(-)}(t)E^{(-)}(t+\tau)E^{(+)}(t+\tau)E^{(+)}(t)\rangle}{\langle E^{(-)}(t)E^{(+)}(t)\rangle^2}. \end{aligned} \tag{4.22}$$

Adapting the source field expression from [127], the field emitted from the two-level atom can be written quantum mechanically in terms of the atomic lowering and raising operator. The correlation functions in Eqn. 4.22 now become

$$\begin{aligned} g^{(1)}(\tau) &= \frac{\langle \sigma^\dagger(t)\sigma(t+\tau)\rangle}{\langle \sigma^\dagger(t)\sigma(t)\rangle} \\ g^{(2)}(\tau) &= \frac{\langle \sigma^\dagger(t)\sigma^\dagger(t+\tau)\sigma(t+\tau)\sigma(t)\rangle}{\langle \sigma^\dagger(t)\sigma(t)\rangle^2}. \end{aligned} \tag{4.23}$$

Immediately we can see that for a single two-level atom, the intensity correlation function at $\tau = 0$, $g^{(2)}(0)$ is zero since σ^2 vanishes. The atom is in the ground state after it emits a photon and cannot emit again until it is being excited to the excited state. As such, the probability to detect a second photon at $\tau = 0$ is zero. This phenomenon known as antibunching is manifestly quantum. For classical fields, the relation $\langle I(t)^2\rangle \geq \langle I(t)\rangle^2$ inferred from Cauchy's inequality ensures that $g^{(2)}(\tau) \geq 1$ for all time τ. Photon antibunching was first demonstrated experimentally by Kimble *et al.* in 1977 [128].

While a vanishing intensity correlation is a clear indication of antibunching, the dynamic of $g^{(2)}(\tau)$ near $\tau = 0$ reveals more about the underlying atom-light interaction such as a Rabi oscillation. Using the quantum regression theorem [127, 129], we can write the intensity correlation function as

$$g^{(2)}(\tau) = \frac{\rho_{ee}(\tau)}{\rho_{ee}(t \to \infty)}, \tag{4.24}$$

where $\rho_{ee}(\tau)$ is the excited state population with the initial condition $\rho_{ee}(0) = 0$. For the case where detuning is zero, the optical Bloch equation can be solved analytically and the $g^{(2)}(\tau)$ for a single atom can be expressed as [127]

$$g^{(2)}(\tau) = 1 - e^{-(3\Gamma/4)|\tau|}\left(\cos\Omega_\Gamma\tau + \frac{3\Gamma}{4\Omega_\Gamma}\sin\Omega_\Gamma|\tau|\right), \tag{4.25}$$

where $\Omega_\Gamma = \sqrt{\Omega^2 - (\Gamma/4)^2}$ is the damped Rabi frequency.

For driving fields of low intensity, $g^{(2)}(\tau)$ shows a monotonic increase to unity as τ increases from zero to much larger than $1/\Gamma$. When the driving field intensity increases above saturation, $g^{(2)}(\tau)$ resembles the case for weak excitations at the large delay, but oscillations corresponding to the Rabi frequency appear around zero delay. Upon detection of the first fluorescence photon, the atom is projected onto the ground state and the probability to detect the subsequent photon at some later time, τ is proportional to the excited state population of the atom. As such, this oscillation can be seen as an indication of the Rabi flopping undergone by the atom under a strong excitation.

4.2.3 Coherent & Incoherent Scattering

In atom-light interaction, light scattering is a second-order process that involves the absorption of a photon at frequency ω_L and followed by the emission of a photon at frequency ω_{sc}. This scattering primarily consists of two contributions - coherent and incoherent scattering. The coherent scattering includes emitted photon that has the same frequency as the excitation field ($\omega_{sc} = \omega_L$). In contrast, the incoherent scattering includes all of the remaining components of the fluorescence, with ω_{sc} different from ω_L.

Information on the coherent component (on the first-order) of the scattered field can be extracted through the expectation value of the field operators $E_{sc}^{(-)}$ and $E_{sc}^{(+)}$. The fraction of the first-order coherently scattered light is described as [127]

$$\frac{\bar{I}_{sc}^{coh}}{\bar{I}_{sc}} = \frac{\langle E_{sc}^{(-)}(t)\rangle\langle E_{sc}^{(+)}(t)\rangle}{\langle E_{sc}^{(-)}(t)E_{sc}^{(+)}(t)\rangle}. \tag{4.26}$$

This fraction reaches unity when the scattering is purely coherent. Through the same procedure as in Eqn. 4.23, we can write Eqn. 4.26 in terms of the atomic lowering and raising operator. The steady-state ratio is given as

$$\begin{aligned}\frac{\bar{I}_{sc}^{coh}}{\bar{I}_{sc}} &= |g^{(1)}(t \to \infty)| \\ &= \frac{\langle \sigma^\dagger(t \to \infty)\rangle\langle \sigma(t \to \infty)\rangle}{\langle \sigma^\dagger(t \to \infty)\sigma(t \to \infty)\rangle} \\ &= \frac{|\tilde{\rho}_{eg}(t \to \infty)|^2}{\rho_{ee}(t \to \infty)},\end{aligned} \tag{4.27}$$

where $\tilde{\rho}_{eg}$ and ρ_{ee} are the atomic density matrix elements. Combined with the solutions of the optical Bloch equations in Eqn. 4.19, we obtain the fraction of

coherently scattered light at steady state

$$\frac{\bar{I}_{sc}^{coh}}{\bar{I}_{sc}} = \frac{\Delta^2 + (\Gamma/2)^2}{\Delta^2 + (\Gamma/2)^2 + \Omega^2/2} = \frac{1}{1+s}, \tag{4.28}$$

where s is the saturation parameter.

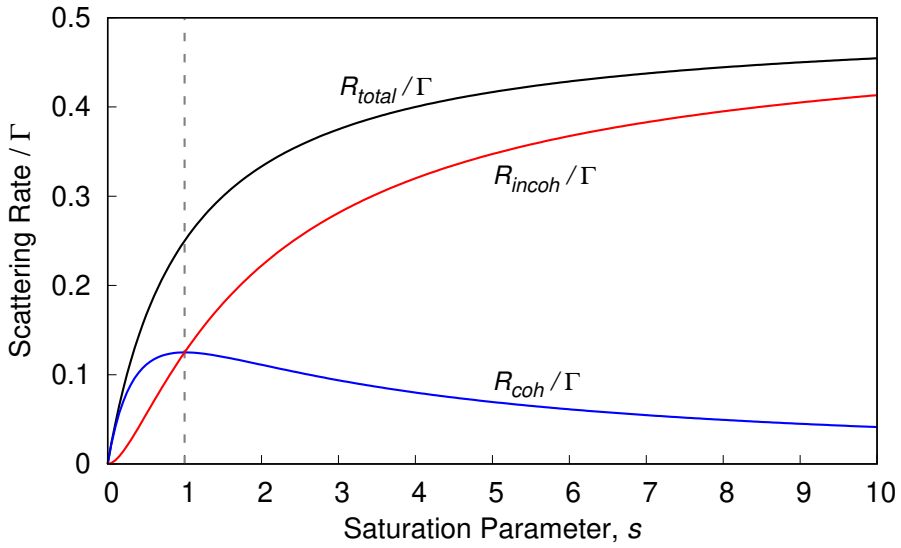

Figure 4.1: Dependence of total, coherent and incoherent scattering rate in units of Γ as a function of saturation parameter. At $s = 1$, the coherent scattering reaches its maximum and the incoherent scattering starts to dominate.

The total scattering rate is given by the product of the excited state population and decay rate

$$R_{total} = \Gamma \rho_{ee}(t \to \infty) = \frac{\Gamma}{2} \frac{s}{1+s}. \tag{4.29}$$

Since the scattering rate scales with the emission intensity, we can obtain the coherent scattering rate from Eqn. 4.28

$$R_{coh} = R_{total} \frac{1}{1+s} = \frac{\Gamma}{2} \frac{s}{(1+s)^2}. \tag{4.30}$$

The incoherent scattering rate can be deduced from the difference of R_{total} and R_{coh}

$$R_{incoh} = R_{total} - R_{coh} = \frac{\Gamma}{2} \frac{s^2}{(1+s)^2}. \tag{4.31}$$

Figure 4.1 shows the different contributions to the scattering rate as a function of the saturation parameter. When the saturation parameter is small, the coherent scattering grows linearly with s and dominates over the incoherent scattering. The

coherent scattering reaches an absolute maximum at $s = 1$ and decreases when s gets larger while the incoherent contribution starts to increase and saturates.

Apart from the difference in scaling with respect to the excitation intensity, the coherent and incoherent components of the fluorescence also have distinct spectral distributions. For the remaining part of this section, we consider the case where the excitation light is exactly on resonant with the atomic transition, where $\omega_L = \omega_0$. Using the Wiener–Khinchin theorem, the power spectrum $S(\omega_{sc})$ of the resonance fluorescence can be calculated as the Fourier transform of its first-order correlation function

$$S(\omega_{sc}) = \frac{1}{2\pi} \int_{-\infty}^{\infty} \mathrm{d}\tau g^{(1)}(\tau) e^{i\omega_{sc}\tau}. \tag{4.32}$$

We decompose the correlation function $g^{(1)}(\tau)$ of the fluorescence into coherent and incoherent contributions. The coherent part of $g^{(1)}(\tau)$ can be written as [127]

$$\begin{aligned} g^{(1)}_{coh}(\tau) &= e^{-i\omega_L\tau} |g^{(1)}(t \to \infty)| \\ &= e^{-i\omega_L\tau} \frac{1}{1+s}, \end{aligned} \tag{4.33}$$

with the result from Eqn. 4.28.

In order to compute the complete power spectrum that contains both coherent and incoherent contributions, we can solve the optical Bloch equations in Eqn. 4.17, and obtain

$$S(\omega) = S_{\mathrm{coh}}(\omega) + S_{\mathrm{incoh}}(\omega), \tag{4.34}$$

with

$$S_{\mathrm{coh}}(\omega) = \frac{s}{(1+s)^2} \delta(\omega), \tag{4.35}$$

$$\begin{aligned} S_{\mathrm{incoh}}(\omega) = &\frac{s}{8\pi(1+s)} \frac{\Gamma}{\omega^2 + (\Gamma/2)^2} \\ &+ \frac{s}{32\pi(1+s)^2} \frac{3\Gamma(s-1) + \frac{\Gamma}{\Omega}(5s-1)(\omega+\Omega)}{(\omega+\Omega)^2 + (3\Gamma/4)^2} \\ &+ \frac{s}{32\pi(1+s)^2} \frac{3\Gamma(s-1) - \frac{\Gamma}{\Omega}(5s-1)(\omega-\Omega)}{(\omega-\Omega)^2 + (3\Gamma/4)^2}, \end{aligned} \tag{4.36}$$

where ω is the relative frequency from the monochromatic driving field ($\omega = \omega_L - \omega_0$), and Γ represents the natural linewidth of the atomic transition, which in this case is $2\pi \times 6.07\,\mathrm{MHz}$ for $^{87}\mathrm{Rb}$ D_2 transition.

When the monochromatic driving field is weak ($s \ll 1$), the fluorescence consists mostly of light scattered elastically by the atom. This coherent component is characterized by a Dirac delta function at the driving frequency (Eqn. 4.35), which appears as a sharp peak at the driving frequency in the spectrum that resembles the spectrum of the driving field. As the driving intensity increases, the incoherently component in the scattered light starts to emerge in the spectrum, while the coherent component will gradually reduce. The incoherent component dominates the spectrum as Rabi frequency Ω increases, and the sidebands begin to emerge.

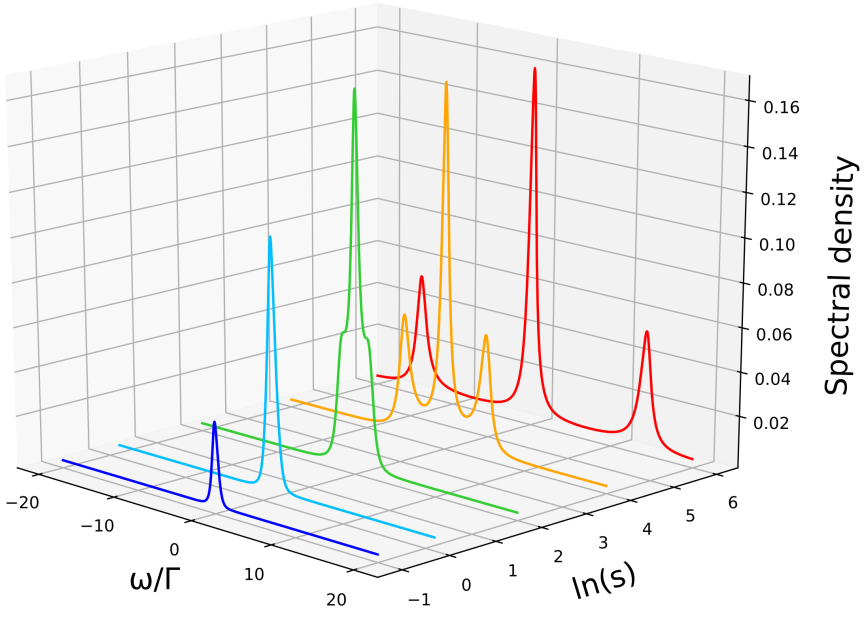

Figure 4.2: Theoretical resonant fluorescence spectra at different saturation parameter, s according to Eqn. 4.36.

The incoherent power spectrum $S_{\text{incoh}}(\omega)$ has a central resonant Lorentzian peak with a full-width half maximum (FWHM) of Γ as well as two side peaks $\pm\Omega$ away from the resonance, with a FWHM of $3\Gamma/2$. These sidebands, together with the central peak, form the Mollow triplet. This result was derived by Mollow using a semi-classical approach [98], but the same result can be obtained using a fully quantum-mechanical picture [130].

4.2.4 Dressed state picture

One way to interpret the spectral features is to describe the atomic energy states as dressed by the driving field [102, 131]. In the previous section, we discussed how the dressed states result from the interaction between an atom and a classical field.

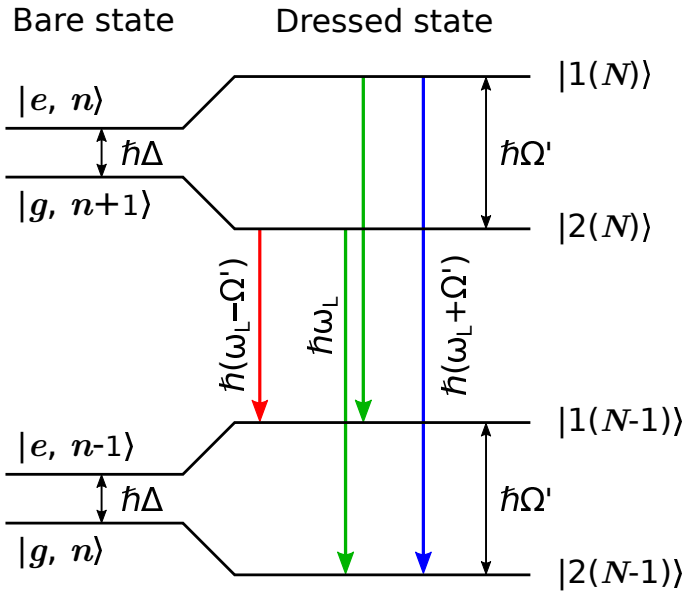

Figure 4.3: Dressed-state picture for an atom coupling to an intense driving field. Bare states are characterized by the photon number Fock state (n), and the atom in the ground (g) or excited (e) state. Their energy difference is $\hbar\Delta$ in the rotating frame, where Δ is the detuning of the driving field from atomic resonance. Dressed states are described by a pair of states with a number of total excitations, N, split by $\hbar\Omega'$ with a generalized Rabi frequency $\Omega' = \sqrt{\Omega^2 + \Delta^2}$.

We can extend this result to the case of the atom interacting with a quantized field. In this picture, the new eigenstates are a superposition of the bare states $|g, n+1\rangle$ and $|e, n\rangle$, where "g" and "e" refer to the ground and excited states of the atom, while n indicates the number of photons from the driving field (see Fig. 4.3). In every manifold where the total number of excitations, N, is the same, the eigenstates are split by the Rabi frequency for on-resonance excitation.

The three frequency components in the fluorescence can be explained by spontaneous decay from a manifold of N total excitations to a manifold with $(N-1)$ excitations. Four optical transitions are possible in this process. Two of them are degenerate (green decays in Fig. 4.3) and correspond to the central peak in the

fluorescence spectrum, while the sidebands $\pm\Omega$ away from the central peak originate from the other two transitions (red and blue decays in Fig. 4.3).

For on-resonance excitation, both the dressed states are the equal superposition of the two bare states. As such, we would expect the four possible decays will occur at the same rate. This leads to the weighting of 1:2:1 in the total spectral intensities of the incoherent peaks under resonant excitation. Note that this picture is most useful when $\Omega \gg \Gamma$ where the dressed state transitions are spectrally resolved.

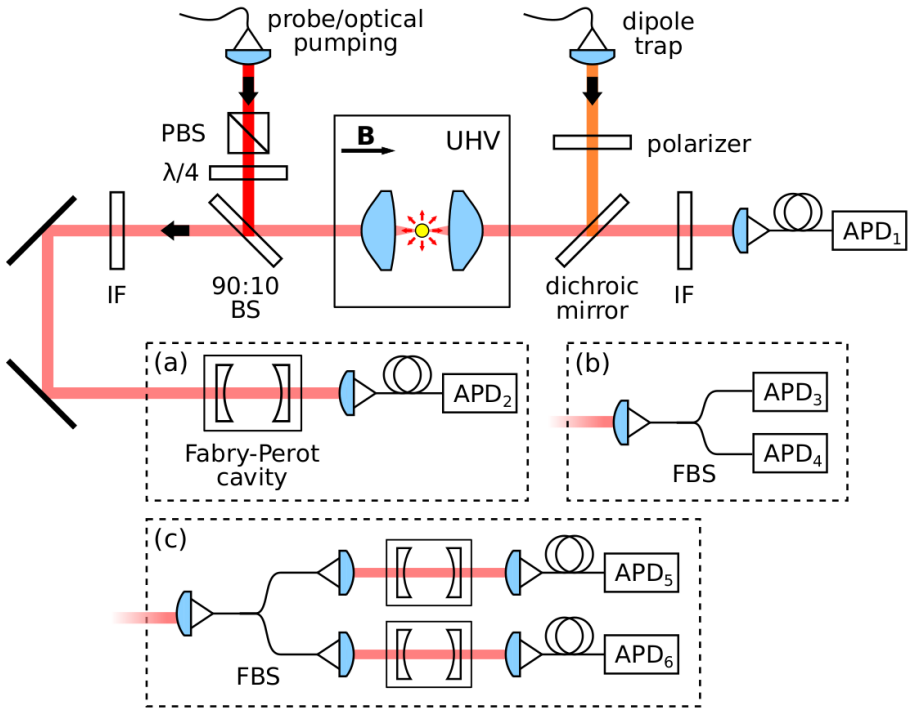

Figure 4.4: Setup for probing light-atom interaction in free space. A single ^{87}Rb atom is cooled and trapped in a far-off-resonance dipole trap. One avalanche photodetector (APD_1) is used to monitor the atomic fluorescence and acts as a trigger to start the experimental sequence. (a) A Fabry-Perot cavity is placed before APD_2 to record the frequency spectrum of the atomic fluorescence. (b) Hanbury-Brown and Twiss (HBT) configuration to measure second-order intensity autocorrelation. (c) Cross-correlation measurement setup with a cavity in each arm before APD_5 and APD_6 to select photons from specific frequency windows. UHV: ultra-high vacuum chamber, IF: interference filter centered at 780 nm, $\lambda/4$: quarter-wave plate, PBS: polarizing beam splitter, FBS: fiber beam splitter, B: magnetic field.

4.3 Experimental Realization

In this section, we will describe the experimental setup and sequences that are crucial in the frequency spectrum and photon correlation measurements. The complete experimental setup is shown in Fig. 4.4.

We are probing the closed transition $5^2S_{1/2}\ |F = 2,\ m_F = -2\rangle \equiv |g\rangle$ to $5^2P_{3/2}$ $|F = 3,\ m_F = -3\rangle \equiv |e\rangle$ such that it resembles the ideal two-level system in the theoretical description. As such, we do not need to consider the complications in the spectrum that arise due to the multilevel structure of the system.

4.3.1 Experimental Sequence

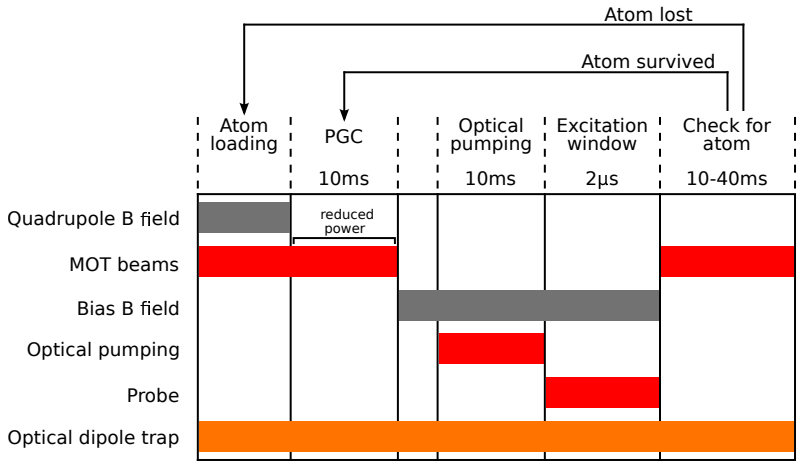

Figure 4.5: Experimental sequence to measure the frequency spectrum of the atomic fluorescence.

Fig. 4.5 outlines the experimental sequence. First, we monitor the fluorescence signal until a single atom is loaded into the FORT. Then we switch off the quadrupole field to prevent further loading of atoms into the trap. Next, we lower the power of the MOT beams and perform polarization gradient cooling (PGC) for 10 ms. This can reduce the atomic motion to a temperature of 14.7(2) μK, corresponding to a Doppler broadening of 113 kHz. A bias magnetic field of 1.44 mT is applied along the FORT laser propagation direction to remove the degeneracy of the Zeeman states, and the atom is optically pumped into $|g\rangle$ by optical pumping beam.

Now, we turn on the probe laser beam that propagates along the optical axis for 2 μs. This pulse length is chosen to maximize the duty cycle of photon collection

while avoiding excessive recoil heating of the atom. The probe frequency is locked to the $F = 2 \rightarrow F' = 3$ hyperfine transition of the ^{87}Rb D_2 line, and shifted by an AOM in order to address the $|g\rangle \leftrightarrow |e\rangle$ transition. The probe is prepared into a σ^- polarization with a quarter-wave plate after a polarizing beam splitter (PBS) to target the closed transition. We collect the backward scattered photons through the same lens and couple them into a single-mode fiber, avoiding the strong light levels of the probe laser for analysis.

After the probe phase, we check the presence of the atom by turning on the MOT beams and comparing the fluorescence rate with the set threshold. If the atom is present, the experimental sequence will be repeated from the PGC phase; else the quadrupole magnetic field will be turned on, and the experiment resumes with the atom loading phase. We repeat this sequence over many experimental cycles until we gather sufficient data for analysis.

4.3.2 Fluorescence Characterization

Before we proceed to measure the frequency spectrum of the fluorescence, we first perform a saturation measurement to determine the overall detection efficiency. By increasing the probe power, we can gauge how strongly we can excite the single atom in terms of the saturation parameter s.

Using the same experimental sequence described above, we detect the backscattered photon with avalanche photodetectors, APD_b under different probe powers, while the incident power on the atom is inferred by the number of photons detected by APD_f in the forward direction, after taking into account the total detection efficiency in the forward direction, η_f.

In our system, we characterize η_f to be 0.0109 when we measure the data in Fig. 4.6, taking into account the fiber coupling (62% coupling efficiency), detector efficiency (56% detection efficiency), and attenuation of the neutral density filter (3.15% transmission) used to prevent the saturation of the detector. With this, we can infer the incident probe power on the atom, P_{probe}, to be

$$P_{\text{probe}} = \frac{R_f}{\eta_f} \hbar \omega_L, \tag{4.37}$$

where R_f is the number of photons detected per second at APD_f, and ω_L is the frequency of the laser.

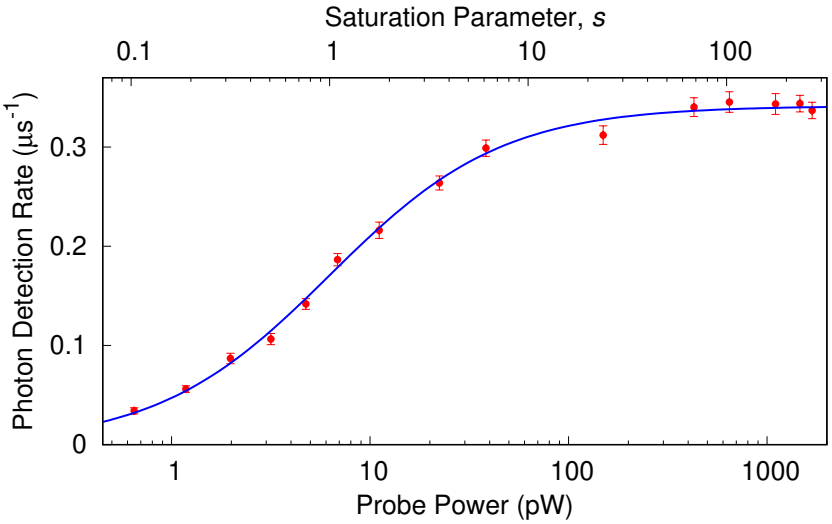

Figure 4.6: Resonant saturation measurement, with the blue solid line representing the fit to Eqn. 4.38 with saturation power $P_{\text{sat}} = 6.3(2)\,\text{pW}$ and total detection efficiency $\eta = 1.79(2)\,\%$.

In the result shown in Fig. 4.6, we can clearly observe the saturation behavior of the scattering rate as the probe power increases. The scattering rate R_{sc} is expected to follow a saturation function

$$R_{sc} = \frac{\eta\Gamma}{2}\frac{P_{\text{probe}}}{P_{\text{probe}} + P_{\text{sat}}}. \tag{4.38}$$

From the fit in Fig. 4.6, we can infer that the atomic response saturates at an incident probe power of $P_{\text{sat}} = 6.3(2)\,\text{pW}$ and total detection efficiency of the atomic fluorescence is $\eta = 1.79(2)\,\%$. These values are similar to the previous reported in [42].

4.3.3 Fabry-Perot Cavity

A Fabry-Perot cavity is the core component in our setup measuring the frequency spectrum of atomic fluorescence. For this experiment, we use a home-built cavity with the structure shown in Fig. 4.7.

The main part of the cavity is a metal block with a through hole. A ring piezo that is responsible for the fine adjustment of the cavity length is glued to one end of the hole. To connect the cavity mirror with the piezo, we use the Thorlabs ⌀1/2" lens tube to hold the mirror. The position of the mirror can be adjusted using

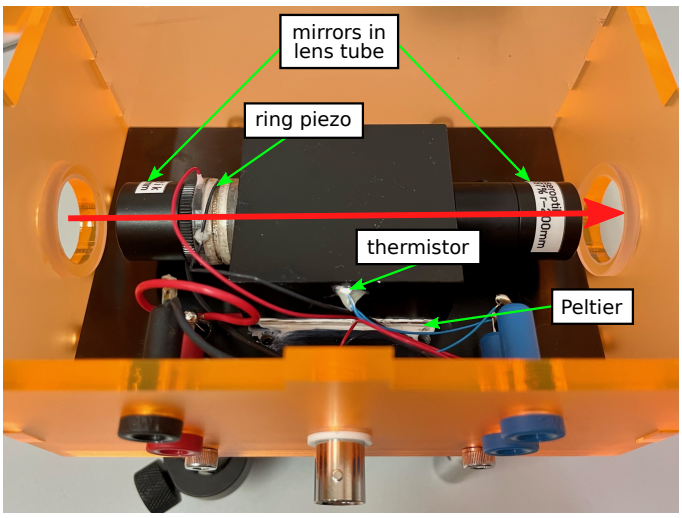

Figure 4.7: A photo of the home-built cavity enclosed in an acrylic box. The red arrow indicates the laser beam path. The cavity mirrors are held by lens tubes that are connected to the cavity body. To avoid cavity length drift due to thermal expansion, we stabilize the cavity temperature with a Peltier controlled by a PID control loop to about $\pm 5\,\mathrm{mK}$. The cavity resonance is manipulated by a ring piezo that modifies the cavity length.

the retainer ring and the tube is screwed into a threaded ring that sticks on the other end of the piezo. Using the same method, another mirror is connected to the internally threaded hole on the other side of the metal block.

The advantage of this design is the flexibility to vary the cavity linewidth without modifying the mode-matching alignment. For example, we can replace the existing mirror with another mirror that has the same radius of curvature but different reflectivity at the same location in the lens tube. By doing so, the mode mismatch of the incoming light into the cavity is minimal and can be recovered in a short time. For the measurement in Section 4.3.6, this configuration enabled us to change the cavity linewidth to 20 MHz without too much hassle. It will also allows to measure the photon statistic of the coherent and incoherent scattering separately by using different filter widths to isolate the respective component [106–108].

In terms of temperature control, we sandwich a Peltier in between the metal block and a heatsink. We can monitor the temperature of the cavity through a thermistor that is attached to it. Using a PID control system, we stabilize the cavity temperature to the desired setpoint by voltage feedback into the Peltier. In this way,

the change in cavity length due to thermal expansion will be minimized.

Next, we need to connect the cavity resonance to a known frequency reference and still be able to tune the resonance across a frequency range to obtain the atomic spectrum. We do this by employing a Pound–Drever–Hall (PDH) technique to lock the cavity to a 795 nm laser that is resonant with the ^{87}Rb D_1 transition. The detail of this locking scheme is shown in Fig. 4.8.

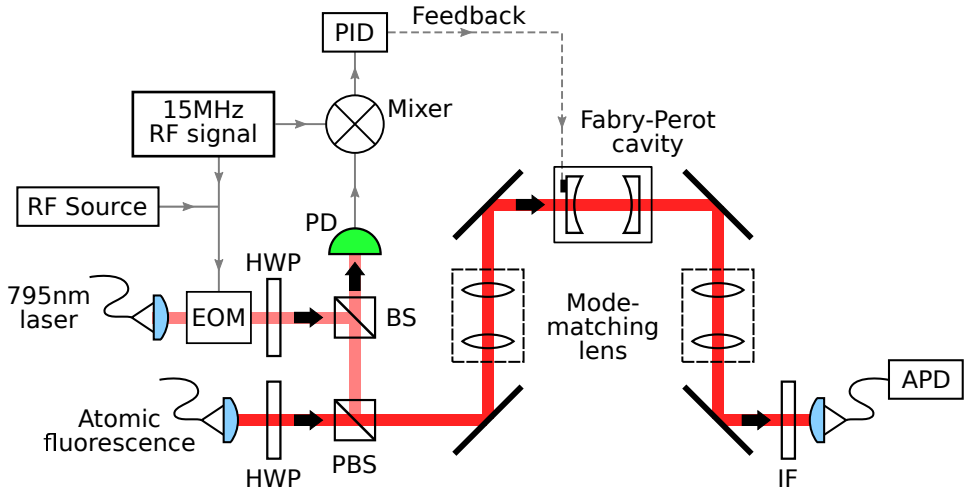

Figure 4.8: Schematic of the cavity locking setup. The locking sequence starts with a 795 nm laser that is locked onto the ^{87}Rb D_1 transition. An electro-optical modulator (EOM) generates a tunable sideband (from a RF source) that is further modulated with a frequency of 15 MHz. By coupling this light to the cavity, the cavity resonance can be locked onto this tunable sideband via the Pound–Drever–Hall (PDH) technique. The photodetector (PD) signal generated from the reflected light is mixed with the 15 MHz signal to create an error signal. The PID controller turns this signal into a feedback to the cavity piezo to lock the cavity to the tunable sideband. A 780 nm interference filter (IF) is placed before the APD to prevent the collection of 795 nm light.

The 795 nm laser is phase-modulated with a frequency of 15 MHz via an electro-optical modulator (EOM) to generate two sidebands. The modulated light is coupled to the cavity through the mode-matching lens, and the reflected signal that is modulated by the cavity transfer function will be detected on the photodetector (PD in Fig. 4.8). The detected signal is mixed with the RF source to produce error signals which indicates how far away the cavity resonance is from the laser carrier frequency. We use a PID controller to provide a control voltage for the cavity piezo. This will change the cavity length and in turn, lock the cavity resonance to the laser

carrier frequency. The long term stability provided by this locking scheme enabled us to measure the frequency spectrum of the fluorescence over a long period of time.

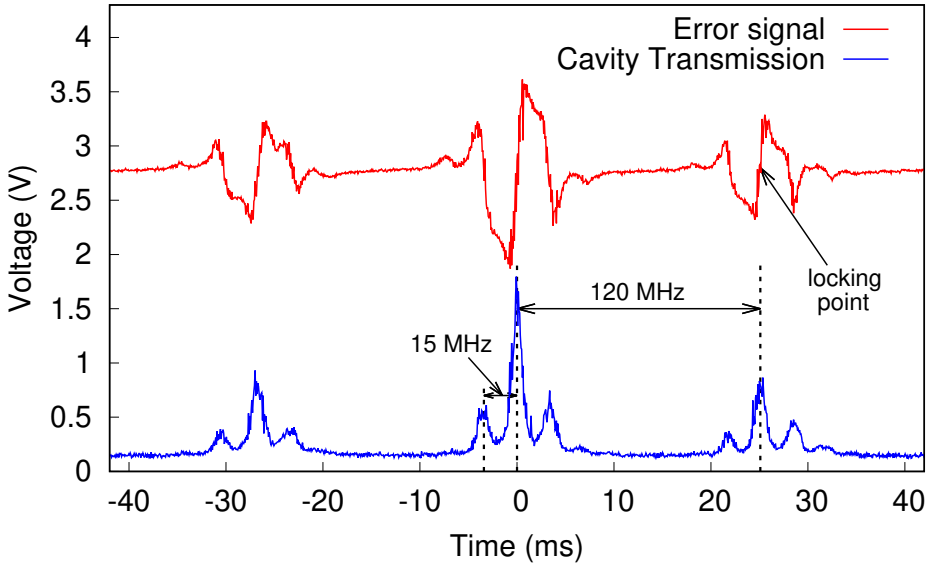

Figure 4.9: Oscilloscope trace showing the PDH error signal and the cavity transmission. We slowly change the cavity length to monitor the various sideband profiles in time. The peak around $t = 0$ is the carrier. A tunable modulation frequency, ω_m is sent into the EOM to create sidebands for locking purposes. In this example the ω_m is chosen to be $2\pi\times120$ MHz and the locking point is indicated with an arrow. By changing ω_m, we can control the cavity resonance. The 15 MHz sidebands are responsible for the generation of the PDH error signal. The error signal is shifted by 2.8 V for better visualization.

However, we want to be able to scan the cavity resonance around the collected fluorescence frequency. To achieve this, we send in another RF signal through a RF combiner to generate additional sidebands (Fig. 4.9) with a modulation frequency of $\omega_m/2\pi$. This $\omega_m/2\pi$ corresponds to the frequency difference between the 795 nm laser and the collected atomic fluorescence. Since the value of ω_m depend on the absolute length of the cavity, this frequency can be tuned by operating the cavity at the next or a few free spectral range away. The typical value of ω_m in our setup is around $2\pi\times200$ MHz. By locking the cavity resonance to this tunable sideband, we can measure the frequency spectrum of the atomic fluorescence by changing ω_m across the desired frequency range.

For the cavity used for spectrum measurement, it is a symmetric cavity with

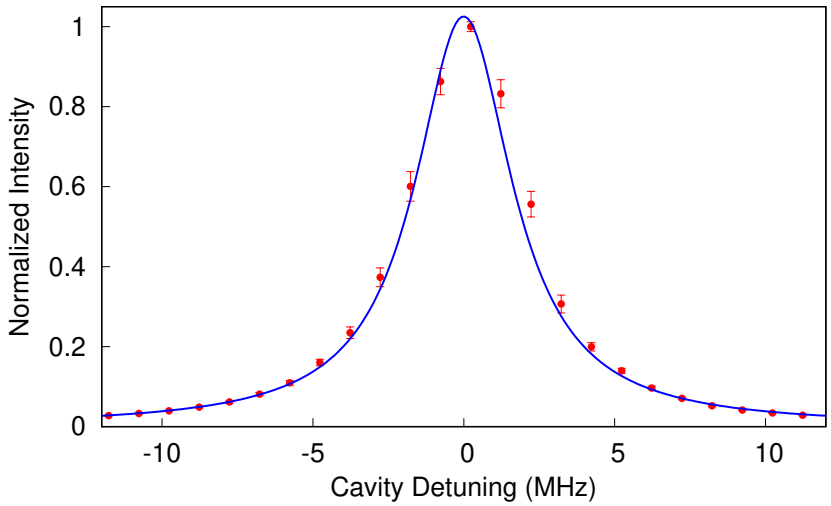

Figure 4.10: Cavity transmission of the probe laser to characterize the cavity linewidth. The blue solid line is a Lorentzian fit which results in a linewidth of 3.92(5) MHz.

mirror reflectivity of around 99 % at 780 nm and a curvature radius of 200 mm. The cavity length is 12 cm, corresponding to a linewidth of 4 MHz and a free spectral range of 1.25 GHz. With a good mode-matching into the cavity mode, a transmission of more than 95% was achieved. We characterize the cavity linewidth by changing the cavity resonance and measure the transmission of the probe light after the cavity. The result is shown in Fig. 4.10. A linewidth of 3.92(5) MHz can be extracted from a Lorentzian fit. This value will be used for the deconvolution of the atomic spectrum measured in the next section.

4.3.4 Mollow Triplet spectrum

The light collected during the 2 μs excitation window is sent into the cavity and the transmission is recorded with an APD as shown in Fig. 4.4(a). By repeating this procedure at different cavity resonant frequencies, we can obtain the atomic fluorescence spectrum.

Fig. 4.11 shows a series of frequency spectra for increasing excitation powers. At weak excitation, the FWHM of the single peak in Fig. 4.11(a) is 2.5(3) MHz after deconvolution of the cavity contribution. This shows that at a driving power that is well below saturation, the coherent component with a linewidth smaller than Γ

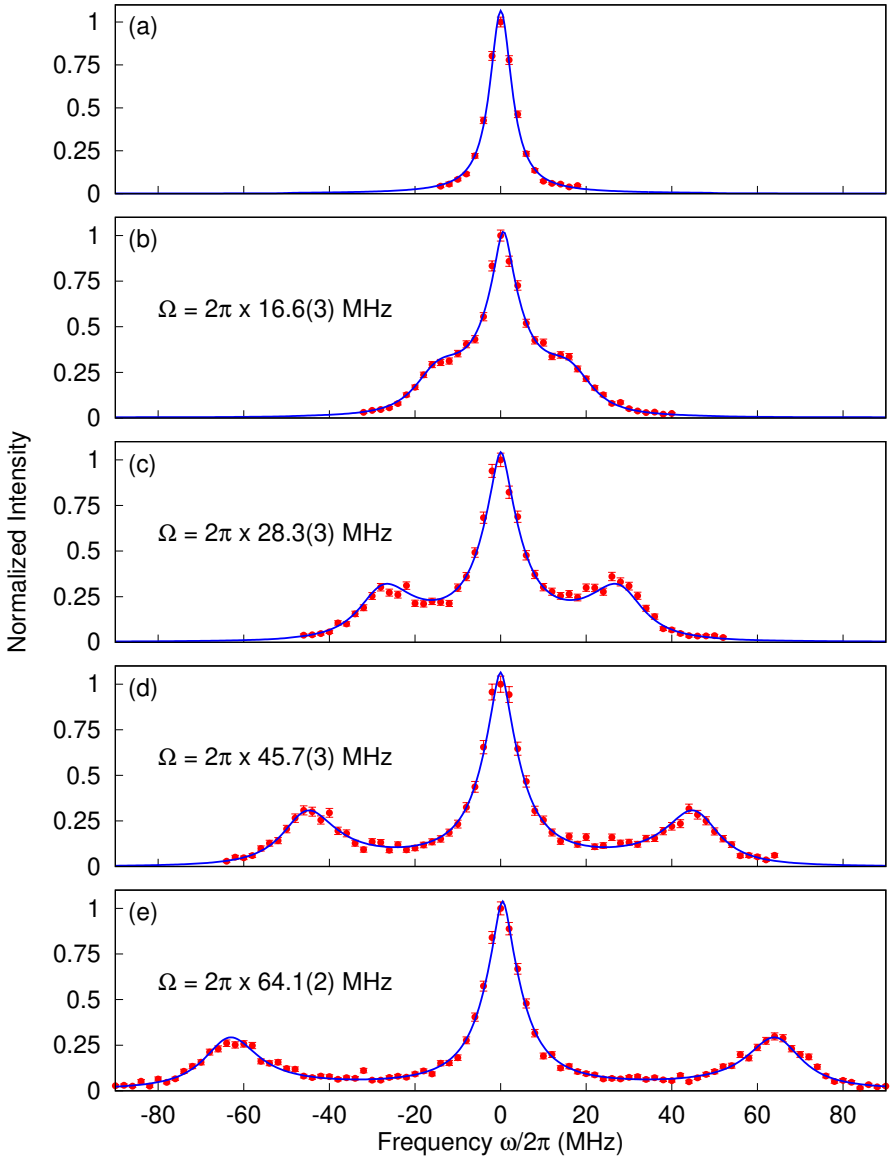

Figure 4.11: Normalized resonance atomic emission spectra at different excitation intensities recorded by scanning the Fabry-Perot cavity with the setup in Fig. 4.4(a). For (b)-(e), the solid line is a fit to Eqn. 4.34 convoluted with the cavity transfer function and the effect of laser reflection. The Rabi frequency Ω extracted from the fit is labeled in Fig. 4.11(b)-(e). The free parameters in these fits are Rabi frequency, natural linewidth, and laser reflection.

dominates the spectrum. The blue solid line in Fig. 4.11(a) is a fit to a Lorentzian function, convoluted with the cavity transfer function.

As the power increases, the three-peak structure emerges and the splitting between the peaks also increases. The fit to the experimental data is done with

Eqn. 4.34 convoluted with the cavity transfer function. After excluding cavity contribution, the central peak in Fig. 4.11(e) has a FWHM of 7.8(3) MHz extracted from the fit. This value is close to the atomic natural linewidth of ^{87}Rb, thus justifying the claim that an optically trapped single atom can be laser cooled to mitigate the Doppler broadening effect.

Theoretically, the height ratio between the central peak and the sidebands is $1:3:1$ according to Eqn. 4.34, owing to the fact that the sidebands have a larger width compared to the central peak. After taking into account the cavity contribution, the height of the central peak should decrease such that the ratio reaches around $1:2.6:1$. However, the measured spectra show central peaks with about 3.7 times the height of sidebands (average value of Fig. 4.11(c)-(e)). This inconsistency between the theoretical prediction and the experimental data can be likely attributed to the reflection and scattering of the probe laser from the optics. Taking this reflection into consideration by adding a term to Eqn. 4.34 that scales with power in a model to describe our experiment, we can extract how much power from the observed spectrum can be attributed to such a reflection. We characterized this laser reflection from the fit and found a contribution of 0.9 %, 2.4 % and 4.5 % to the total power in the spectra (c)-(e) in Fig. 4.11. This explained the higher central peak in the experimental measured spectra.

4.3.5 Second Order Correlation Function

In the subsequent part of the experiment, we replace the Fabry-Perot cavity with a fiber beam splitter and two APDs in a Hanbury-Brown and Twiss configuration [132] as shown in Fig. 4.4(b). The arrival time of the photons is recorded. The second-order intensity correlation function ($g^{(2)}(\tau)$) of the atomic fluorescence can be inferred through

$$g^{(2)}(\tau) = \frac{\langle P_1(t) P_2(t+\tau)\rangle}{\langle P_1(t)\rangle \langle P_2(t+\tau)\rangle}, \tag{4.39}$$

where $P_{1(2)}(t)$ is the probability to detect a photon at $\mathrm{APD}_{1(2)}$ at time t and $\langle \cdots \rangle$ denotes the statistical average.

The time delay τ between the photodetection events are sorted into a histogram. In order to obtain the expression in Eqn. 4.39, we normalize the histogram to

$$R_1 \times R_2 \times t_{\mathrm{bin}} \times T, \tag{4.40}$$

where $R_{1(2)}$ is the average count rate at $\mathrm{APD}_{1(2)}$, t_{bin} is the bin width of the delay histogram and T is the total measurement time. From the $g^{(2)}(\tau)$ result, the Rabi frequency Ω can be also extracted from the fit, and it serves as an independent measurement allowing comparison to the values obtained from the Mollow triplet spectrum measurement.

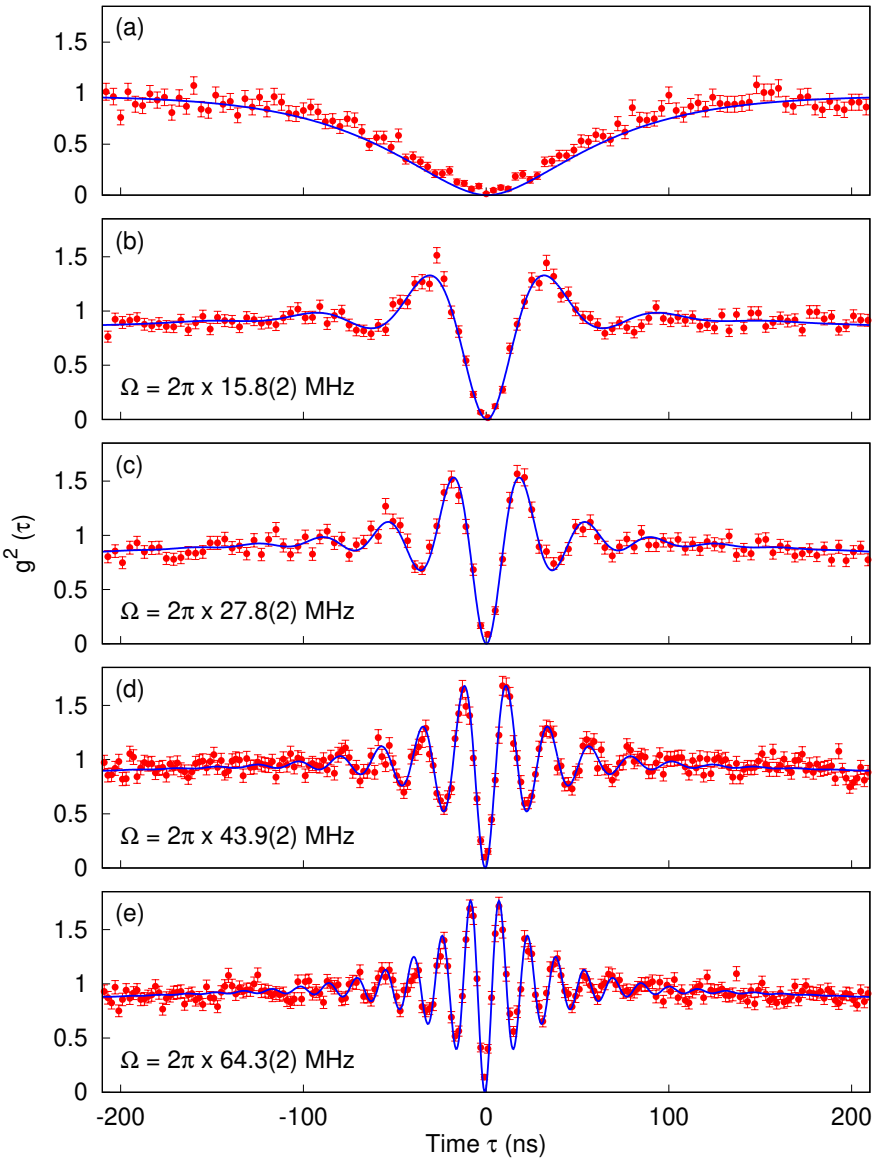

Figure 4.12: Second-order correlation function of the single atom at different excitation intensities. The solid line is a fit to Eqn. 4.25 with the inclusion of a triangular function resulting from a convolution of two square pulses. The Rabi frequency Ω shown for each spectrum is extracted from the respective fits.

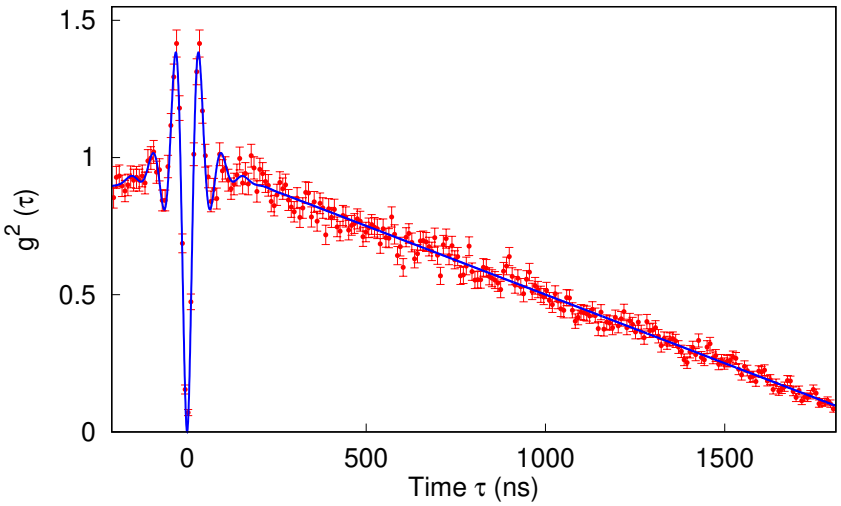

Figure 4.13: Decay of correlation due to finite collection window on a long time scale. For a collection window of 2 μs, the correlation will result in a 4 μs wide triangular envelope.

The correlation measurements in Fig. 4.12 are fitted using Eqn. 4.25, multiplied with a triangle function that results from the convolution of two square pulses of the same length. This is done to account for fluorescence from each detector being collected during a 2 μs wide time window. The correlation between two such windows will result in a 4 μs wide triangular envelope in the correlation measurement. This triangular envelope can be seen in Fig. 4.13 when the correlation at a longer time delay is plotted out. The extracted Rabi frequency, shown in Fig. 4.12 for different driving powers, agrees well with the values for Ω obtained from the Mollow triplet spectra.

4.3.6 Off-resonant excitation

Until this point, all the experiments have been carried out under the condition of on-resonant excitation. When the atom is excited off-resonantly, the spectrum of the fluorescence does not have a simple analytical solution. However, we can inspect this problem in the dressed state picture and get some useful information out of it. When we consider the case of very large detuning ($\Delta \gg \Gamma$), the splitting between the dressed states is given by the generalized Rabi frequency, $\Omega' = \sqrt{\Omega^2 + \Delta^2}$, where Δ is the detuning of the laser from atomic resonance. As compared to the

on-resonant case, the off-resonant spectrum is slightly different, with the central peak sitting at the driving frequency and two sidebands located $\pm\Omega'$ away. Due to the non-zero detuning, both the dressed states are no longer an equal superposition of the two bare states. At the limit of very large detuning ($\Delta \gg \Omega$), $|1(N)\rangle(|2(N)\rangle)$ consists mostly of $|e, n\rangle(|g, n+1\rangle)$. The decay from $|1(N)\rangle$ to $|1(N-1)\rangle$ ($|2(N)\rangle$ to $|2(N-1)\rangle$) happens at a much lower rate than the other two paths. As such, the power ratio between the central peak and the sidebands also deviates from the on-resonant case, with the central peak being suppressed as detuning increases.

While the atom is excited resonantly, the emission of the sideband photons does not have a preferred order. As such, the cross-correlation between photons from different sidebands is symmetric with respect to zero time delay, $\tau = 0$. However, if the excitation field is detuned from the atomic resonance, this symmetry is broken as the emission process of the sideband photons now has a preferred order [100–103]. The preferred order of the emission depends on the sign of the detuning, and manifests as an asymmetry in the cross-correlation measurement around $\tau = 0$.

In this part of the experiment, we red-detuned the excitation laser by 30 MHz from the atomic resonance. As shown in Fig. 4.4(c), there is a Fabry-Perot cavity in front of each APD to filter the incoming fluorescence such that photon correlation between chosen spectral components can be measured. To better transmit the photons from different peaks, the cavities used in this experiment have a linewidth of 20 MHz. The cavities are almost the same as the ones used in the spectrum measurement, with the only difference being the 95 % mirror reflectivity.

To align the cavity resonance with the respective sidebands, we first measure the second-order correlation of the off-resonance fluorescence. The data is shown in the inset of Fig. 4.14 and the solid blue line is fit to extract Ω', which is $2\pi \times 42(1)$ MHz in this case. For the off-resonant case, the second-order correlation function does not have a simple analytical form. As such, we numerically solve the optical Bloch equation and fit the measurement result to it according to Eqn. 4.24. With this, the cavity resonance is locked at $\pm\Omega'$ away from the driving frequency to isolate the sidebands photon.

Figure 4.14 shows the cross-correlation measurement between the opposite Mollow sidebands where we use the photon from the lower energy sideband as the 'start' trigger and the photon from the other sideband as the 'stop' signal. The measurement

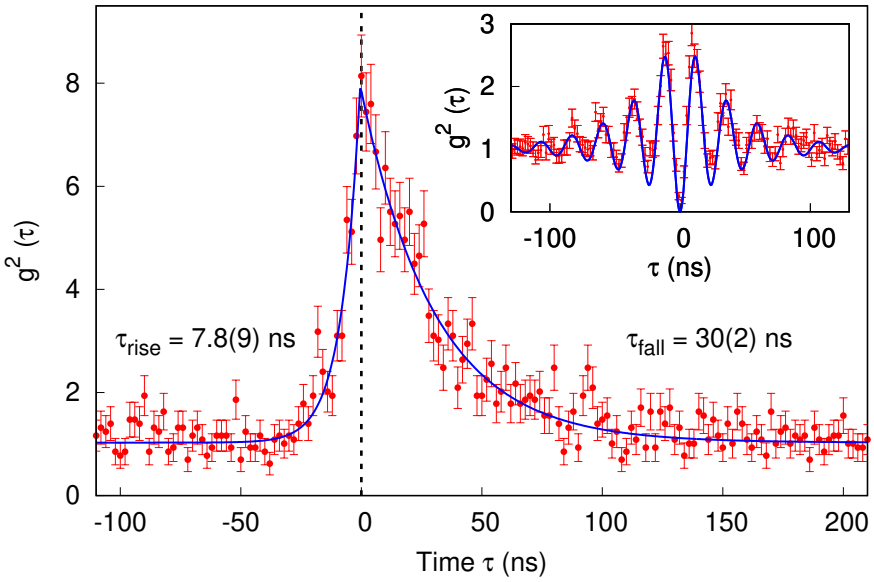

Figure 4.14: Normalized cross-correlation between photons from two opposite Mollow sidebands as a function of delay τ between detection of a photon from the higher energy sideband after detection of a photon from lower energy sideband. Inset: Normalized intensity autocorrelation of the unfiltered off-resonance atomic fluorescence to extract Ω'.

shows a clear bunching behavior around $\tau = 0$. We normalize the correlation function with respect to coincidence counts from a time window that is far from $\tau = 0$. With this, we obtain a bunching value of 8.1(8). The normalized correlation can be fitted by two exponentials, with time constants of $\tau_{\text{rise}} = 7.8(9)\,\text{ns}$ and $\tau_{\text{fall}} = 30(2)\,\text{ns}$, respectively. The theoretical prediction following [101] for τ_{rise} and τ_{fall} are 7.96 ns and 35.02 ns, respectively. The asymmetry of the correlation function indicates that the emission of the sideband photons has a preferred time order for off-resonant excitation, in this case first an emission from the lower energy sideband, followed by a second emission from the higher energy sideband.

Using Eqn. 40 from [101], the theoretically predicted bunching value is 11 for the parameters in our experiment. The discrepancy in our observed value of 8.1 can be attributed to the imperfection in the spectral filtering process. With the separation of 42(1) MHz, cavities with a linewidth of 20 MHz cannot entirely suppress the photons from the central peak and the opposite sideband. Therefore, there are some correlation contributions from different combinations of photons in our experiment, for example between photons from the central peak and photons from two sidebands.

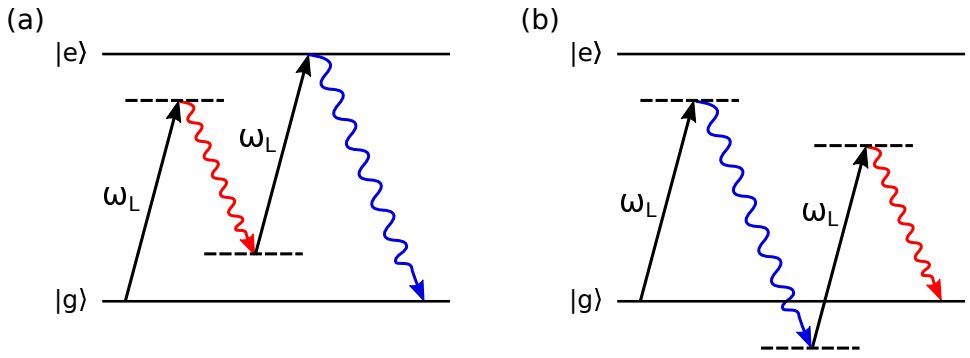

Figure 4.15: Second-order nonlinear scattering processes with red-detuned excitation that result in the emission of photons with frequencies of $2\omega_L - \omega_0$ and ω_0. (a) Emission of photon with frequency $2\omega_L - \omega_0$, followed by emission of photon with frequency ω_0. (b) Reverse order.

These would reduce the expected bunching value.

The preferred order of this emission process can be understood qualitatively through Fig. 4.15. For the red-detuned case, the emission process can happen in two different ways that include the emission of a photon with frequency $2\omega_L - \omega_0$ followed by the photon of frequency ω_0 and the reverse order. In the emission order shown in Fig. 4.15(b), this process does not have an intermediate resonance with the excited state and also involves more virtual states. This causes photon emission in the reverse order to happen at a much lower rate. Thus, the emission is dominated by the process in Fig. 4.15(a) which results in the observation of the asymmetry seen in Fig. 4.14.

4.4 Summary

In this chapter, we described the measurement of the frequency spectrum of resonance fluorescence emitted by an optically trapped atom at different excitation intensities, until the emitter is saturated. The distinctive Mollow triplet was observed, and has been compared to the theoretical model. After taking into account the effect of the cavity transfer function and laser reflection, our results agree with the theoretical prediction very well. For each excitation intensity used in the measurements of the emission spectra, we also record the second-order correlation function of the atomic fluorescence. The Rabi frequency can be extracted by fitting

the $g^{(2)}(\tau)$ obtained from recorded photoevents and this value serves as a benchmark for the results obtained in each measured spectrum. These two measurements also show that we are able to strongly excite the single atom, reaching a saturation parameter of $s \approx 223$.

With the off-resonant excitation, the photons from opposite sidebands have a preferred order of emission, which is manifested in the asymmetry of the correlation around $\tau = 0$. Such a preferred time-ordering of the emitted photons from opposite sidebands could be used to herald narrowband single photons that might find applications in quantum networks using atoms or atom-like systems as stationary nodes.

Chapter 5

Blue-detuned bottle beam dipole trap

In this chapter, we explore the implementation of a reconfigurable blue-detuned optical dipole trap using a spatial light modulator. First, we give a brief overview of the working principle of the blue-detuned optical dipole trap. Next, we construct the bottle beam trap in a test setup to characterize and compare the beam profile with the simulation result. We implement the trap into the setup to trap a single atom. In order to characterize the performance of the bottle beam trap, several measurements have been done including the lifetime and coherence of the single atom in the blue-detuned trap. This work is still in progress and more effort is needed to make the trap work reliably. With a spatial light modulator, it is possible to reconfigure and scale up the trap to form an atomic array.

5.1 Introduction

Optical tweezers are versatile tool that offers the capability to prepare, trap and move neutral atoms with ease. However, it is important to keep in mind that the field that provides the trapping power can have adverse effects such as reduction of the qubit coherence time. Many studies have been conducted to understand how light shifts affect the qubit coherence in various experimental configurations, including strongly focused optical tweezers [66, 82, 133].

In our current setup, we employ a linearly polarized dipole trap that significantly reduces the atomic motion-induced dephasing. However, this linearly polarized trap introduces a tensor light shift that causes state mixing and lowers the light-atom

coupling [46]. We can mitigate this effect by applying a strong magnetic field while keeping the trap depth as low as possible to minimize the tensor light shift.

Instead of finding ways to overcome the side effect of light shifts, we can use a different approach to eliminate the light shift completely by utilizing blue-detuned light. The repulsive nature of blue-detuned light allows for the confinement of the atoms at the intensity minimum region. In the usual trapping potential formed by a red-detuned light, the attractive potential for atoms in the ground state will be repulsive for atoms in the excited state. Especially for atoms in the Rydberg state, light of all wavelengths is 'blue-detuned' to them and will repel the atoms away from the light field. This is because the highly excited valence electron of the Rydberg atom acts almost like a free electron and therefore this results in a negative atomic polarizability. Thus, all the experiments that involve a Rydberg excitation need to switch off the red-detuned trap during the excitation window to avoid atom loss. By choosing a proper wavelength where the atomic polarizability is the same for both the ground and excited states, we can create a trapping potential that is unchanged for atoms in the two states.

5.2 Theoretical Background

In this section, we will briefly introduce the working principle of the optical dipole trap following the standard treatment in [134].

5.2.1 Interaction between dipole with external electric field

Consider the situation where an atom is placed within a laser field, the electric field $\mathbf{E}$ will cause separation of charge in the atom, which makes the neutral atom acts like a dipole. In this case, it becomes a standard problem in electrodynamics where a dipole interacts with an external electric field. The electric field that oscillates at angular frequency ω is given by

$$\mathbf{E}(t) = \hat{\epsilon}E(e^{-i\omega t} + e^{i\omega t}). \tag{5.1}$$

Here, E is the field amplitude and $\hat{\epsilon}$ is the unit polarization vector of the field. While the dipole moment $\mathbf{p}$ of the induced atomic dipole can be written as

$$\begin{aligned}\mathbf{p}(t) &= \alpha \mathbf{E}(t) \\ &= \hat{\epsilon} p (e^{-i\omega t} + e^{i\omega t}),\end{aligned} \tag{5.2}$$

where the amplitude of the dipole moment, p is equal to αE and α is the atomic polarizability that depends on the driving frequency ω.

The potential of the dipole is given by the time-averaged product of the dipole moment and the external field

$$\begin{aligned}U_{dip} &= -\frac{1}{2} \langle \mathbf{pE} \rangle \\ &= -\frac{1}{2\epsilon_0 c} \mathrm{Re}(\alpha) I,\end{aligned} \tag{5.3}$$

where $I = 2\epsilon_0 c |E|^2$ is the intensity of the field. By taking the gradient of the potential, we can obtain the dipole force that acts on the atom

$$\begin{aligned}\mathbf{F}_{dip}(\mathbf{r}) &= -\nabla U_{dip}(\mathbf{r}) \\ &= \frac{1}{2\epsilon_0 c} \mathrm{Re}(\alpha) \nabla I(\mathbf{r}).\end{aligned} \tag{5.4}$$

We can see that the atom will feel a dipole force proportional to the laser's intensity gradient.

5.2.2 Atomic polarizability

To understand the effect of this force on the atom, we first need to figure out the value of the atomic polarizability α. Using Lorentz's model for a classical oscillator, we get the equation of motion for an electron of mass m_e and charge $-e$ to be

$$\ddot{x} + \Gamma_\omega \dot{x} + \omega_0^2 x = -\frac{eE(t)}{m_e}, \tag{5.5}$$

where $\Gamma_\omega = \dfrac{e^2 \omega^2}{6\pi\epsilon_0 m_e c^3}$ is the damping rate when the classical charged oscillator radiated. By integrating Eqn. 5.5, the polarizability is calculated to be

$$\alpha = \frac{e^2}{m_e} \frac{1}{\omega_0^2 - \omega^2 - i\omega\Gamma_\omega}. \tag{5.6}$$

Here we substitute Γ_ω into Eqn. 5.6,

$$\alpha = 6\pi\epsilon_0 c^3 \frac{\Gamma/\omega_0^2}{\omega_0^2 - \omega^2 - i(\omega^3/\omega_0^2)\Gamma}, \tag{5.7}$$

where we define the on-resonance damping rate $\Gamma = (\omega_0/\omega)^2\Gamma_\omega$.

In the semi-classical model described in Section 4.2.1, this damping rate corresponds to the excited state decay rate and is determined by the dipole matrix element:

$$\Gamma = \frac{\omega_0^3}{3\pi\epsilon_0\hbar c^3}|\langle g|\mathbf{d}|e\rangle|^2. \tag{5.8}$$

5.2.3 Dipole potential

With result from Eqn. 5.7, the dipole potential can be written as

$$U_{dip}(\mathbf{r}) = -\frac{3\pi c^2}{2\omega_0^3}\left(\frac{\Gamma}{\omega_0-\omega}+\frac{\Gamma}{\omega_0+\omega}\right)I(\mathbf{r}). \tag{5.9}$$

Through the same treatment in Section 4.2.1 where we assume rotating wave approximation and small detuning ($|\Delta| \ll \omega_0$), now the dipole potential is simplified to

$$U_{dip}(\mathbf{r}) = \frac{3\pi c^2}{2\omega_0^3}\frac{\Gamma}{\Delta}I(\mathbf{r}). \tag{5.10}$$

From this result, we can see that the atom will experience a potential given by the distribution of the laser intensity. If the laser is red-detuned with respect to the atomic resonance ($\Delta < 0$), the negative potential will attract atoms to the intensity maximum point of the laser. This kind of dipole trap can be easily set up by strongly focusing a Gaussian beam to create an intensity maximum at the focal point.

A red-detuned dipole trap is sufficient for most applications that do not saturate the atoms too much. For the same red-detuned light, the polarizability of the excited state is negative, which results in a positive potential for atoms in the excited state. When the atoms are strongly saturated, half of the atomic population will experience a repulsive potential that pushes them away from the trap. As such, even for a "red-detuned" trap, one needs to calculate the atomic polarizability for the state the atom is in to know the effect of the trap potential.

In some highly excited states such as the Rydberg states, the valence electron acts more like a free electron which results in the polarizability of free electron $\alpha = -\frac{e^2}{m_e\omega^2}$ [135]. Given that the polarizability is always negative, the atom that is excited to the Rydberg state will experience a repulsive potential regardless of the wavelength of the trapping laser. In an experiment that involves Rydberg excitation,

the red-detuned dipole trap will be turned off temporarily such that the atom will not get kicked away from the trap.

Other than the trapping potential, one also needs to take into account the photon scattering rate Γ_{sc}, which is given as

$$\Gamma_{\text{sc}} = \frac{1}{\hbar\epsilon_0 c}\text{Im}(\alpha)I. \tag{5.11}$$

The scattering rate is crucial because it affects the heating rate of the atom in the trap and we wish to keep it as low as possible. Using the same procedure to derive Eqn. 5.9, the scattering rate can be simplified to

$$\Gamma_{\text{sc}} = \frac{3\pi c^2}{2\hbar\omega_0^3}\left(\frac{\Gamma}{\Delta}\right)^2 I. \tag{5.12}$$

From Eqn. 5.10 and Eqn. 5.12, we notice that the potential scales with I/Δ while the scattering rate scales with I/Δ^2. As such, the optical dipole traps usually operate at very large detunings and high intensities in order to minimize the scattering while maintaining a certain potential depth. In our setup, we use a wavelength of 851 nm for the red-detuned dipole trap which is 25 THz and 32 THz detuned from the D1 and D2 lines of ^{87}Rb, respectively. With the large detuning, we manage to achieve a trap depth of a few mK through strong focusing of the red-detuned trapping laser.

5.2.4 Blue-Detuned Dipole Trap

Things get a little bit more complicated when the atoms spend most of their time in the excited state. In a red-detuned dipole trap, the state-dependent potential might interfere with the experiment by heating up the atoms or causing state decoherence. On the other hand, blue-detuned light will be repulsive for atoms in both their ground and excited state. Of course, the blue-detuned light here refers to light with a frequency higher than the nearby atomic transitions for the state of interest.

This indicates that we could use blue-detuned light to create a dipole trap that will maintain a similar potential for atoms in different states. Due to the repulsive nature of the blue-detuned light, we need to consider the geometry of the blue-detuned trap. Intuitively, we will need an intensity minimum region that is surrounded by blue-detuned light to confine the atoms. In contrast to the red-

detuned case, a zero-order Gaussian beam that is strongly focused will not work as the intensity minimum simply does not exist.

However, there are various ideas to realize the blue-detuned trap experimentally, such as the light-sheet trap and hollow-beam trap. For the light-sheet trap, the laser is focused elliptically to form a sheet of light which can be used as an optical wall to confine the atom. These light sheets are combined to form a V-shaped cross-section potential where gravity aid in the vertical confinement by pushing the atoms to the bottom of the potential [136, 137]. While the geometry of zero order Gaussian beam does not fulfill the condition to form a blue-detuned trap, the higher order Laguerre-Gaussian beam in $LG_{0,l}$ mode with $l \geq 1$ can provide spatial confinement in the radial direction. As the center of the beam is hollow along the propagation direction, there is no barrier to prevent the atoms from moving along the longitudinal direction. Thus, a pair of plugging beams is applied perpendicularly to the hollow beam to provide longitudinal confinement [138].

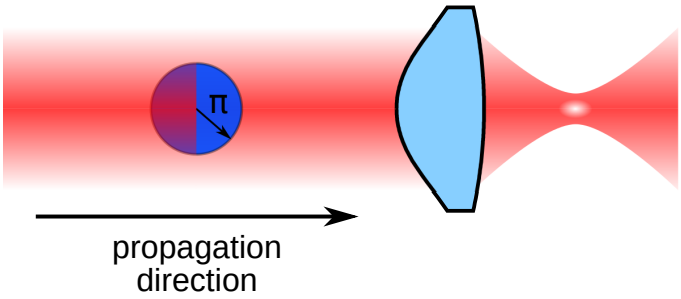

Figure 5.1: Schematic of generation of bottle beam trap with a Gaussian beam passing through a phase plate with circular π phase shift in the central part of the beam. When such a beam is focused down by a lens, the outer and inner regions will interfere destructively due to the phase shift which results in an intensity minimum region surrounded by light.

The two methods described above require multiple beams to form a working trap geometry, which makes it more challenging to maintain a stable potential due to the relative movement of the laser beams. Ozeri et al. [139] demonstrated a variation of a hollow-beam trap, where only one laser beam is needed to create a trapping potential that can provide confinement in all directions. First, a circular π phase shift is applied to the center part of a collimated Gaussian beam. When such a beam is focused down by a lens, the phase shift between the outer and inner regions

will interfere destructively, which results in a dark zone surrounded by light. The dipole trap with this kind of intensity profile is known as a bottle beam trap. A bottle beam trap can be generated in several other experimental configurations, such as Gaussian interference [140, 141], crossed vortex beam [142, 143], and rotating dipole trap [144].

In our implementation, we will focus on the method that applies a π phase shift to the central area of the laser beam [139, 145, 146].

5.3 Numerical Simulation of the beam profile

Before we dive right into the implementation part, we numerically simulate the trap profile to investigate the factor that affects the trapping performance. We adapt the method in [147] to calculate the field near the focal plane by using Green theorem.

Consider a closed surface S' that encloses a given point $\vec{r}$. The electric field at this point can be computed by [148]

$$\begin{aligned}\vec{E}(\vec{r}) = \oint_{S'} \mathrm{d}A' \{ \mathrm{i}kc[\vec{n}' \times \vec{B}(\vec{r}')]G(\vec{r},\vec{r}') + \\ [\vec{n}' \times \vec{E}(\vec{r}')] \times \nabla' G(\vec{r},\vec{r}') + [\vec{n}' \cdot \vec{E}(\vec{r}')]\nabla' G(\vec{r},\vec{r}') \},\end{aligned} \tag{5.13}$$

where $\vec{E}(\vec{r}')$ and $\vec{B}(\vec{r}')$ is the electric and magnetic fields on point $\vec{r}'$ on the closed surface S'. Here, $\vec{n}'$ is the unit vector normal to the closed surface S' and is always pointing inward. The Green function $G(\vec{r},\vec{r}')$ is given by

$$G(\vec{r},\vec{r}') = \frac{e^{\mathrm{i}k|\vec{r}-\vec{r}'|}}{4\pi|\vec{r}-\vec{r}'|}. \tag{5.14}$$

In the far field limit where the distance of point $\vec{r}$ from the closed surface is much larger than the wavelength of the field ($|\vec{r}-\vec{r}'| \gg \lambda$), Eqn. 5.13 becomes

$$\begin{aligned}\vec{E}(\vec{r}) = -2\mathrm{i} \int_{S_{\mathrm{bf}}} \mathrm{d}A' [\vec{n}' \cdot \vec{k}'] \vec{E}(\vec{r}') G(\vec{r},\vec{r}') \\ + 2\mathrm{i} \int_{S_{\mathrm{af}}} \mathrm{d}A' [\vec{n}' \cdot \vec{E}(\vec{r}')] \vec{k}' G(\vec{r},\vec{r}'),\end{aligned} \tag{5.15}$$

where $\vec{k}'$ is the wave vector of the field on the closed surface. We split the surface S' into surface S_{bf} before the focal plane and surface S_{af} after the focal plane as shown in Fig. 5.2. For S_{bf}, we choose an infinitely large plane surface that coincides with

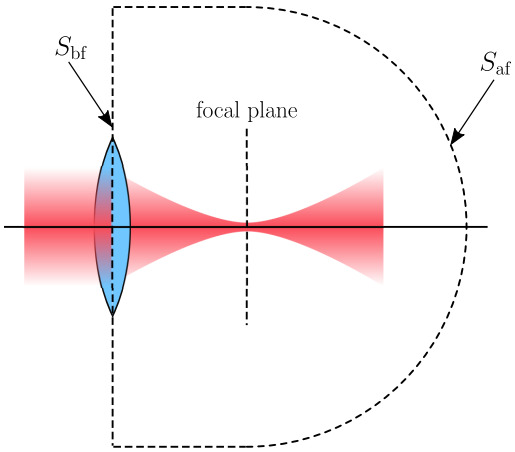

Figure 5.2: The choice of closed surface to simplify Eqn. 5.15.

the ideal lens. Hence, the electric field in the first term in Eqn. 5.15 is the laser field directly after the lens. While for S_{af}, we can choose it to be a hemisphere with an infinitely large radius centered at the focus of the lens. This choice will make the second term in Eqn. 5.15 vanish as $\vec{n}' \cdot \vec{E}(\vec{r}')$ is zero at all points on S_{af}. With this, we can key in the equation and related parameters into a Python program and compute the resulting field profile. To compute the field profile when different phases are applied to the input light, we just add a factor of $e^{i\phi(\vec{r}')}$ to $\vec{E}(\vec{r}')$ where $\phi(\vec{r}')$ is the position-dependent phase shift.

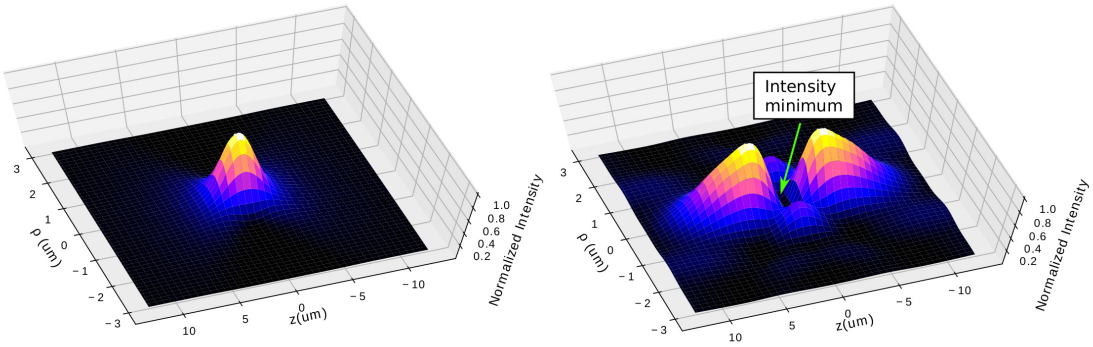

Figure 5.3: Simulation results of the normalized intensity profile of a Gaussian beam focused down by a lens. (Left) Normal Gaussian beam without any phase shift. (Right) Gaussian beam with an additional circular π phase shift in the central region. The intensity minimum region is pointed out with a green arrow. In this simulation, the ratio of the radius of the circular π phase shift to the input beam waist is 0.76.

The simulation results are shown in Fig. 5.3. The intensity profile in Fig. 5.3(left) shows a focused Gaussian beam that can be used as a red-detuned dipole trap where the atoms will be attracted to the intensity maximum region at the focus. In contrast, Fig. 5.3(right) shows the intensity profile of a bottle beam trap when an additional circular π phase shift is applied to the central region of the input Gaussian beam. We can clearly observe a region with minimal intensity.

With this method, we can determine the optimal parameters such as the radius of circular π phase shift to create a bottle beam trap with better performance.

5.3.1 Optimal π phase shift radius

Intuitively, the profile of the bottle beam will vary with different radii of the circular π phase shift that is applied to the central region of the input Gaussian beam. For atom trapping purposes, the intensity at the center of the bottle beam ($z = \rho = 0$) should be as small as possible. It is crucial to figure out the optimal radius of the circular π phase shift that result in a minimum intensity at the center of the bottle beam. With the method in Section 5.3, we can calculate the intensity at the focal point ($z = \rho = 0$) when different radii of the circular π phase shift are applied to the input beam.

In this particular calculation, we are using parameters from the test setup in Section 5.4. The input beam has a beam waist of 0.9 mm, and we use an aspheric lens (Thorlabs AL2520M) with a focal length of 20 mm to focus down the modulated beam to form the bottle beam. Figure 5.4 shows the the intensity at the focal point with respect to different ratios of a to w_0, where we define a as the radius of the circular π phase shift and w_0 is the input beam waist. The value of a/w_0 that results in minimum focal point intensity is 0.832, in agreement with the value obtained in [139, 149].

However, it is worth mentioning that the optimal value for a/w_0 depends on the focusing strength. Here, we define the focusing strength as w_0/f, where f is the focal length of the lens. We perform the same calculation as in Fig. 5.4 with the parameters of our single atom setup to investigate the change in the optimal value of a/w_0. In the actual setup, a beam with 2.71 mm beam waist is focused down with an aspheric lens of the focal length of 5.95 mm to create the bottle beam. With

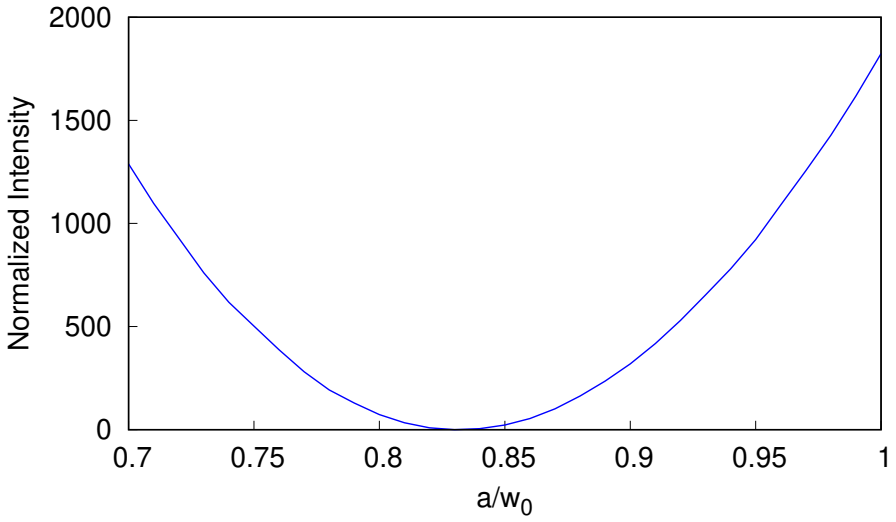

Figure 5.4: The intensity at the center ($z = \rho = 0$) of the bottle beam trap for different ratios of a to w_0, where a is the radius of the circular π phase shift and w_0 is the input beam waist. In this calculation, we are using parameters from the test setup in Section 5.4. The intensity reaches a minimum at $a/w_0 = 0.832$. The intensity here is normalized with respect to the peak intensity of the input Gaussian beam.

these parameters, the optimization result is shown in Fig. 5.5.

We can see that the value of a/w_0 that results in minimum focal point intensity is 0.77. We attribute the discrepancy between the results in Fig. 5.4 and Fig. 5.5 to the breakdown of paraxial approximation under strong focusing. To understand this effect quantitatively, we repeat the simulation for different input beam waists with a constant focal length of 5.95 mm. Through the simulation, the optimal value of a/w_0 at different focusing strengths can be calculated. The result is shown in Fig. 5.6, and we can see the optimal value for a/w_0 decrease for increasing focusing strength.

The expression in [139, 149] assumes paraxial approximation. This approximation is reasonable for the case of longer focal length, where the input beam waist is mainly limited by the aperture of the lens, resulting in smaller focusing strength. As such, the optimal a/w_0 agrees with the expression for the case in the test setup. With smaller focal length, this approximation breaks down very quickly as larger focusing strength can be achieved easily. As such, we will use the optimized value of $a/w_0 = 0.77$ for the experiment in the actual single atom setup.

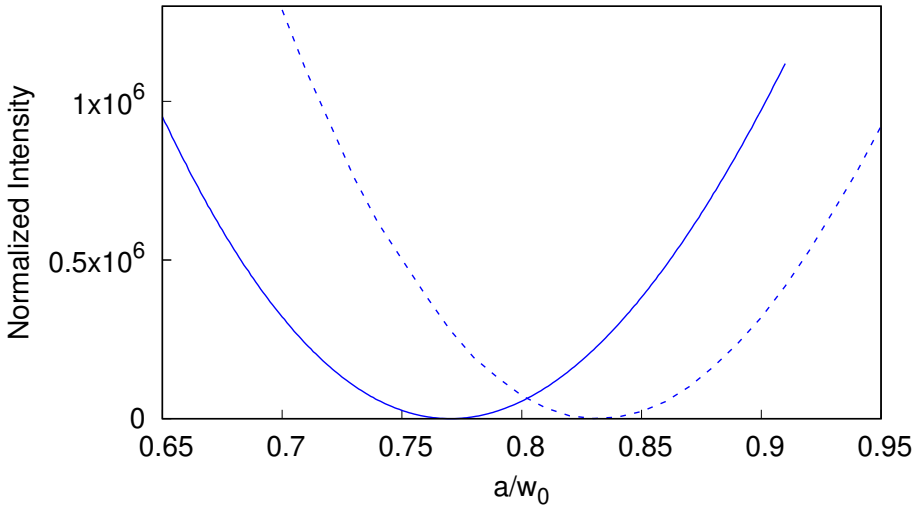

Figure 5.5: Graph of center point intensity versus radius of the circular π phase shift with the parameters of our single atom setup. Here a is the radius of the circular π phase shift and w_0 is the input beam waist. The intensity reaches a minimum at $a/w_0 = 0.77$. The dotted line shows the result in Fig. 5.4 with 1000 times magnification in intensity for visual comparison. The intensity here is normalized with respect to the peak intensity of the input Gaussian beam.

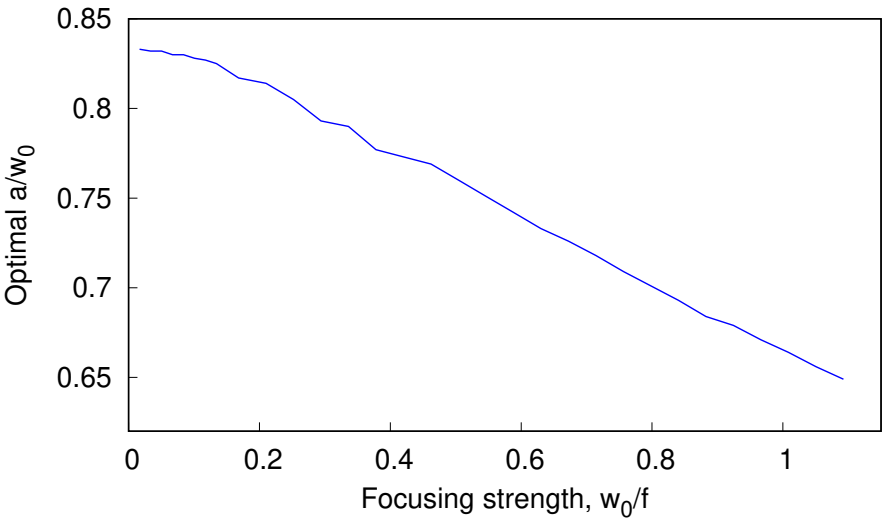

Figure 5.6: The optimal value of a/w_0 at different focusing strength. The focusing strength is defined as the ratio of input beam waist w_0 to focal length f.

5.4 Trap Profile Characterization

Before directly implementing the bottle beam trap in the single-atom setup, we constructed a test setup to characterize the profile of this trap. In this section, we will describe some of the important instruments and present the result of characterization. The experimental setup is shown in Fig. 5.7.

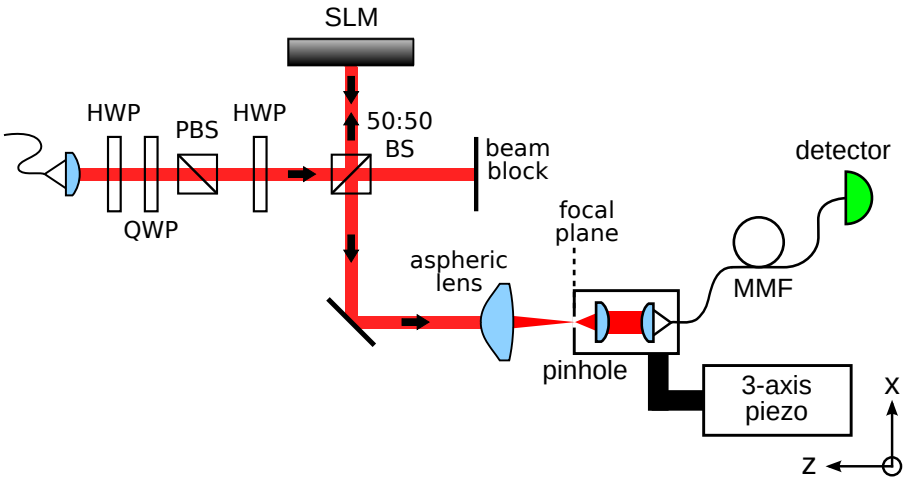

Figure 5.7: Setup to create and characterize profile of a bottle beam. The laser first passes through a combination of wave plates and PBS to align the beam polarization to the SLM crystal axis. The laser is sent head-on to the SLM with a beamsplitter and subsequently focused down by an aspheric lens (Thorlabs AL2520M, f=20 mm). To reconstruct the beam profile, we measure the light that transmits through a 1 μm pinhole. By moving the pinhole and the collection optics with a 3-axis piezo, we can map the beam profile not only on the focal plane but also along the propagation direction. HWP: half-wave plate, QWP: quarter-wave plate, PBS: polarizing beam splitter, BS: beam splitter, MMF: multi-mode fiber.

5.4.1 Spatial Light Modulator

To create the bottle beam trap in our experiment, we choose to use a spatial light modulator (SLM) to apply the desired local phase to the dipole trap laser beam. The SLM employed here is a liquid crystal device that can manipulate the spatial phase of a light field reflected off the device. When a voltage is applied to the anisotropic liquid crystal, its birefringence will change accordingly by re-aligning the liquid crystal molecules. As such, the liquid crystal will imprint a voltage-dependent phase shift to the light field. In our experiment, the SLM is an LCD-based reflection

SLM (P512L) from Meadowlark Optics. It has a spatial resolution of 512×512 pixel with a pitch size of $25\times25\,\mu\text{m}^2$. Each pixel can be individually controlled to modify phase up to more than 2π with 16 bits of voltage resolution. Due to the birefringence property of the liquid crystal, the phase modification only acts on linearly polarized light that is sent horizontally relative to the SLM. Thus, the laser first passes through a PBS to clean up the polarization, and the subsequent HWP is used to adjust the linear polarization with respect to the SLM crystal axis.

There are two common ways to integrate an SLM into an optical setup to perform phase manipulation. The first method is shown in Fig. 5.7 where the laser is sent head-on to the SLM with a beamsplitter (BS). In the case of a 50:50 BS, half of the light will reach SLM, and the modulated light is then split into two beams by the BS again. As such, we collect only a quarter of the total light power.

The second method involves sending the laser beam onto the SLM at a small off-axis angle such that the reflected beam is spatially separated from the input beam. However, the off-axis configuration introduces cross-talk between neighboring pixels as the beam will pass through different pixels along the propagation direction. We also need to take into account the elliptical cross-section of a Gaussian beam impinging on the SLM at an angle and modify the circular π phase shift accordingly. In the actual setup shown in Fig. 5.12, we use the second method to implement the bottle beam trap such that we can retain more laser power in forming the trap.

5.4.2 Measurement and Result

To reconstruct the profile of the beam modulated by the circular π phase shift, we place a $1\,\mu$m pinhole near the focal plane and measure the transmission through it. We attach the pinhole and the collection optics onto a piezo-driven motorized translation stage (P-611.3 NanoCube XYZ Nanopositioner) with a travel range up to $120\,\mu$m in xyz direction. By scanning the pinhole across the focal plane, we can map out the beam profile. We can also repeat this procedure at a different location along the laser propagation axis to investigate how the beam propagates.

Fig. 5.8 shows the side-by-side comparison of the experimentally observed profile and simulation results. A good agreement between the simulation and the experimental data can be seen in the figure. However, the measured trap profile at $z = 60\,\mu$m

and $z = 120\,\mu$m show asymmetry between the two diagonals.

We suspect that the asymmetry arises due to astigmatism in the optical system. To confirm our hypothesis, we measure the intensity profile of the laser before and after the focal plane. The result is shown in Fig. 5.9. The inverted asymmetry shows that the light propagates along the two diagonal planes has a slightly different focus.

To understand the effect of astigmatism on the trap profile, we measured the intensity distribution in the $x' - z$ plane and $y' - z$ plane where we define the diagonals in Fig. 5.8 as x' and y' axis. From Fig. 5.10(a) and (b), we can observe the asymmetry in the trap profile with respect to the focal plane ($z = 0$). Compared to the simulation result (Fig. 5.10(c)), the measured intensity distribution in the $x' - z$ plane (Fig. 5.10(a)) has a v-shape valley that is lower in intensity after the focal plane ($z > 0$). The similar feature appears before the focal plane ($z < 0$) for the measured intensity distribution in the $y' - z$ plane (Fig. 5.10(b). This results in a lower trap potential along the valleys and atoms can escape through these channels. If this problem persists in the single atom setup, we can apply an additional phase

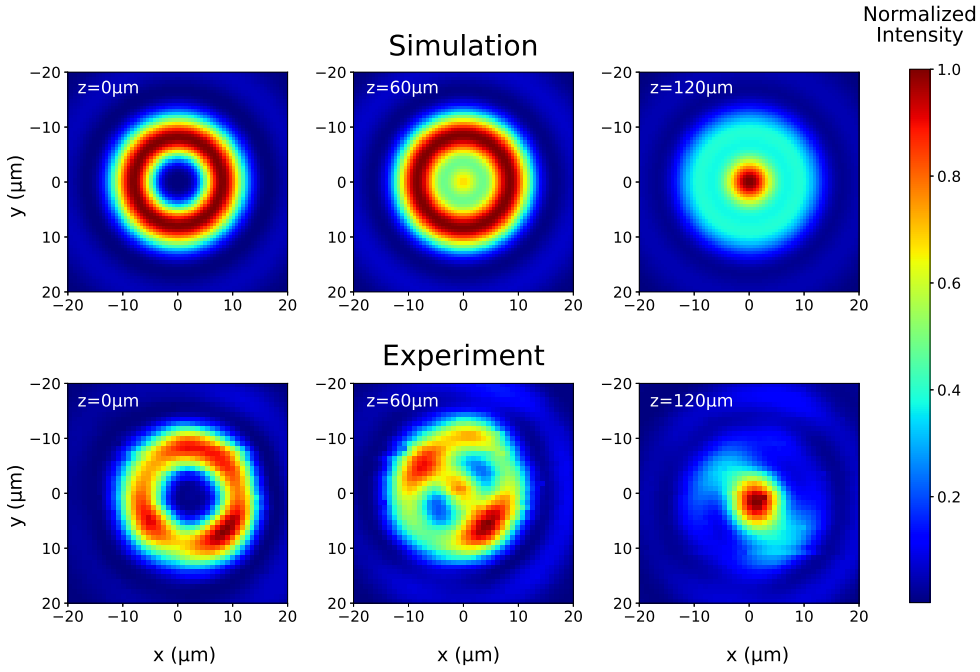

Figure 5.8: Intensity profile of the bottle beam trap at different locations along the beam path. The experimentally observed profile (bottom row) agrees well with the theoretically calculated profile (top row).

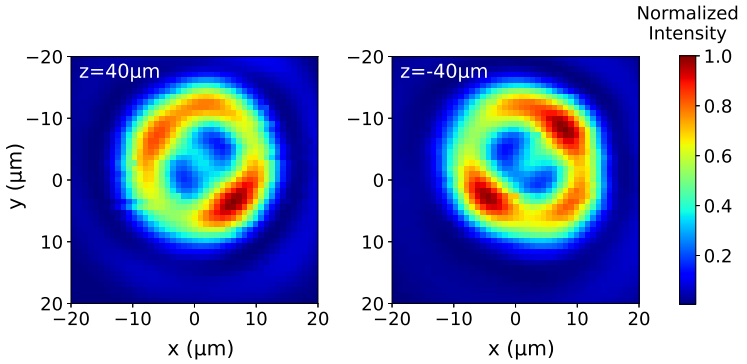

Figure 5.9: Measured intensity profile of the bottle beam trap before ($z = -40\,\mu$m) and after ($z = 40\,\mu$m) the focal plane. Astigmatism shifts the focal plane between the diagonal and anti-diagonal axis.

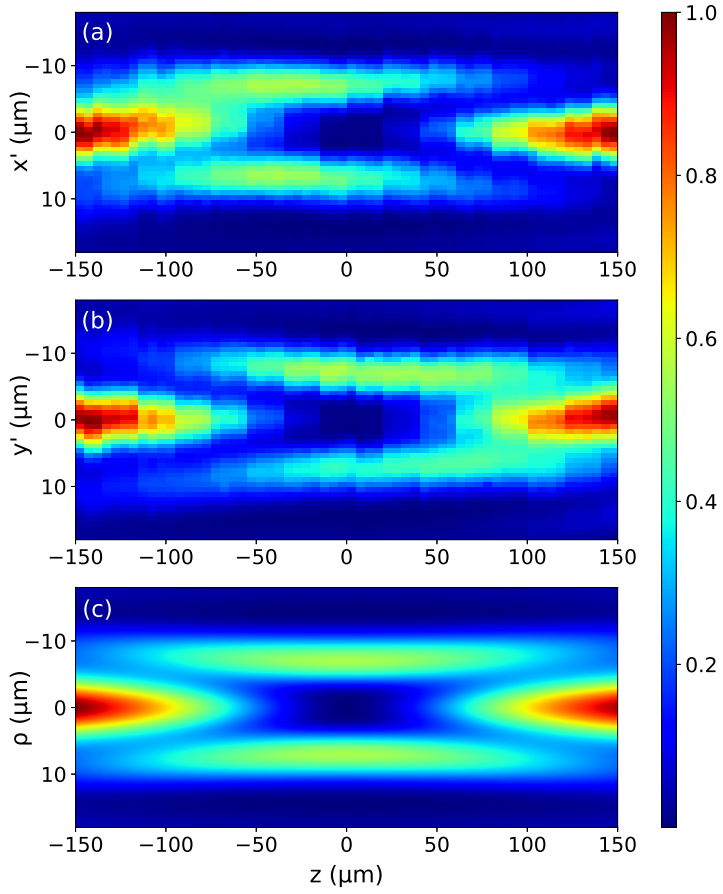

Figure 5.10: Intensity distribution on the (a) $x' - z$ plane and (b) $y' - z$ plane where x'-axis and y'-axis are 45° rotated from the original x-axis and y-axis. (c) Simulation of intensity distribution in $\rho - z$ plane.

on SLM to correct for this aberration.

Next, we also demonstrate the scaling up to multiple dipole traps by uploading different phases to the SLM. In the first column of Fig. 5.11, a grating phase is added on top of the circular π phase shift to split the bottle beam trap into two.

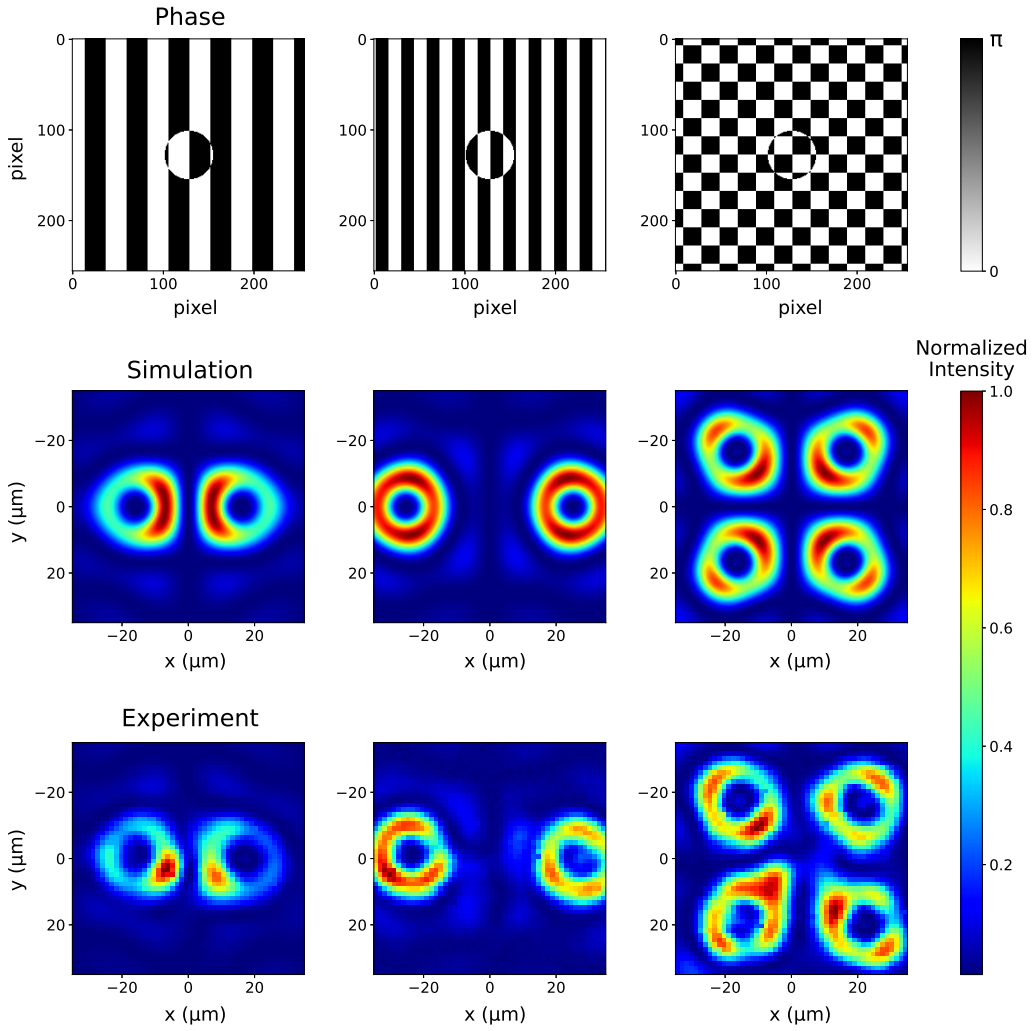

Figure 5.11: Generation of multi bottle beam trap using SLM. The top row shows the input phase onto the SLM while the second and third rows show the simulated and experimental measured intensity profile resulting from the corresponding phase. On top of the circular π phase shift, a grating phase with alternate columns of zero and π phase shift is added to split the beam into two. The grating period will determine the splitting distance as seen from the first and second columns. With additional grating in the horizontal direction, four bottle beam traps can be created as shown in the last column.

Intuitively in the case of a physical grating, we can control the splitting distance by changing the grating period. As we can see in the second column of Fig. 5.11, smaller grating period results in a larger distance between the two bottle beam traps. With the flexibility offered by the SLM, we apply an additional grating in the horizontal direction which will cause the beam to split vertically. This grid grating phase creates four bottle beam traps as shown in the third column of Fig. 5.11. With more complex phases, implementation of traps with different spatial configurations is possible with the usage of the SLM [30].

5.5 Dipole Trap Performance

In this section, we will present the implementation of the blue-detuned bottle beam trap into the single atom setup. We will characterize the trap properties such as the lifetime and coherence of the single atom within the trap.

5.5.1 Experimental Implementation

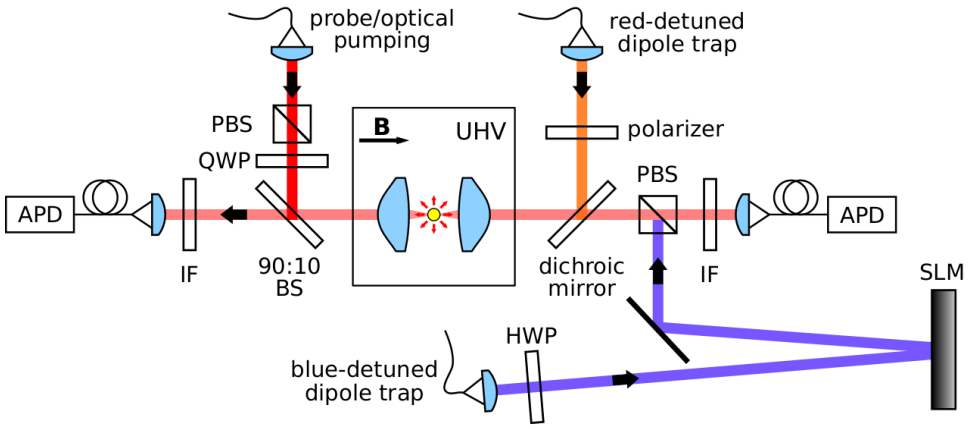

Figure 5.12: Setup for implementing blue-detuned bottle beam trap to trap a single atom. We sent the blue-detuned laser onto the SLM with a small off-axis angle to reduce the side effect of this off-axis configuration. With a PBS, we combine the blue-detuned laser onto the optical axis. The laser passes through the dichroic mirror and is focused down by the aspheric lens to form the bottle beam trap. IF: interference filter centered at 780 nm, HWP: half-wave plate, QWP: quarter-wave plate, PBS: polarizing beam splitter, BS: beam splitter, APD: avalanche photodetector, SLM: spatial light modulator, B: magnetic field.

In the actual setup shown in Fig. 5.12, the blue-detuned laser is collimated

with a triplet fiber collimator from Thorlabs to a beam waist of 2.71 mm. This beam is sent onto the SLM with a small off-axis angle to retain most of the laser power. As discussed in the Section 5.4.1, this leads to cross-talk between neighboring pixels and an elliptical cross-section of the beam impinging on the SLM due to the off-axis angle. To minimize these side effects, we choose a very small off-axis angle of incidence ($\approx 3.2°$). This results in a crosstalk due to an overlap of 0.14 μm to the neighboring pixels given the thickness of the liquid crystal layer is around 2.5 μm. This corresponds to only less than one percent of the 25 μm pixel width. The elliptical cross-section caused by this off-axis angle has a major axis of $w_0 \sec\theta \approx 1.002 w_0$ where w_0 is the Gaussian beam waist. Therefore, we conclude that side effects from off-axis incidence are negligible in our setup.

To minimize the change to our atom trap setup, we inject the blue-detuned laser into the beam along the optical axis with a PBS. This will reduce the collected fluorescence in by half, but transmit almost all power of the linearly polarized trapping laser. This will require a different threshold for detecting the presence of a single atom in the trap and state detection scheme.

As mentioned in Chapter 2, the blue-detuned trap light originates from the same Ti:sapphire laser that used to create the red-detuned dipole trap. We tuned the lasing wavelength from 851 nm to 740 nm, which is blue-detuned with respect to the D_1 and D_2 transitions of ^{87}Rb. A distributed feedback laser lasing at 851 nm is deployed to form a red-detuned dipole trap that replaces the original trap.

We need to estimate the depth of the bottle beam trap to make sure the laser power is sufficient to capture the atom from the MOT. However, for bottle beam trap, the estimation of the trap depth is not so straightforward. For a red-detuned focused-beam trap, the trap depth can be calculated from the maximum intensity at the focal point. In contrast, for the bottle beam trap, the depth of the trap is decided by the saddle point located between the radial and axial intensity maxima, indicated by the red square in Fig. 5.13. For a input laser power of 40 mW and wavelength of 740 nm, the trap depth is estimated to be around $U_0 \simeq k_B \times 3.3\,\mathrm{mK}$ for ^{87}Rb atom. This trap depth is comparable to the red-detuned dipole trap in our current setup. In reality, the trap depth will be lower due to aberration, but we can always compensate that with a higher laser power.

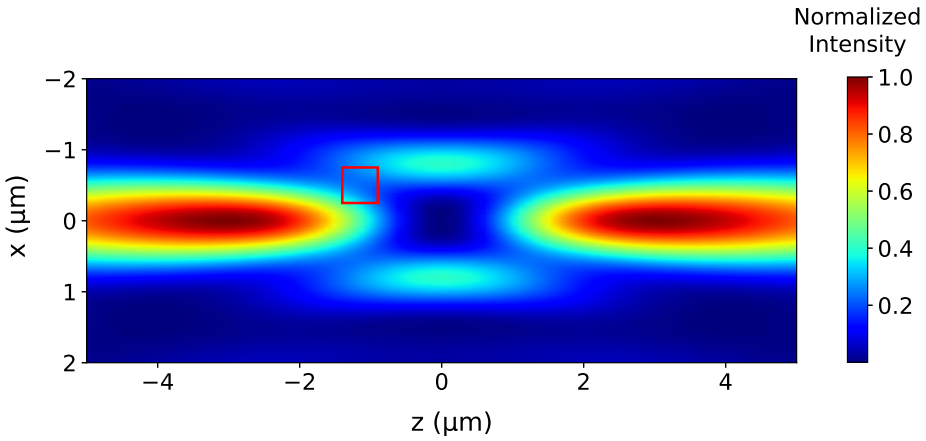

Figure 5.13: Intensity profile of the bottle beam trap along the beam propagation direction. The red square indicates the saddle region between the radial and axial intensity maxima.

5.5.2 Lifetime measurement

After setting up the bottle beam trap, we try the same method to trap a single atom by overlapping the atomic cloud with the focus of the trapping laser. Due to the repulsive nature of the blue-detuned trap, we will not be able to capture a single atom if we repeat the trapping procedure of the red-detuned case where the trapping laser is turned on all the time. Thus, we instead turn on the blue-detuned laser for 20 ms (Fig. 5.14) during the MOT phase and check if a single atom is loaded into the trap by looking at the fluorescence count. We expect a spike in the collected fluorescence if a single atom is trapped. If the loading is unsuccessful, we turn off

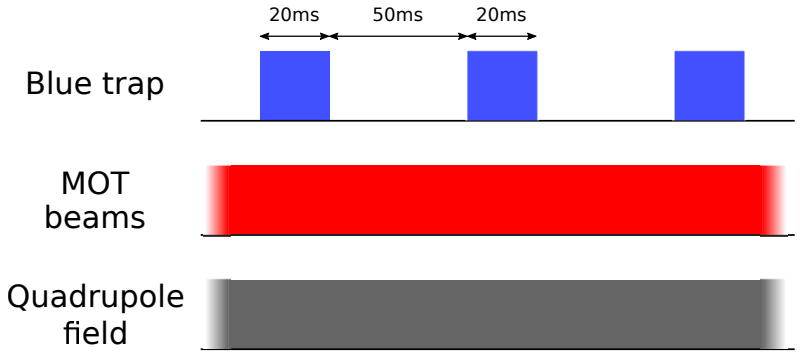

Figure 5.14: Sequence for loading a single atom into the blue-detuned bottle beam trap.

the trapping laser for 50 ms so that the atoms from the MOT can reach the trapping region and turn on the laser again.

However, we did not observe any signal that indicate an atom loading through this process. We think that this might be due to insufficient atomic density in the MOT and the small trapping volume of the bottle beam trap that results in an extremely low loading probability into the intensity minimum region. Further investigations are needed to make direct loading into the bottle beam trap work.

Instead, we try to solve this problem with an indirect approach where we first trap a single atom in a red-detuned dipole trap, and then transfer it to the blue-detuned bottle beam trap. The first part is straightforward. After loading a single atom into the red-detuned trap and cooling it down with PGC, we first turn on the blue-detuned trap and subsequently turn the red-detuned trap off.

With this successful indirect loading into the blue-detuned trap, we measure the lifetime of the single atom in the trap. We hold the atom in the blue-detuned trap for a certain duration and then transfer the atom back to the red-detuned trap to check if the atom survives. We can infer the lifetime of the single atom in the

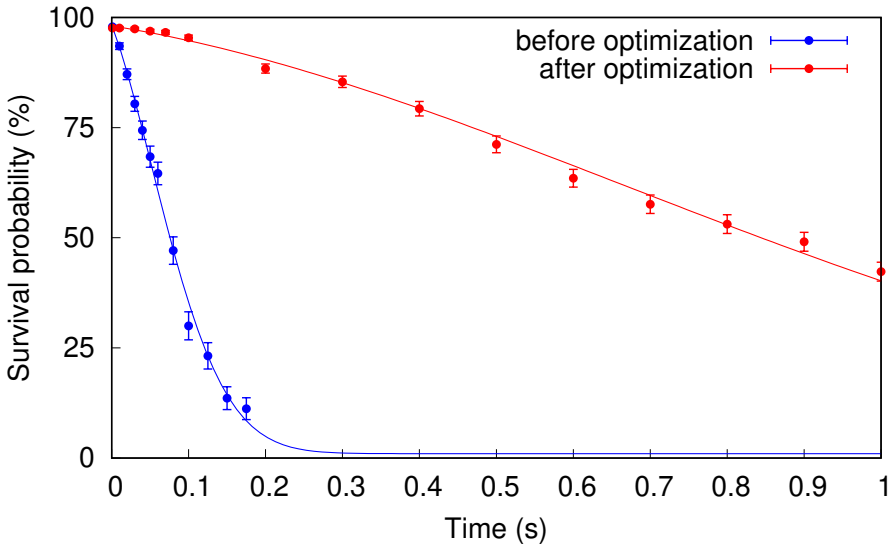

Figure 5.15: Trapping lifetime of single atoms in the blue-detuned dipole trap before (blue) and after (red) optimization of the spatial overlap. The solid lines are Gaussian decay fits that result in a lifetime of 0.133(7) s (blue) and 1.27(8) s (red). Compare to exponential decay, the Gaussian decay profile results in a better fit for the data. The error bars reflect the standard error of binomial statistics.

blue-detuned trap from the survival probabilities at different trapping durations. In Fig. 5.15, the data in blue shows the first measurement done and the lifetime extracted from the fit is 0.133(7) s. This lifetime is lower than expected, given the fact that the scattering from the trapping laser will be minimum at the trapping region. It turns out that the spatial overlap between the two traps is not optimal, which results in a motional heating during the trap transfer process. Utilizing the flexibility offered by the SLM, we can apply phases to the trapping laser to focus, defocus or to steer the beam in both x and y directions. With this, we can control the position of the trap in all three dimensions, and optimize the spatial overlap between the two traps. The red data in Fig. 5.15 show the atom lifetime of 1.27(8) s in the blue-detuned trap after optimization.

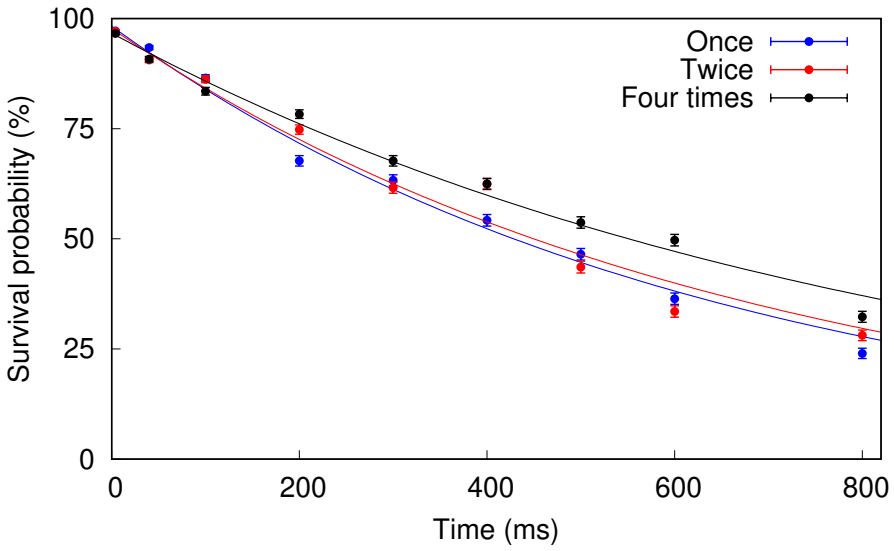

Figure 5.16: Survival probability of the single atom after multiple trap transfers. The data in blue is a control experiment where trap transfer is done once. While the data in red and black are the survival probability of the atoms after going through trap transfer twice and four times. The lifetime here is lower compared to the optimal lifetime in Fig. 5.15 as the measurement is taken on different days.

Although such a lifetime is enough for most of the experiments performed in our setup, it is still shorter than the lifetime in the red-detuned trap by a factor of two. We suspect that the change in potential results in heating in the atomic motion. To confirm our hypothesis, we compare the survival probability of the single atom after experiencing different numbers of trap transfer cycle. The result is

shown in Fig. 5.16. Here, one complete trap transfer cycle refers to the process of which the atom is transferred from the red-detuned trap to the blue-detuned trap, and then back to the red-detuned trap again. Compared to the experimental data where this trap transfer is only done once, the survival probability of the atom after multiple trap transfer cycles does not deviate too much. We deduce a trap transfer probability of around 99% from the red and blue data in Fig. 5.16. This shows that the trap transfer is very efficient and induces minimal heating such that this process does not affect the overall survival probability too much.

To further confirm this conclusion, we investigate the heating quantitatively by measuring the atom temperature. We infer the atom temperature from the release and recapture measurement, where the dipole trap is switched off for a variable duration and the recapture probability of the atom by the trap is measured. We then compare the empirical recapture probability with Monte Carlo simulations to determine the atomic temperature [150]. For atoms in the red-detuned trap, we find an atomic temperature of $15.6(3)\,\mu$K. On the other hand, for the case where the trap transfer is done once, we measured an atomic temperature of $19.4(4)\,\mu$K. This suggests that the trap transfer is not the primary reason for the lower lifetime of atoms within the blue-detuned trap.

Another possible source of heating that result in lower trap lifetime is the scattering of the trap photons by the atom. The result in Fig. 2.6 is taken with a trap depth of $k_B \times 2.8\,\mathrm{mK}$, which correspond to a trap scattering rate of $69.5\,\mathrm{s}^{-1}$. While for the blue-detuned trap, ideally the atom will not scatter any photon if the atom stay at the intensity minimum region. However, there might be residual light intensity at the trapping region due to the imperfection in the process of forming the trap such as aberration. From the measurement in Fig. 5.20, we observed a residual light shift from the blue-detuned trap and can infer a trap scattering rate of $2.7\,\mathrm{s}^{-1}$ from it. This proves that the scattering of the trap photons by the atom in the blue-detuned trap does not induce a serious heating effect onto the atom.

5.5.3 Coherence Characterization

With a reduced light shift experienced by the single atoms, we expect a better coherence with the blue-detuned trap. In this section, we choose to use

the two magnetic-sensitive $5^2S_{1/2}$ Zeeman levels, $|F = 2,\ m_F = -2\rangle \equiv |\uparrow\rangle$ and $|F = 1,\ m_F = -1\rangle \equiv |\downarrow\rangle$ as our qubit states. As such, we can compare the coherence of the single atoms within the blue-detuned trap with the results obtained in Chapter 3, where the single atoms are confined in the red-detuned trap.

Similar to the procedure in Chapter 3, we perform PGC and optical pumping to the atom that has been transferred to the blue-detuned trap. To account for the difference in light shift experienced by the atom in both traps, the laser frequency for PGC and optical pumping is adjusted accordingly.

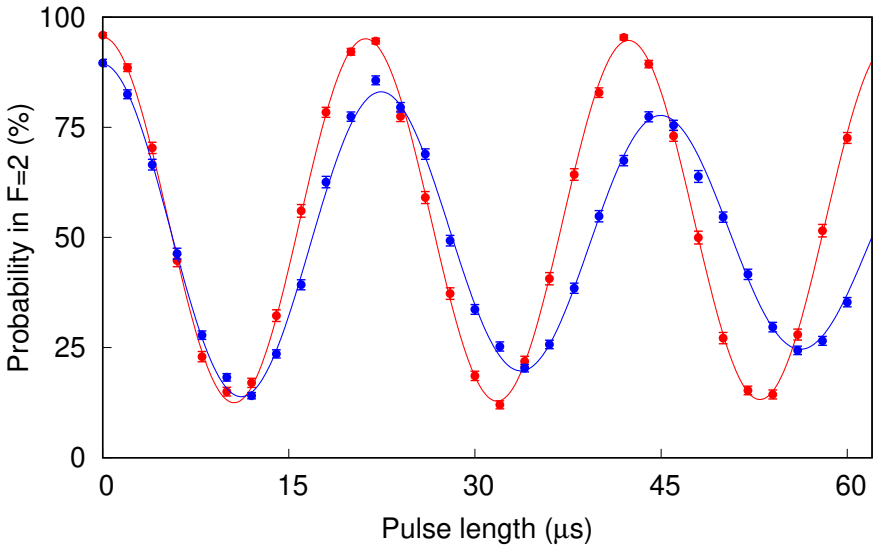

Figure 5.17: Rabi oscillation between $|\uparrow\rangle$ and $|\downarrow\rangle$ states. The data in red and blue show the Rabi oscillations undergone by the atom in the red-detuned trap and blue-detuned trap respectively. The solid line is a fit to an exponentially decaying cosine function to extract the decay time, τ_{Rabi} of the oscillation. In the blue-detune trap, the Rabi oscillation of the single atom shows a decay time, τ_{Rabi} of $127(10)\,\mu$s.

First, we prepare the atom in the $|\uparrow\rangle$ state. After this, we use the microwave field to drive Rabi oscillation between the $|\uparrow\rangle$ and $|\downarrow\rangle$ states. We measure the atomic state after switching on the microwave field for different durations. For comparison purpose, this measurement is done in red and blue-detuned trap, respectively. The result is shown in Fig. 5.17.

We fit the results to an exponentially decaying cosine function to extract both the Rabi frequency Ω_{mw} and the decay time τ_{Rabi} of the Rabi visibility. From the fit, we can obtain a Rabi frequency of $\Omega_{mw} = 2\pi \times 44.40(7)\,\text{kHz}$ and a decay time τ_{Rabi}

of 127(10) μs for case of blue-detuned trap. Compared to the Rabi oscillation in the red-detuned trap, the Rabi visibility within the blue-detuned trap decays at a much faster rate. This indicate that the coherence time of the qubit in the blue-detuned trap might be lower than in the red-detuned trap.

Next, we apply dynamical decoupling sequence to the single atom qubit to investigate the qubit coherence quantitatively. For this experiment, the sequence we choose to apply is the Periodic dynamical decoupling (PDD) sequence used in Section 3.3. With the measured Rabi frequency, we can infer the pulse duration required for a π-pulse is 11.26 μs. The results for $N = 3$ and $N = 5$ are shown in Fig. 5.18 where N is the number of π-pulses in the sequence. We can extract a $1/e$ decay time of 345(32) μs and 440(43) μs for $N = 3$ and $N = 5$ π-pulses, respectively. Compared to the coherence time obtained with PDD sequence in the red-detuned trap (764 μs for $N = 3$ and 1060 μs for $N = 5$ in Section 3.3), there is a significant reduction in the qubit coherence in the bottle beam trap.

From the result in Fig. 5.18, we observe a lower initial population in $|\uparrow\rangle$ due to the reduced Rabi visibility. At zero free evolution time $\tau = 0$, the application of dynamical decoupling sequence is equivalent as the qubit undergoes Rabi oscillation of 6π for $N = 5$ π-pulses. As such, the reduced Rabi visibility results in a initial population of around 76.8% for the case of $N = 5$.

Compared to the coherence evolution of the qubit under Periodic DD in Fig. 3.7, the results in Fig. 5.18 are smoother and do not have any visible recurring dips. In red-detuned trap, the dips in the coherence evolution occur at frequencies that correspond to the axial trap frequency due to the atomic motion in the dipole trap. For the blue-detuned bottle beam trap, we expect an axial trap frequency that is on the same order of magnitude as the radial trap frequency. The decoherence caused by the high frequency atomic motion due to the strong axial and radial confinement is suppressed by the PDD sequence, which results in smooth decay of the qubit coherence evolution.

Currently, the reason for the lower coherence time in the blue-detuned trap is still unclear. As mentioned in Chapter 3, the coherence seems to be mainly limited by fluctuations in magnetic field, causing a change in resonant transition frequency. Theoretically we would expect similar or better coherence performance given that light shift due to dipole light vanishes in the blue-detuned trap. More effort is

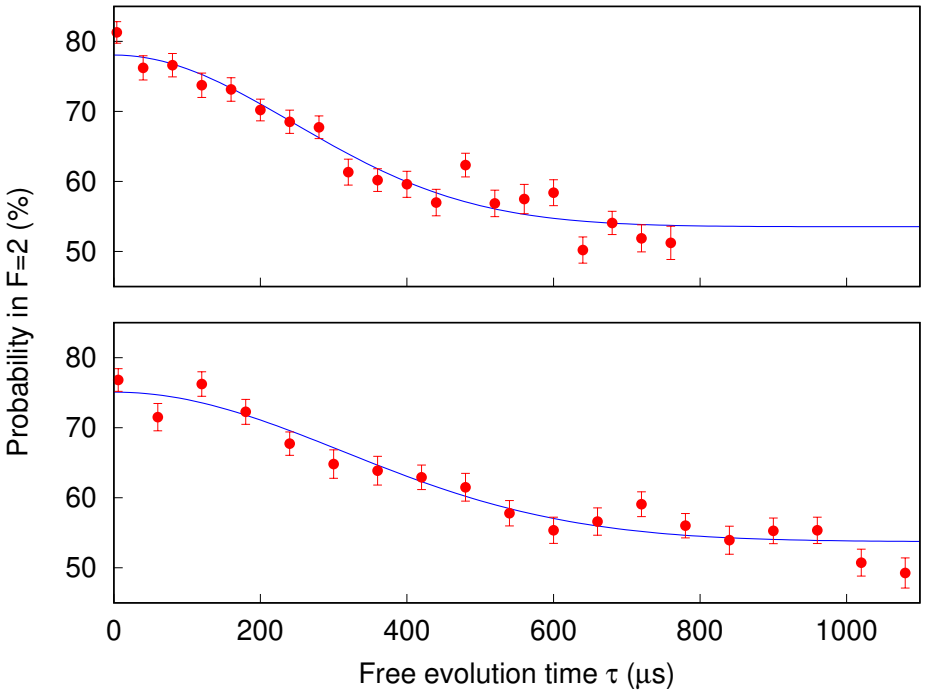

Figure 5.18: Coherence evolution of the stretched state qubit under Periodic DD for $N = 3$ (top) and $N = 5$ (bottom) π-pulses in the blue-detuned trap. The solid lines are fit to a decaying Gaussian to extract their respective $1/e$ decay time. We extend the coherence time to 345(32) μs for $N = 3$ and 440(43) μs for $N = 5$. Error bars represent the standard error of binomial statistics.

needed to investigate the deterioration of the qubit coherence.

5.5.4 Transmission Measurement

Previous works in our group focused on characterizing the coupling efficiency between an optically confined single atom and the strongly focused probe beam. The 36.6(3)% extinction of a weak coherent field by an optically trapped single atom has been demonstrated with a 4Pi configuration [41]. Here the extinction, ϵ is defined as 1-T, where T is the transmission of the probe.

Other than testing the light-atom coupling efficiency in the bottle beam trap, the transmission measurement is done mainly to determine the light shift experienced by the trapped atom. The experimental sequence to characterize the light-atom coupling strength is shown in Fig. 5.19. First, we prepare the atom in $5^2S_{1/2}$ $|F = 2,\ m_F = -2\rangle$ state. In the excitation window, we turn on the probe laser that

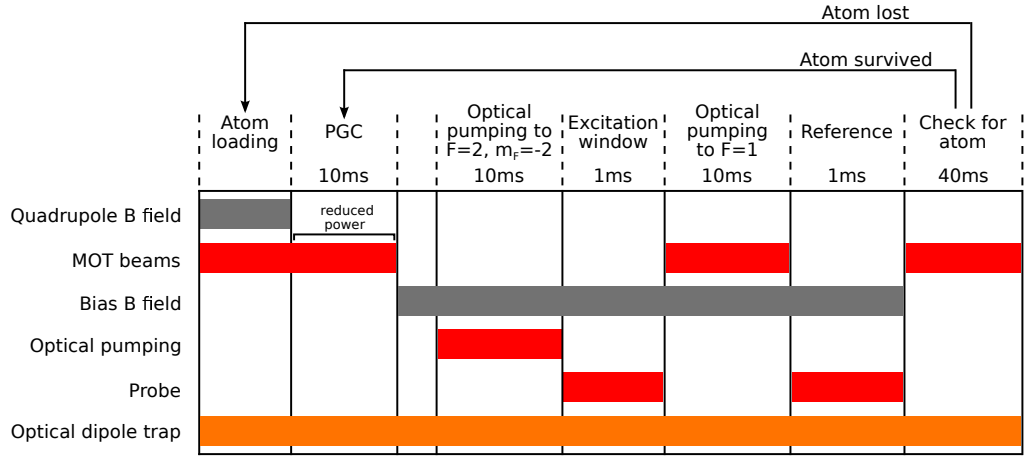

Figure 5.19: Experimental sequence to measure the light-atom coupling efficiency.

drives the closed transition to $5^2P_{3/2}\ |F = 3,\ m_F = -3\rangle$ for 1 ms. After that, we pump the atom to the $F = 1$ state by turning on the MOT cooling beam. This will decouple the atom from the probe beam. Next, we integrate the probe laser for 1 ms when the atom is in the dark state for normalization purpose. By repeating this sequence at different probe frequencies, we can obtain the transmission spectrum shown in Fig. 5.20.

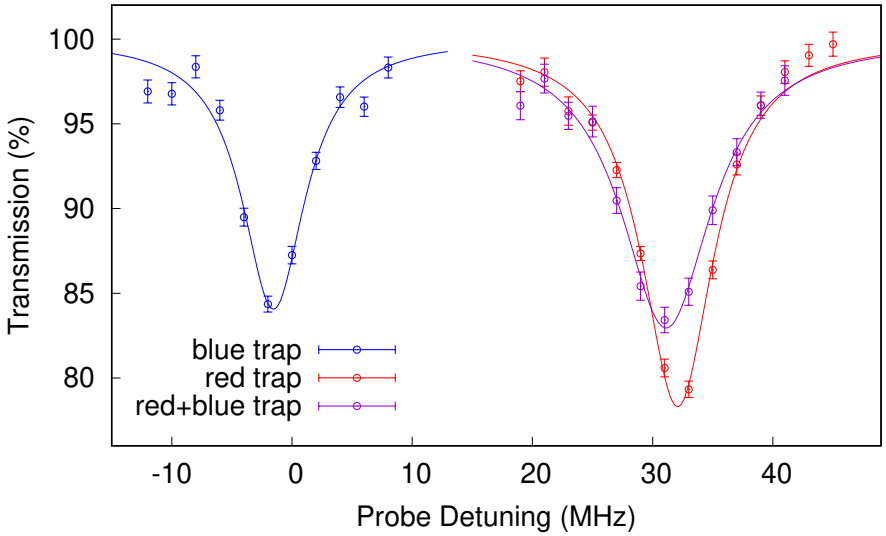

Figure 5.20: Transmission spectrum of a weak coherent probe beam through the single atom confined in different traps. Solid line is a fit to Lorentzian function to extract the resonant frequency and extinction. Error bars represent the standard error of Poissonian statistics.

Within the red-detuned trap, we observe an extinction of $\epsilon_{\text{red}} = 21.7(6)\%$ at detuning $\delta\omega_{\text{red}} = 2\pi \times 32.08(9)\,\text{MHz}$ with respect to the atomic resonance. When we perform the same measurement with both traps on at the same time, we see a small reduction in the extinction ($\epsilon_{\text{red+blue}} = 17.0(6)\%$) with a resonance shift of $\delta\omega_{\text{red+blue}} = 2\pi \times 31.1(2)\,\text{MHz}$. If only blue-detuned trap is on, we record a similar extinction ($\epsilon_{\text{blue}} = 15.9(8)\%$) with a very small resonance shift of $\delta\omega_{\text{blue}} = -2\pi \times 1.5(2)\,\text{MHz}$. From these measurements, we can infer that the blue-detuned trap causes a light-shift of around around 1 MHz to 2 MHz.

In the simulation, we find close to zero light-shift at the intensity minimum point. However, due to the atom movement in the trap, it will experience an effective light-shift which result from averaging the light-shift according to the atom trajectory within the trap. An imperfection in the experimental setup such as aberrations also contribute to this observed light-shift.

5.6 Summary

In this chapter, we have presented the progress towards realizing a blue-detuned bottle beam trap that could be scaled up to form an atomic array. We started by describing the principle of an optical dipole trap, and discussed the effect of light detuning on the trapping potential. By adapting the method in [147], we can numerically simulate the intensity profile of the bottle beam trap. Using the same method, we can also determine the optimal radius for the circular π-phase shift that is used to form the bottle beam trap. In a test setup, we have successfully formed a bottle beam trap using a SLM. The intensity profile of the resulting trap matches well with the simulation result, with some slight asymmetry due to aberration. We also demonstrate the scaling up to multiple dipole traps by applying an additional grating phase on top of the circular π-phase shift. Next, we incorporated the bottle beam trap into our single atom setup and discuss the change in the optimal π-phase shift radius under strong focusing. In the blue-detuned trap, we find a trapping lifetime that is comparable to the case of red-detuned trap. We measure the Rabi oscillation and apply periodic dynamical decoupling sequence to the atom. However, the results show a shorter coherence time and more effort is needed to investigate the reason. In the final part, we perform transmission measurement to probe the light

shift experienced by the atom in the blue-detuned trap. While retaining efficient light-atom coupling, the atom only experiences a light shift of around $1{\sim}2\,\mathrm{MHz}$.

Chapter 6

Conclusion and Future Work

In this thesis, we have presented the characterization of a light-atom interface in free space in terms of its ground state coherence and the spectral properties of the closed optical transition. Utilizing the interaction of the atoms with blue-detuned light, we have realized a light-shift-free trapping geometry that maintains the trapping potential experienced by the atoms across different electronic states.

First, we probe the coherence of the magnetically sensitive Zeeman ground state transition, $|F = 2,\ m_F = -2\rangle \leftrightarrow |F = 1,\ m_F = -1\rangle$. This unusual choice of qubit states is motivated by the existence of the closed optical transition between $5^2S_{1/2}, |F = 2,\ m_F = -2\rangle$ to $5^2P_{3/2}, |F = 3,\ m_F = -3\rangle$, which opens up the possibility to implement some protocols [1–3] that are originally developed for solid-state quantum systems in an atomic system. With such motivation, we have presented a detailed study of the implementation of various dynamical decoupling sequences to extend the coherence time of our qubit system. In the process of comparing the performance of several decoupling sequences such as the Uhrig sequence and Carr–Purcell–Meiboom–Gill sequence, we observe an improvement in the coherence time T_2 by two orders of magnitude from T_2^*. Through a deeper understanding of the applied sequence, we could map out the spectrum of the noise experienced by the qubit by interpreting the decoupling sequence as a noise filter. Finally, optimization on the sequence with 5 π-pulses reveals the ideal sequence for our qubit system, which matches the Carr-Purcell sequence.

Previous efforts in our group mainly focus on interfacing the single atom with a single photon or incoming excitation at the weak field limit for a small saturation parameter $s \ll 1$. An extinction of 36.6(3)% by an optically trapped single atom has

been observed with a 4Pi configuration [41]. Moving on from the investigation on light-atom coupling efficiency, we presented a detailed study on the atomic emission in terms of its spectral properties and photon statistics under different excitation conditions. By exciting a closed transition that resembles an ideal two-level system to the saturation regime, we managed to observe the Mollow triplet in the frequency spectrum of the atomic fluorescence from a single atom. For each experimental setting, we also measure the second-order correlation function of the fluorescence where the Rabi frequency can be extracted. This value serves as a reference to cross-check with the frequency splitting we observed in the measured spectrum. We achieve a Rabi splitting of $2\pi\times64\,\mathrm{MHz}$, which corresponds to a saturation parameter of $s \approx 223$. Under off-resonant excitation, we isolate the photons from opposite sidebands using Fabry-Perot cavities and investigate the correlation of their arrival time. The asymmetry in the $g^{(2)}(\tau)$ reveals the preferred time-ordering of the emitted photons from the different sidebands. Such time-correlated photon pairs with tunable frequency and narrow bandwidth could be used as a heralded single photon source in applications involving atomic systems.

In the last part of this thesis, we explore the possibility to engineer a blue-detuned bottle beam dipole trap by using a spatial light modulator. The flexibility to imprint different spatial phase profiles onto the laser offers us an alternative to scale up the number of traps to form an atomic array. We have successfully characterized the intensity profile of a bottle beam trap. The result agrees well with the simulation. By applying grating phase in both 1D and 2D cases, we show the scaling up to multiple dipole traps in this configuration. We also demonstrate the capability of our bottle beam trap in retaining a single atom with a comparable lifetime to the case of a red-detuned focused-beam trap. However, the coherence within the blue-detuned trap does not show expected behaviour and more investigation is needed in future. In the transmission measurement, the atom confined in the bottle beam trap shows similar efficient light-atom coupling, while experiencing only a light shift of around $1\sim2\,\mathrm{MHz}$. This shows that this approach of realizing an atom-light interface offers us scalability while having a high light-atom interaction strength and similar potential for atom in different electronic states.

Future works could also include the possibility to generate quantum light from our qubit system. As mentioned in Chapter 3, we can apply protocols in [2, 3]

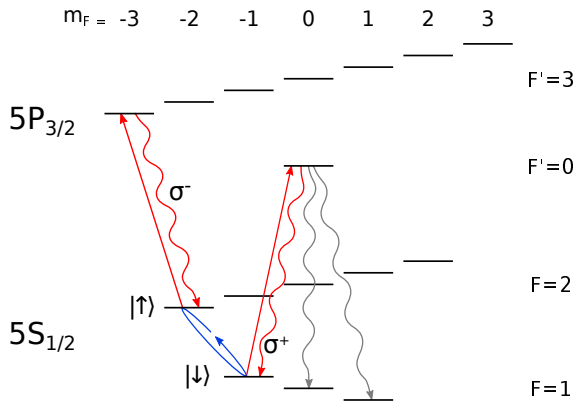

Figure 6.1: Possible level scheme for generation of photonic cluster state. Grey arrows indicate the undesired decay that stop the generation of the cluster state.

that were originally designed for quantum dots to generate entangled photonic strings. One possible way is to replace the two transitions in this proposal with $5S_{1/2}, F = 2,\ m_F = -2 \leftrightarrow 5P_{3/2}, F = 3,\ m_F = -3$ and $5S_{1/2}, F = 1,\ m_F = -1,$ $\leftrightarrow 5P_{3/2}, F = 0,\ m_F = 0$ (Fig. 6.1), where a spin flip can be performed between the two ground state Zeeman levels. Of course complications arise due to the fact that the second transition is not closed and the atom might escape to other levels which halts the generation of a photon chain. While a recent experiment [151] show the generation of entanglement using the correlation of the photons originated from the opposite sidebands of Mollow triplet, it is worth to explore other ways using this correlation as a useful quantum resources.

In order to scale up our system to include more qubits, we also need to upgrade the detector to a camera for higher spatial resolution. In our current setup, we only have the ability to confirm the existence of two atoms in two separate traps. This is done by aiming two single photon detectors at one of the two atoms from both sides of the lenses. With the installation of a camera and additional SLMs for the optical pumping or probe beam, individual site addressing and detection can be achieved.

Appendix A

List of Publications and Conferences

The work presented in this thesis has been published in these articles:

- Coherence of a dynamically decoupled single neutral atom,
  Chang Hoong Chow, **Boon Long Ng**, and Christian Kurtsiefer.
  J. Opt. Soc. Am. B **38**, 621-629 (2021).

- Observation of the Mollow triplet from an optically confined single atom,
  Boon Long Ng, Chang Hoong Chow, and Christian Kurtsiefer.
  Phys. Rev. A **106**, 063719 (2022).

These results have also been presented at the following scientific conferences:

- Coherence of a dynamically decoupled single neutral atom:
  (**Poster**) IPS Meeting 2020, Singapore (2020),
  (**Poster**) 2021 Conference on Lasers and Electro-Optics Europe & European Quantum Electronics Conference (CLEO/Europe-EQEC 2021).

- Observation of the Mollow triplet from an optically confined single atom:
  (**Talk**) IPS Meeting 2022, Singapore (2022),
  (**Poster**) 2023 Conference on Lasers and Electro-Optics Europe & European Quantum Electronics Conference (CLEO/Europe-EQEC 2023), Munich, Germany.

Bibliography

[1]J. P. Lee, B. Villa, A. J. Bennett, R. M. Stevenson, D. J. P. Ellis, I. Farrer, D. A. Ritchie, and A. J. Shields, "A quantum dot as a source of time-bin entangled multi-photon states", Quantum Science and Technology **4**, 025011 (2019).

[2]N. H. Lindner and T. Rudolph, "Proposal for pulsed on-demand sources of photonic cluster state strings", Phys. Rev. Lett. **103**, 113602 (2009).

[3]I. Schwartz, D. Cogan, E. R. Schmidgall, Y. Don, L. Gantz, O. Kenneth, N. H. Lindner, and D. Gershoni, "Deterministic generation of a cluster state of entangled photons", Science **354**, 434–437 (2016).

[4]R. P. Feynman, "Simulating physics with computers", in *Feynman and computation* (CRC Press, 2018), pp. 133–153.

[5]P. W. Shor, "Polynomial-time algorithms for prime factorization and discrete logarithms on a quantum computer", SIAM Journal on Computing **26**, 1484–1509 (1997).

[6]I. L. Chuang, N. Gershenfeld, and M. Kubinec, "Experimental implementation of fast quantum searching", Phys. Rev. Lett. **80**, 3408–3411 (1998).

[7]L. M. K. Vandersypen, M. Steffen, G. Breyta, C. S. Yannoni, M. H. Sherwood, and I. L. Chuang, "Experimental realization of shor's quantum factoring algorithm using nuclear magnetic resonance", Nature **414**, 883–887 (2001).

[8]B. P. Lanyon, T. J. Weinhold, N. K. Langford, M. Barbieri, D. F. V. James, A. Gilchrist, and A. G. White, "Experimental demonstration of a compiled version of shor's algorithm with quantum entanglement", Phys. Rev. Lett. **99**, 250505 (2007).

[9]T. Monz, D. Nigg, E. A. Martinez, M. F. Brandl, P. Schindler, R. Rines, S. X. Wang, I. L. Chuang, and R. Blatt, "Realization of a scalable shor algorithm", Science **351**, 1068–1070 (2016).

[10]C. Figgatt, D. Maslov, K. A. Landsman, N. M. Linke, S. Debnath, and C. Monroe, "Complete 3-qubit grover search on a programmable quantum computer", Nature Communications **8**, 1918 (2017).

[11]H.-J. Briegel, T. Calarco, D. Jaksch, J. I. Cirac, and P. Zoller, "Quantum computing with neutral atoms", Journal of Modern Optics **47**, 415–451 (2000).

[12]L. Isenhower, E. Urban, X. L. Zhang, A. T. Gill, T. Henage, T. A. Johnson, T. G. Walker, and M. Saffman, "Demonstration of a neutral atom controlled-not quantum gate", Phys. Rev. Lett. **104**, 010503 (2010).

[13]Q. A. Turchette, C. J. Hood, W. Lange, H. Mabuchi, and H. J. Kimble, "Measurement of conditional phase shifts for quantum logic", Phys. Rev. Lett. **75**, 4710–4713 (1995).

[14]A. Reiserer and G. Rempe, "Cavity-based quantum networks with single atoms and optical photons", Rev. Mod. Phys. **87**, 1379–1418 (2015).

[15]J. Clarke and F. K. Wilhelm, "Superconducting quantum bits", Nature **453**, 1031–1042 (2008).

[16]M. H. Devoret and R. J. Schoelkopf, "Superconducting circuits for quantum information: an outlook", Science **339**, 1169–1174 (2013).

[17]J. I. Cirac and P. Zoller, "Quantum computations with cold trapped ions", Phys. Rev. Lett. **74**, 4091–4094 (1995).

[18]R. Blatt and D. Wineland, "Entangled states of trapped atomic ions", Nature **453**, 1008–1015 (2008).

[19]I. V. Inlek, C. Crocker, M. Lichtman, K. Sosnova, and C. Monroe, "Multispecies trapped-ion node for quantum networking", Phys. Rev. Lett. **118**, 250502 (2017).

[20]D. Loss and D. P. DiVincenzo, "Quantum computation with quantum dots", Phys. Rev. A **57**, 120–126 (1998).

[21]H.-R. Wei and F.-G. Deng, "Scalable quantum computing based on stationary spin qubits in coupled quantum dots inside double-sided optical microcavities", Scientific Reports **4**, 7551 (2014).

[22]A. Delteil, Z. Sun, W.-b. Gao, E. Togan, S. Faelt, and A. Imamoğlu, "Generation of heralded entanglement between distant hole spins", Nature Physics **12**, 218–223 (2016).

[23]S. Boixo, S. V. Isakov, V. N. Smelyanskiy, R. Babbush, N. Ding, Z. Jiang, M. J. Bremner, J. M. Martinis, and H. Neven, "Characterizing quantum supremacy in near-term devices", Nature Physics **14**, 595–600 (2018).

[24]T. E. Northup and R. Blatt, "Quantum information transfer using photons", Nature Photonics **8**, 356–363 (2014).

[25]J. I. Cirac, P. Zoller, H. J. Kimble, and H. Mabuchi, "Quantum state transfer and entanglement distribution among distant nodes in a quantum network", Phys. Rev. Lett. **78**, 3221–3224 (1997).

[26]H. J. Kimble, "The quantum internet", Nature **453**, 1023–1030 (2008).

[27]W. Rosenfeld, J. Volz, M. Weber, and H. Weinfurter, "Coherence of a qubit stored in zeeman levels of a single optically trapped atom", Phys. Rev. A **84**, 022343 (2011).

[28]C. Junge, D. O'Shea, J. Volz, and A. Rauschenbeutel, "Strong coupling between single atoms and nontransversal photons", Phys. Rev. Lett. **110**, 213604 (2013).

[29]E. Distante, S. Daiss, S. Langenfeld, L. Hartung, P. Thomas, O. Morin, G. Rempe, and S. Welte, "Detecting an itinerant optical photon twice without destroying it", Phys. Rev. Lett. **126**, 253603 (2021).

[30]D. Barredo, V. Lienhard, S. de Léséleuc, T. Lahaye, and A. Browaeys, "Synthetic three-dimensional atomic structures assembled atom by atom", Nature **561**, 79–82 (2018).

[31]H. Bernien, S. Schwartz, A. Keesling, H. Levine, A. Omran, H. Pichler, S. Choi, A. S. Zibrov, M. Endres, M. Greiner, V. Vuletić, and M. D. Lukin, "Probing many-body dynamics on a 51-atom quantum simulator", Nature **551**, 579–584 (2017).

[32]D. Bluvstein, H. Levine, G. Semeghini, T. T. Wang, S. Ebadi, M. Kalinowski, A. Keesling, N. Maskara, H. Pichler, M. Greiner, V. Vuletić, and M. D. Lukin, "A quantum processor based on coherent transport of entangled atom arrays", Nature **604**, 451–456 (2022).

[33]E. Urban, T. A. Johnson, T. Henage, L. Isenhower, D. D. Yavuz, T. G. Walker, and M. Saffman, "Observation of rydberg blockade between two atoms", Nature Physics **5**, 110–114 (2009).

[34]A. Gaëtan, Y. Miroshnychenko, T. Wilk, A. Chotia, M. Viteau, D. Comparat, P. Pillet, A. Browaeys, and P. Grangier, "Observation of collective excitation of two individual atoms in the rydberg blockade regime", Nature Physics **5**, 115–118 (2009).

[35]H. Levine, A. Keesling, A. Omran, H. Bernien, S. Schwartz, A. S. Zibrov, M. Endres, M. Greiner, V. Vuleti ć, and M. D. Lukin, "High-fidelity control and entanglement of rydberg-atom qubits", Phys. Rev. Lett. **121**, 123603 (2018).

[36]H. Levine, A. Keesling, G. Semeghini, A. Omran, T. T. Wang, S. Ebadi, H. Bernien, M. Greiner, V. Vuleti ć, H. Pichler, and M. D. Lukin, "Parallel implementation of high-fidelity multiqubit gates with neutral atoms", Phys. Rev. Lett. **123**, 170503 (2019).

[37]T. M. Graham, M. Kwon, B. Grinkemeyer, Z. Marra, X. Jiang, M. T. Lichtman, Y. Sun, M. Ebert, and M. Saffman, "Rydberg-mediated entanglement in a two-dimensional neutral atom qubit array", Phys. Rev. Lett. **123**, 230501 (2019).

[38]K. Singh, S. Anand, A. Pocklington, J. T. Kemp, and H. Bernien, "Dual-element, two-dimensional atom array with continuous-mode operation", Phys. Rev. X **12**, 011040 (2022).

[39]C. Sheng, J. Hou, X. He, K. Wang, R. Guo, J. Zhuang, B. Mamat, P. Xu, M. Liu, J. Wang, and M. Zhan, "Defect-free arbitrary-geometry assembly of mixed-species atom arrays", Phys. Rev. Lett. **128**, 083202 (2022).

[40]V. Leong, M. A. Seidler, M. Steiner, A. Cerè, and C. Kurtsiefer, "Time-resolved scattering of a single photon by a single atom", Nature Communications **7**, 13716 (2016).

[41]Y.-S. Chin, M. Steiner, and C. Kurtsiefer, "Nonlinear photon-atom coupling with 4pi microscopy", Nature Communications **8**, 1200 (2017).

[42]C. Y. Sum, "Light-atom coupling with 4pi microscopy", PhD thesis (National University of Singapore (Singapore), 2018).

[43]A. Arnold, J. Wilson, and M. Boshier, "A simple extended-cavity diode laser", Review of Scientific Instruments **69**, 1236–1239 (1998).

[44]L. Ricci, M. Weidemüller, T. Esslinger, A. Hemmerich, C. Zimmermann, V. Vuletic, W. König, and T. Hänsch, "A compact grating-stabilized diode laser system for atomic physics", Optics Communications **117**, 541–549 (1995).

[45]Y.-S. Chin, M. Steiner, and C. Kurtsiefer, "Polarization gradient cooling of single atoms in optical dipole traps", Phys. Rev. A **96**, 033406 (2017).

[46]M. Steiner, Y.-S. Chin, and C. Kurtsiefer, "Transmission spectroscopy of a single atom in the presence of tensor light shifts", New J. Phys. **21**, 023012 (2019).

[47]N. Schlosser, G. Reymond, and P. Grangier, "Collisional blockade in microscopic optical dipole traps", Phys. Rev. Lett. **89**, 023005 (2002).

[48]A. Fuhrmanek, R. Bourgain, Y. R. P. Sortais, and A. Browaeys, "Free-space lossless state detection of a single trapped atom", Phys. Rev. Lett. **106**, 133003 (2011).

[49]M. J. Gibbons, C. D. Hamley, C.-Y. Shih, and M. S. Chapman, "Nondestructive fluorescent state detection of single neutral atom qubits", Phys. Rev. Lett. **106**, 133002 (2011).

[50]C. H. Chow, B. L. Ng, and C. Kurtsiefer, "Coherence of a dynamically decoupled single neutral atom", J. Opt. Soc. Am. B **38**, 621–629 (2021).

[51]C. H. Bennett and D. P. DiVincenzo, "Quantum information and computation", Nature **404**, 247–255 (2000).

[52]F. Arute, K. Arya, R. Babbush, D. Bacon, J. C. Bardin, R. Barends, R. Biswas, S. Boixo, F. G. S. L. Brandao, D. A. Buell, B. Burkett, Y. Chen, Z. Chen, B. Chiaro, R. Collins, W. Courtney, A. Dunsworth, E. Farhi, B. Foxen, A. Fowler, C. Gidney, M. Giustina, R. Graff, K. Guerin, S. Habegger, M. P. Harrigan, M. J. Hartmann, A. Ho, M. Hoffmann, T. Huang, T. S. Humble, S. V. Isakov, E. Jeffrey, Z. Jiang, D. Kafri, K. Kechedzhi, J. Kelly, P. V. Klimov, S. Knysh, A. Korotkov, F. Kostritsa, D. Landhuis, M. Lindmark, E. Lucero, D. Lyakh, S. Mandrà, J. R. McClean, M. McEwen, A. Megrant, X. Mi, K. Michielsen, M. Mohseni, J. Mutus, O. Naaman, M. Neeley, C. Neill, M. Y. Niu, E. Ostby, A. Petukhov, J. C. Platt, C. Quintana, E. G. Rieffel, P. Roushan, N. C. Rubin, D. Sank, K. J. Satzinger, V. Smelyanskiy,

K. J. Sung, M. D. Trevithick, A. Vainsencher, B. Villalonga, T. White, Z. J. Yao, P. Yeh, A. Zalcman, H. Neven, and J. M. Martinis, "Quantum supremacy using a programmable superconducting processor", Nature **574**, 505–510 (2019).

[53]W. H. Zurek, "Decoherence, einselection, and the quantum origins of the classical", Rev. Mod. Phys. **75**, 715–775 (2003).

[54]H. G. Krojanski and D. Suter, "Decoherence in large nmr quantum registers", Phys. Rev. A **74**, 062319 (2006).

[55]S. Doronin, E. Fel'dman, and A. Zenchuk, "Numerical analysis of relaxation times of multiple quantum coherences in the system with a large number of spins", The Journal of Chemical Physics **134**, 034102 (2011).

[56]H. Y. Carr and E. M. Purcell, "Effects of diffusion on free precession in nuclear magnetic resonance experiments", Phys. Rev. **94**, 630–638 (1954).

[57]S. Meiboom and D. Gill, "Modified spin-echo method for measuring nuclear relaxation times", Review of Scientific Instruments **29**, 688–691 (1958).

[58]E. L. Hahn, "Spin echoes", Phys. Rev. **80**, 580–594 (1950).

[59]L. M. K. Vandersypen and I. L. Chuang, "Nmr techniques for quantum control and computation", Rev. Mod. Phys. **76**, 1037–1069 (2005).

[60]G. S. Uhrig, "Keeping a quantum bit alive by optimized π-pulse sequences", Phys. Rev. Lett. **98**, 100504 (2007).

[61]M. J. Biercuk, H. Uys, A. P. VanDevender, N. Shiga, W. M. Itano, and J. J. Bollinger, "Optimized dynamical decoupling in a model quantum memory", Nature **458**, 996–1000 (2009).

[62]M. J. Biercuk, A. C. Doherty, and H. Uys, "Dynamical decoupling sequence construction as a filter-design problem", Journal of Physics B: Atomic, Molecular and Optical Physics **44**, 154002 (2011).

[63]G. S. Uhrig, "Exact results on dynamical decoupling by π pulses in quantum information processes", New Journal of Physics **10**, 083024 (2008).

[64]Ł. Cywi ński, R. M. Lutchyn, C. P. Nave, and S. Das Sarma, "How to enhance dephasing time in superconducting qubits", Phys. Rev. B **77**, 174509 (2008).

[65]S. Kuhr, W. Alt, D. Schrader, I. Dotsenko, Y. Miroshnychenko, W. Rosenfeld, M. Khudaverdyan, V. Gomer, A. Rauschenbeutel, and D. Meschede, "Coherence properties and quantum state transportation in an optical conveyor belt", Phys. Rev. Lett. **91**, 213002 (2003).

[66]S. Kuhr, W. Alt, D. Schrader, I. Dotsenko, Y. Miroshnychenko, A. Rauschenbeutel, and D. Meschede, "Analysis of dephasing mechanisms in a standing-wave dipole trap", Phys. Rev. A **72**, 023406 (2005).

[67]M. F. Andersen, A. Kaplan, and N. Davidson, "Echo spectroscopy and quantum stability of trapped atoms", Phys. Rev. Lett. **90**, 023001 (2003).

[68]M. F. Andersen, A. Kaplan, T. Grünzweig, and N. Davidson, "Suppression of dephasing of optically trapped atoms", Phys. Rev. A **70**, 013405 (2004).

[69]D. D. Yavuz, P. B. Kulatunga, E. Urban, T. A. Johnson, N. Proite, T. Henage, T. G. Walker, and M. Saffman, "Fast Ground State Manipulation of Neutral Atoms in Microscopic Optical Traps", Phys. Rev. Lett. **96**, 063001 (2006).

[70]M. P. A. Jones, J. Beugnon, A. Gaëtan, J. Zhang, G. Messin, A. Browaeys, and P. Grangier, "Fast quantum state control of a single trapped neutral atom", Phys. Rev. A **75**, 040301(R) (2007).

[71]J. Yang, X. He, R. Guo, P. Xu, K. Wang, C. Sheng, M. Liu, J. Wang, A. Derevianko, and M. Zhan, "Coherence preservation of a single neutral atom qubit transferred between magic-intensity optical traps", Phys. Rev. Lett. **117**, 123201 (2016).

[72]G. Afek, J. Coslovsky, A. Mil, and N. Davidson, "Revival of raman coherence of trapped atoms", Physical Review A **96**, 043831 (2017).

[73]S. B. Markussen, J. Appel, C. Østfeldt, J.-B. S. Béguin, E. S. Polzik, and J. H. Müller, "Measurement and simulation of atomic motion in nanoscale optical trapping potentials", Applied Physics B: Lasers and Optics **126**, 73 (2020).

[74]C. A. Ryan, J. S. Hodges, and D. G. Cory, "Robust decoupling techniques to extend quantum coherence in diamond", Phys. Rev. Lett. **105**, 200402 (2010).

[75]D. D. Sukachev, A. Sipahigil, C. T. Nguyen, M. K. Bhaskar, R. E. Evans, F. Jelezko, and M. D. Lukin, "Silicon-vacancy spin qubit in diamond: a quantum memory exceeding 10 ms with single-shot state readout", Phys. Rev. Lett. **119**, 223602 (2017).

[76]D. J. Szwer, S. C. Webster, A. M. Steane, and D. M. Lucas, "Keeping a single qubit alive by experimental dynamic decoupling", J. Phys. B **44**, 025501 (2010).

[77]M. A. A. Ahmed, G. A. Álvarez, and D. Suter, "Robustness of dynamical decoupling sequences", Physical Review A **87**, 042309 (2013).

[78]M. Hirose, C. D. Aiello, and P. Cappellaro, "Continuous dynamical decoupling magnetometry", Phys. Rev. A **86**, 062320 (2012).

[79]I. Baumgart, J.-M. Cai, A. Retzker, M. B. Plenio, and C. Wunderlich, "Ultrasensitive magnetometer using a single atom", Phys. Rev. Lett. **116**, 240801 (2016).

[80]J. Bylander, S. Gustavsson, F. Yan, F. Yoshihara, K. Harrabi, G. Fitch, D. G. Cory, Y. Nakamura, J. S. Tsai, and W. D. Oliver, "Noise spectroscopy through dynamical decoupling with a superconducting flux qubit", Nat. Phys. **7**, 565–570 (2011).

[81]S. Hernández-Gómez, F. Poggiali, P. Cappellaro, and N. Fabbri, "Noise spectroscopy of a quantum-classical environment with a diamond qubit", Phys. Rev. B **98**, 214307 (2018).

[82]J. D. Thompson, T. G. Tiecke, A. S. Zibrov, V. Vuleti ć, and M. D. Lukin, "Coherence and raman sideband cooling of a single atom in an optical tweezer", Phys. Rev. Lett. **110**, 133001 (2013).

[83]C. P. Slichter, "Principles of magnetic resonance", (Springer Berlin Heidelberg, 1990).

[84]T. Gullion, D. B. Baker, and M. S. Conradi, "New, compensated carr-purcell sequences", Journal of Magnetic Resonance (1969) **89**, 479–484 (1990).

[85]A. Ajoy, G. A. Álvarez, and D. Suter, "Optimal pulse spacing for dynamical decoupling in the presence of a purely dephasing spin bath", Physical Review A **83**, 032303 (2011).

[86]K. Khodjasteh and D. A. Lidar, "Fault-tolerant quantum dynamical decoupling", Physical Review Letters **95**, 180501 (2005).

[87]D. Farfurnik, A. Jarmola, L. M. Pham, Z.-H. Wang, V. V. Dobrovitski, R. L. Walsworth, D. Budker, and N. Bar-Gill, "Optimizing a dynamical decoupling protocol for solid-state electronic spin ensembles in diamond", Physical Review B **92**, 060301 (2015).

[88]L. Childress, J. M. Taylor, A. S. Sørensen, and M. D. Lukin, "Fault-tolerant quantum communication based on solid-state photon emitters", Phys. Rev. Lett. **96**, 070504 (2006).

[89]M. Razavi, M. Piani, and N. Lütkenhaus, "Quantum repeaters with imperfect memories: cost and scalability", Phys. Rev. A **80**, 032301 (2009).

[90]B. L. Ng, C. H. Chow, and C. Kurtsiefer, "Observation of the mollow triplet from an optically confined single atom", Phys. Rev. A **106**, 063719 (2022).

[91]H. Walther, "Resonance fluorescence of two-level atoms", in *Advances in atomic, molecular, and optical physics*, Vol. 51 (Academic Press, Jan. 2005), pp. 239–272.

[92]V. Weisskopf and E. Wigner, "Berechnung der natürlichen linienbreite auf grund der diracschen lichttheorie", Zeitschrift für Physik **63**, 54–73 (1930).

[93]H. Gibbs and T. Venkatesan, "Direct observation of fluorescence narrower than the natural linewidth", Optics Communications **17**, 87–90 (1976).

[94]J. T. Höffges, H. W. Baldauf, W. Lange, and H. Walther, "Heterodyne measurement of the resonance fluorescence of a single ion", Journal of Modern Optics **44**, 1999–2010 (1997).

[95]K. Konthasinghe, J. Walker, M. Peiris, C. K. Shih, Y. Yu, M. F. Li, J. F. He, L. J. Wang, H. Q. Ni, Z. C. Niu, and A. Muller, "Coherent versus incoherent light scattering from a quantum dot", Phys. Rev. B **85**, 235315 (2012).

[96]H. S. Nguyen, G. Sallen, C. Voisin, P. Roussignol, C. Diederichs, and G. Cassabois, "Ultra-coherent single photon source", Applied Physics Letters **99**, 261904 (2011).

[97]C. Matthiesen, A. N. Vamivakas, and M. Atatüre, "Subnatural linewidth single photons from a quantum dot", Phys. Rev. Lett. **108**, 093602 (2012).

[98]B. R. Mollow, "Power spectrum of light scattered by two-level systems", Phys. Rev. **188**, 1969–1975 (1969).

[99]C. Cohen-Tannoudji and S. Reynaud, "Atoms in strong light-fields: photon antibunching in single atom fluorescence", Philosophical Transactions of the Royal Society of London. Series A, Mathematical and Physical Sciences **293**, 223–237 (1979).

[100]A. Aspect, G. Roger, S. Reynaud, J. Dalibard, and C. Cohen-Tannoudji, "Time correlations between the two sidebands of the resonance fluorescence triplet", Phys. Rev. Lett. **45**, 617–620 (1980).

[101]C. A. Schrama, G. Nienhuis, H. A. Dijkerman, C. Steijsiger, and H. G. M. Heideman, "Intensity correlations between the components of the resonance fluorescence triplet", Phys. Rev. A **45**, 8045–8055 (1992).

[102]G. Nienhuis, "Spectral correlations in resonance fluorescence", Phys. Rev. A **47**, 510–518 (1993).

[103]A. Ulhaq, S. Weiler, S. M. Ulrich, R. Roßbach, M. Jetter, and P. Michler, "Cascaded single-photon emission from the Mollow triplet sidebands of a quantum dot", Nature Photonics **6**, 238–242 (2012).

[104]M. Peiris, B. Petrak, K. Konthasinghe, Y. Yu, Z. C. Niu, and A. Muller, "Two-color photon correlations of the light scattered by a quantum dot", Phys. Rev. B **91**, 195125 (2015).

[105]J. C. López Carreño, E. del Valle, and F. P. Laussy, "Photon correlations from the Mollow triplet", Laser and Photonics Reviews **11**, 1700090 (2017).

[106]L. Hanschke, L. Schweickert, J. C. L. Carreño, E. Schöll, K. D. Zeuner, T. Lettner, E. Z. Casalengua, M. Reindl, S. F. C. da Silva, R. Trotta, J. J. Finley, A. Rastelli, E. del Valle, F. P. Laussy, V. Zwiller, K. Müller, and K. D. Jöns, "Origin of antibunching in resonance fluorescence", Phys. Rev. Lett. **125**, 170402 (2020).

[107]C. L. Phillips, A. J. Brash, D. P. S. McCutcheon, J. Iles-Smith, E. Clarke, B. Royall, M. S. Skolnick, A. M. Fox, and A. Nazir, "Photon statistics of filtered resonance fluorescence", Phys. Rev. Lett. **125**, 043603 (2020).

[108]L. Masters, X. Hu, M. Cordier, G. Maron, L. Pache, A. Rauschenbeutel, M. Schemmer, and J. Volz, "Will a single two-level atom simultaneously scatter two photons?", 2022.

[109]E. Z. Casalengua, E. del Valle, and F. P. Laussy, "Two-photon correlations in detuned resonance fluorescence", Physica Scripta **98**, 055104 (2023).

[110]F. Schuda, C. R. Stroud, and M. Hercher, "Observation of the resonant stark effect at optical frequencies", Journal of Physics B: Atomic and Molecular Physics **7**, L198–L202 (1974).

[111]W. Hartig, W. Rasmussen, R. Schieder, and H. Walther, "Study of the frequency distribution of the fluorescent light induced by monochromatic radiation", Zeitschrift für Physik A Atoms and Nuclei **278**, 205–210 (1976).

[112]R. E. Grove, F. Y. Wu, and S. Ezekiel, "Measurement of the spectrum of resonance fluorescence from a two-level atom in an intense monochromatic field", Phys. Rev. A **15**, 227–233 (1977).

[113]A. Muller, E. B. Flagg, P. Bianucci, X. Y. Wang, D. G. Deppe, W. Ma, J. Zhang, G. J. Salamo, M. Xiao, and C. K. Shih, "Resonance fluorescence from a coherently driven semiconductor quantum dot in a cavity", Phys. Rev. Lett. **99**, 187402 (2007).

[114]A. Nick Vamivakas, Y. Zhao, C.-Y. Lu, and M. Atatüre, "Spin-resolved quantum-dot resonance fluorescence", Nature Physics **5**, 198–202 (2009).

[115]E. B. Flagg, A. Muller, J. W. Robertson, S. Founta, D. G. Deppe, M. Xiao, W. Ma, G. J. Salamo, and C. K. Shih, "Resonantly driven coherent oscillations in a solid-state quantum emitter", Nature Physics **5**, 203–207 (2009).

[116]S. Ates, S. M. Ulrich, S. Reitzenstein, A. Löffler, A. Forchel, and P. Michler, "Post-selected indistinguishable photons from the resonance fluorescence of a single quantum dot in a microcavity", Phys. Rev. Lett. **103**, 167402 (2009).

[117]G. Wrigge, I. Gerhardt, J. Hwang, G. Zumofen, and V. Sandoghdar, "Efficient coupling of photons to a single molecule and the observation of its resonance fluorescence", Nature Physics **4**, 60–66 (2008).

[118]Y. Stalgies, I. Siemers, B. Appasamy, T. Altevogt, and P. E. Toschek, "The spectrum of single-atom resonance fluorescence", Europhysics Letters (EPL) **35**, 259–264 (1996).

[119]J. D. Sterk, L. Luo, T. A. Manning, P. Maunz, and C. Monroe, "Photon collection from a trapped ion-cavity system", Phys. Rev. A **85**, 062308 (2012).

[120]L. Ortiz-Gutiérrez, R. C. Teixeira, A. Eloy, D. F. da Silva, R. Kaiser, R. Bachelard, and M. Fouché, "Mollow triplet in cold atoms", New Journal of Physics **21**, 093019 (2019).

[121]O. Astafiev, A. M. Zagoskin, A. A. Abdumalikov, Y. A. Pashkin, T. Yamamoto, K. Inomata, Y. Nakamura, and J. S. Tsai, "Resonance fluorescence of a single artificial atom", Science **327**, 840–843 (2010).

[122]A. F. van Loo, A. Fedorov, K. Lalumière, B. C. Sanders, A. Blais, and A. Wallraff, "Photon-mediated interactions between distant artificial atoms", Science **342**, 1494–1496 (2013).

[123]D. M. Toyli, A. W. Eddins, S. Boutin, S. Puri, D. Hover, V. Bolkhovsky, W. D. Oliver, A. Blais, and I. Siddiqi, "Resonance fluorescence from an artificial atom in squeezed vacuum", Phys. Rev. X **6**, 031004 (2016).

[124]P. J. Ungar, D. S. Weiss, E. Riis, and S. Chu, "Optical molasses and multilevel atoms: theory", J. Opt. Soc. Am. B **6**, 2058–2071 (1989).

[125]D. S. Weiss, E. Riis, Y. Shevy, P. J. Ungar, and S. Chu, "Optical molasses and multilevel atoms: experiment", J. Opt. Soc. Am. B **6**, 2072–2083 (1989).

[126]D. A. Steck, "Quantum and atom optics", (2007).

[127]R. Loudon, "The quantum theory of light", (OUP Oxford, 2000).

[128]H. J. Kimble, M. Dagenais, and L. Mandel, "Photon antibunching in resonance fluorescence", Phys. Rev. Lett. **39**, 691–695 (1977).

[129]S. Swain, "Master equation derivation of quantum regression theorem", Journal of Physics A: Mathematical and General **14**, 2577 (1981).

[130]H. J. Kimble and L. Mandel, "Theory of resonance fluorescence", Phys. Rev. A **13**, 2123–2144 (1976).

[131]C. Cohen-Tannoudji and S. Reynaud, "Dressed-atom description of resonance fluorescence and absorption spectra of a multi-level atom in an intense laser beam", Journal of Physics B: Atomic and Molecular Physics **10**, 345–363 (1977).

[132]R. H. Brown and R. Q. Twiss, "Correlation between photons in two coherent beams of light", Nature **177**, 27–29 (1956).

[133]A. M. Kaufman, B. J. Lester, and C. A. Regal, "Cooling a single atom in an optical tweezer to its quantum ground state", Phys. Rev. X **2**, 041014 (2012).

[134]R. Grimm, M. Weidemüller, and Y. B. Ovchinnikov, "Optical dipole traps for neutral atoms", in *Advances in atomic, molecular, and optical physics*, Vol. 42 (Elsevier, 2000), pp. 95–170.

[135]M. Saffman, T. G. Walker, and K. Mølmer, "Quantum information with rydberg atoms", Rev. Mod. Phys. **82**, 2313–2363 (2010).

[136]N. Davidson, H. Jin Lee, C. S. Adams, M. Kasevich, and S. Chu, "Long atomic coherence times in an optical dipole trap", Phys. Rev. Lett. **74**, 1311–1314 (1995).

[137]H. J. Lee, C. S. Adams, M. Kasevich, and S. Chu, "Raman cooling of atoms in an optical dipole trap", Phys. Rev. Lett. **76**, 2658–2661 (1996).

[138]T. Kuga, Y. Torii, N. Shiokawa, T. Hirano, Y. Shimizu, and H. Sasada, "Novel optical trap of atoms with a doughnut beam", Phys. Rev. Lett. **78**, 4713–4716 (1997).

[139]R. Ozeri, L. Khaykovich, and N. Davidson, "Long spin relaxation times in a single-beam blue-detuned optical trap", Phys. Rev. A **59**, R1750–R1753 (1999).

[140]L. Isenhower, W. Williams, A. Dally, and M. Saffman, "Atom trapping in an interferometrically generated bottle beam trap", Opt. Lett. **34**, 1159–1161 (2009).

[141]D. Yelin, B. E. Bouma, and G. J. Tearney, "Generating an adjustable three-dimensional dark focus", Opt. Lett. **29**, 661–663 (2004).

[142]F. K. Fatemi, M. Bashkansky, and Z. Dutton, "Dynamic high-speed spatial manipulation of cold atoms using acousto-optic and spatial light modulation", Opt. Express **15**, 3589–3596 (2007).

[143]G. Li, S. Zhang, L. Isenhower, K. Maller, and M. Saffman, "Crossed vortex bottle beam trap for single-atom qubits", Opt. Lett. **37**, 851–853 (2012).

[144]D. Sheng, J. Zhang, and L. A. Orozco, "Rb atoms in a blue-detuned dipole trap: coherence and ground-state differential ac stark shift", Phys. Rev. A **87**, 063412 (2013).

[145]P. Xu, X. He, J. Wang, and M. Zhan, "Trapping a single atom in a blue detuned optical bottle beam trap", Opt. Lett. **35**, 2164–2166 (2010).

[146]D. Barredo, V. Lienhard, P. Scholl, S. de Léséleuc, T. Boulier, A. Browaeys, and T. Lahaye, "Three-dimensional trapping of individual rydberg atoms in ponderomotive bottle beam traps", Phys. Rev. Lett. **124**, 023201 (2020).

[147]M. K. Tey, G. Maslennikov, T. C H Liew, S. A. Aljunid, F. Huber, B. Chng, Z. Chen, V. Scarani, and C. Kurtsiefer, "Interfacing light and single atoms with a lens", New Journal of Physics **11**, 043011 (2009).

[148]J. D. Jackson, "Classical electrodynamics", 1999.

[149]V. V. Ivanov, J. A. Isaacs, M. Saffman, S. A. Kemme, A. R. Ellis, G. R. Brady, J. R. Wendt, G. W. Biedermann, and S. Samora, "Atom trapping in a bottle beam created by a diffractive optical element", 2013.

[150]C. Tuchendler, A. M. Lance, A. Browaeys, Y. R. P. Sortais, and P. Grangier, "Energy distribution and cooling of a single atom in an optical tweezer", Phys. Rev. A **78**, 033425 (2008).

[151]M. Peiris, K. Konthasinghe, and A. Muller, "Franson interference generated by a two-level system", Phys. Rev. Lett. **118**, 030501 (2017).